論文 / 著書情報
Article / Book Information

題目(和文)	
Title(English)	Development of a Single-Camera Markerless Optical Motion Capture System for Biomechanical Analysis
著者(和文)	Ferryanto
Author(English)	Ferryanto Ferryanto
出典(和文)	学位:博士(工学), 学位授与機関:東京工業大学, 報告番号:乙第4192号, 授与年月日:2023年3月31日, 学位の種別:論文博士, 審査員:中島 求,倉林 大輔,塚越 秀行,田中 正行,宮崎 祐介
Citation(English)	Degree:Doctor (Engineering), Conferring organization: Tokyo Institute of Technology, Report number:乙第4192号, Conferred date:2023/3/31, Degree Type:Thesis doctor, Examiner:,,,,
学位種別(和文)	博士論文
Type(English)	Doctoral Thesis

Doctoral Thesis

Development of a Single-Camera Markerless Optical Motion Capture System for Biomechanical Analysis

FERRYANTO

A thesis submitted in partial fulfilment of requirements
For the degree of Doctor of Engineering

December 2022

Department of System and Control Engineering
Tokyo Institute of Technology

Supervisor Professor MOTOMU NAKASHIMA

This page is intentionally left blank

Contents

List of Figures

List of Tables

Chapter 1
Introduction

1.1 Background

Movement analysis is an assessment of an individual's motion. It may combine the biomechanics assessment by a trained individual or the use of technology such as video analysis [1]. Movement analysis may be applied in medical and sports application. There are two main applications of movement analysis in sports, such as performance improvement and injury prevention of athletes. For example, Cohen et al. use the combination of kinematic data and Smoothed-particle hydrodynamics (SPH)-based flow modeling to explore the degree to which the instantaneous thrust generated by the arms is controlled by the hand trajectories, their orientation, and speeds during the freestyle stroke. In addition, they also examine the effect of hand-generated vortices that travel along the body toward the kicking legs, which may be used to enhance propulsion. As a result, they found that the hand motions generate vortical structures that travel along the body toward the kicking legs, and the hands are shown to produce thrust using both lift and drag. These findings advance understanding of the freestyle stroke and may be used to improve athlete technique [2]. One example of sports biomechanics application in injury prevention is the study of Kibler in 1998 [3]. Kibler concludes that shoulder injury in sports could be prevented by core stabilization and scapular stabilization since the scapula is the kinetic chain from the legs and trunk to the shoulders [3], [4]. Hence, coaches and physical therapists should strengthen the entire kinetic chain to prevent and treat shoulder injuries.

Given the importance of movement analysis in various fields of human life, the movement of the human body needs to be measured to get a position that can then be continued for kinematics analysis. Kinematics parameters, ground reaction forces, and anthropometry are needed for kinetic analysis to obtain force and torque loads on the joints of the human body, as shown in Figure 1.1. The ground reaction force can be measured using a force plate. A force plate is an instrumented plate installed flush with the ground for the registration of GRF and Center of Pressure (CoP). The sensor used in the force plate could be piezoelectric material [5] or load cell [6]. The force and torque on the joints of the human body can then be analyzed

further to obtain the tension on the muscles. On the other hand, the muscle tension can also be measured using electromyography (EMG) [7], [8].

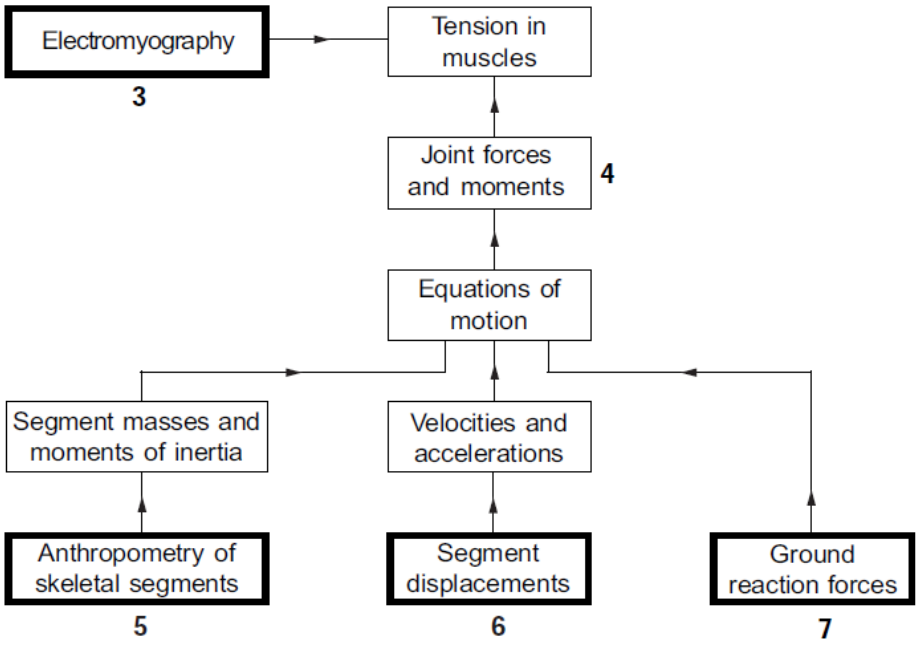

Figure 1.1 Human movement analysis [9]

Currently, the measurement of the joint position of the human body can use an inertia measurement unit (IMU) and an optical motion capture system. Inertial Measurement Unit (IMU) is an electronic device composed of accelerometer and gyroscope sensors. The accelerometer is used to measure linear acceleration, while the gyroscope is used to measure angular (angular) velocity. In the last decade, micro-electromechanical-based IMUs (MEMS) have become the main alternative as a substitute for Optical Motion Capture. Wireless inertial measurement technology is required in such applications. Various IMU manufacturers are competing to create a multisensory IMU platform where the system is already integrated with a centralized transmitter module and is available with data processing algorithms and filters. Figure 1.2 shows the example if IMU with 6 degrees of freedom.

The optical motion capture system is a measurement of the joint movement of the human body using a camera and several markers attached to the human body. Measurement of motion using a camera has actually been started since 1878 by Muybridge [10]. At that time, Muybridge used a camera to record and observe the horse's movements. Since then, cameras have often been used to record the movements of living things in the film world, along with the development of camera technology.

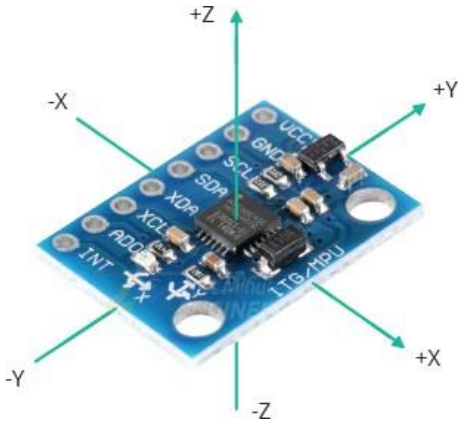

Figure 1.2 IMU with 6 degrees of freedom (MPU6050) [11]

In the optical-based measurement of joint position, the number of cameras used is a minimum of one camera for two-dimensional measurements and a minimum of two cameras for three-dimensional measurements. The advantages of optical/image measurement techniques are as follows [12]: (a) All data from the measurement results of this technique are absolute, (b) The number of markers that can be used is unlimited, (c) Disturbances in gait normality can be reduced, and the attachment of markers does not take long, (d) Video cameras are generally not very expensive, and (e) The results of the video recording can be used again for further analysis. In biomechanics, the marker-based technique of optical motion capture is the most common technique and is used as the gold standard in motion analysis because of its high accuracy. An optical motion capture system is often used together with force plates to obtain all parameters required in the dynamics analysis of movement. Figure 1.3 shows the typical setup of the experiment in the movement analysis. One of commercial optical motion capture for swimming analysis that use marker-based technique is Qualysis [13], Vicon [14], or Optitrack [15].

In general, the movement measurement procedures using marker-based optical motion capture system techniques are divided into four steps: camera calibration, marker installation, marker detection and tracking, and 2D/3D reconstruction. Camera calibration is a process to obtain the intrinsic and extrinsic parameters of the camera so that the relationship between the image and the world coordinate system can be known. Figure 1.4 depicts the pin-hole camera model often used to obtain the relationship between the image and the world coordinate system. Currently, there are many camera calibration methods, namely Direct Linear Transformation [16], which was then further developed into Modified Direct Linear Transformation (MDLT)

[17], Tsai [18], Faugeras [19], or Zhang camera model [20]. The calibrated camera is then used to record the movement of the marker mounted on the human body.

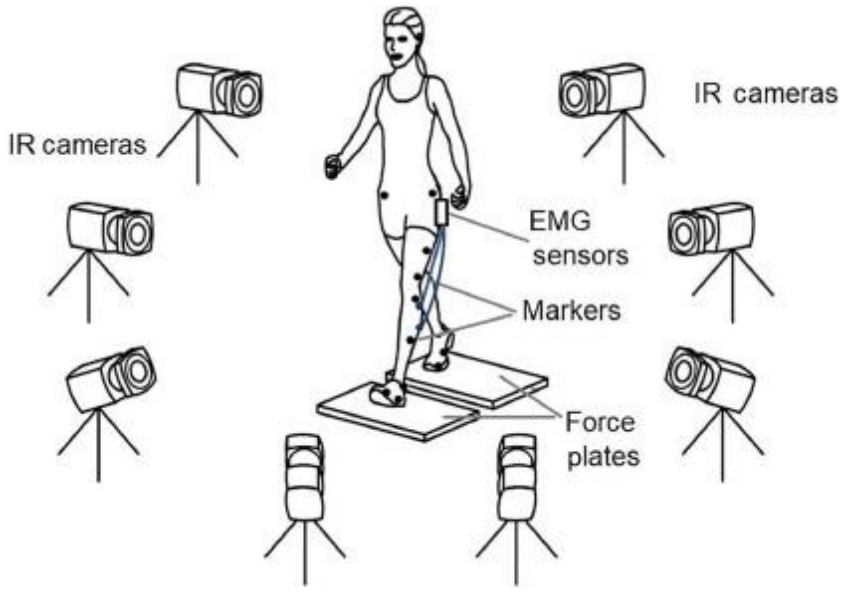

Figure 1.3 Typical experimental setup for movement analysis [21]

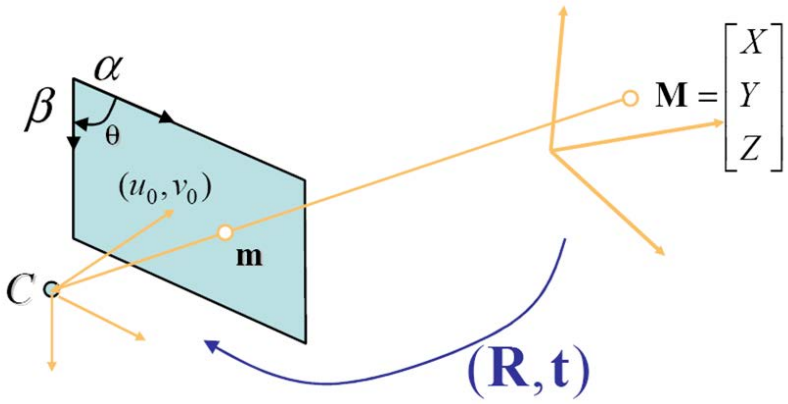

Figure 1.4 Pin-hole camera model [22]

The marker used in the marker-based optical motion capture system can be an active marker or a passive marker. Active markers require a power supply so they can emit light. Meanwhile, passive markers reflect the surrounding light, so they do not need a power supply. The attachment of markers on the body usually follows the Helen Hayes configuration [23] or the Cleveland Clinic marker set [24]. Figure 1.5 shows the Helen-Hayes marker configuration.

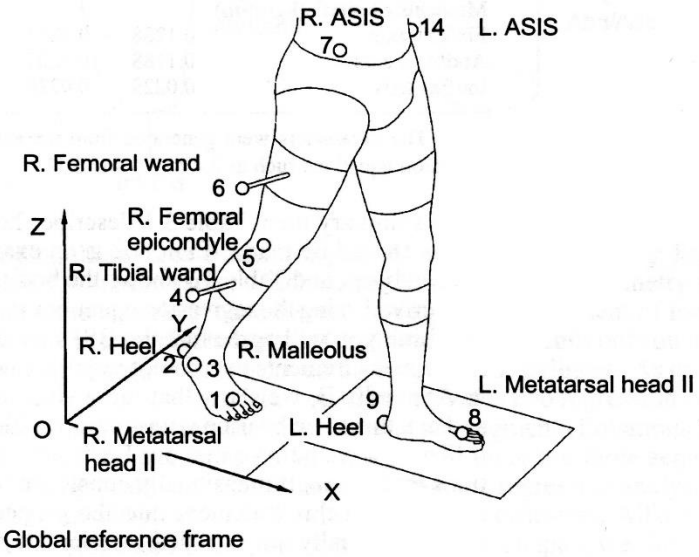

Figure 1.5 Halen Hayes marker configuration [9]

The recorded markers will then be detected and tracked for every human body movement video frame. Marker tracking usually uses the least square method [25]. The result of tracking markers is the position of the marker in the image coordinate system for each frame. The last process of measuring movement using a marker-based optical mocap is 2D/3D reconstruction, where the position of the marker in the image coordinate system is transformed into a world coordinate system by utilizing camera parameters from the camera calibration module.

Despite their accuracy and popularity, a marker-based technique has some limitations [26], i.e., (a) Markers attached to the subject can affect the subject's movements, (b) The time required for marker placement could be excessive, (c) The experimental environment has to be controlled, and (d) The markers on the skin can move relative to the underlying bone. To overcome the limitation of the marker-based technique, markerless optical motion capture system has been developed. In a markerless optical motion capture system, subjects do not have to use markers so that the process of experiment could be simpler and easier. Therefore, markerless motion capture has been a highly active research area in the last decade.

Based on the pose estimation method, the markerless optical motion capture system is divided into two methods, namely, based on deep learning and registration. A deep learning-based markerless optical motion capture system uses a machine learning method to estimate human poses so that parameters of human movement could be obtained. This deep learning method is becoming increasingly developed at this time, following the development of

computers. There are several methods developed in deep learning-based pose estimation, namely OpenPose [27], High-Resolution Net (HRNet) [28], DeepCut [29], and Regional Multi-Person Pose Estimation (AlphaPose) [30].

OpenPose is a real-time multi-person human pose detection library that has, for the first time, shown the capability to jointly detect the human body, foot, hand, and facial keypoints on single images. OpenPose is capable of detecting a total of 135 keypoints. In detecting the keypoints, OpenPose employs a bottom-up methodology in which each body segment of every human visible in the image will be predicted before the actual human is identified [27]. This method results in a nonlinear relationship between the inference time and the number of persons visible in the frame. Additionally, PAFs (Part Affinity Fields) are used by OpenPose to represent segments and the Confidence Map to show where key points on the human anatomy are in the image, as shown in Figure 1.6.

Figure 1.6 Key points on the human anatomy resulted by OpenPose [31]

For estimating multiple human poses, another well-liked bottom-up method is DeepCut. DeepCut is a state-of-the-art approach to multi-person pose estimation based on integer linear programming (ILP) that jointly estimates the poses of all people present in an image by minimizing a joint objective [32]. The model calculates the joint locations for each image after counting the number of people in each image. Videos or images with multiple people or objects, such as those of football, basketball, and other sports, can be edited using DeepCut.

OpenPose has been widely used in sports applications. One of them is the study of Nakai et al. in 2019 on Basketball Free Throw Shooting [33]. They aimed to build a posture analysis model using OpenPose skeletal recognition data and verify the practicality of OpenPose by verifying the model's accuracy. As a result, sufficiently significant prediction

accuracy was obtained. Therefore, posture analysis using OpenPose has been verified to be practical with our model. Another application of OpenPose in sports is estimating a baseball hitter's limb coordinates to investigate whether a baseball hitter performs a good swing. This study was conducted by Li et al. in 2021 [34].

Although the deep-learning pose estimation method in the markerless optical motion capture system was robust, especially the bottom-up approach, this method has major disadvantages. One of the disadvantages that can limit the method's performance is the availability of rare poses [35]. Besides, this method also requires data for the learning session. Hence, this method needs a high computational cost, which is unsuitable for daily sports coaching training.

Another method in the markerless optical motion capture system is registration based. The registration-based markerless optical motion capture system is one solution to overcome the shortcomings of marker-based optical motion capture systems [36]–[38]. Furthermore, since this method is simple and does not need a learning process, the registration-based markerless motion capture system is suitable for daily training in sports.

In 2006, Corazza et al. developed a registration-based markerless optical motion capture system method to analyze human walking motion. At that time, they used a human body model obtained from visual hull reconstruction to assist the tracking process. As a result, Corazza et al. found that the markerless optical motion capture system has great potential in gait analysis. Since then, the markerless optical motion capture system for gait analysis has been applied broadly and could be explored in [26], [39]–[42].

Besides being used for gait analysis, a registration-based markerless optical motion capture system has also been developed for the benefit of sports biomechanics. In 2010, Corazza et al. developed a registration-based markerless optical motion capture system to analyze gymnast movements [43]. The tracking process in the system is carried out using the Levenberg-Marquardt minimization method. In addition to being used for gymnast movement analysis, a registration-based markerless system was also developed to observe the fresh movements of tennis [44], [45]. Ceseracciu first developed a markerless optical motion capture system for underwater applications in 2011 [46]. The overview of the markerless processing procedure conducted in this study is presented in Figure 1.7. Ceseracciu et al. observe hand movements in freestyle swimming. The method developed by Ceseracciu et al. is very promising for the quantitative analysis of swimming movements.

In general, registration based markerless motion capture can be defined as the task of full-body motion capture without the need for marker or specialist suits attached to the body [47]. Because there are no markers or special clothes attached to the human body, obtaining body kinematics parameters when performing movements becomes very challenging. There are many degrees of freedom in estimating body poses which increases the complexity of the system. Therefore, the use of the model is very helpful in reducing the computational load. The model is used as a priori information about the locomotion of a human. Human body models which contain a priori information are used in two ways: actively and passively. Passive models use the information to guide the tracking and pose estimation step to give more convincing results but are not confined to the model. On the other hand, an active model usually has a set of predefined and allowable postures which are represented by individual states of the model, information is drawn from the image and tracking processes and used to select the most convincing predefined pose [47]. In the development of registration-based markerless optical motion capture systems, the models used can be rigid bodies [48], [49], and non-rigid segments [50]. However, these approaches have problems with accurately identifying the three-dimensional kinematics of the segments or using a limited number of body segments [26], [51].

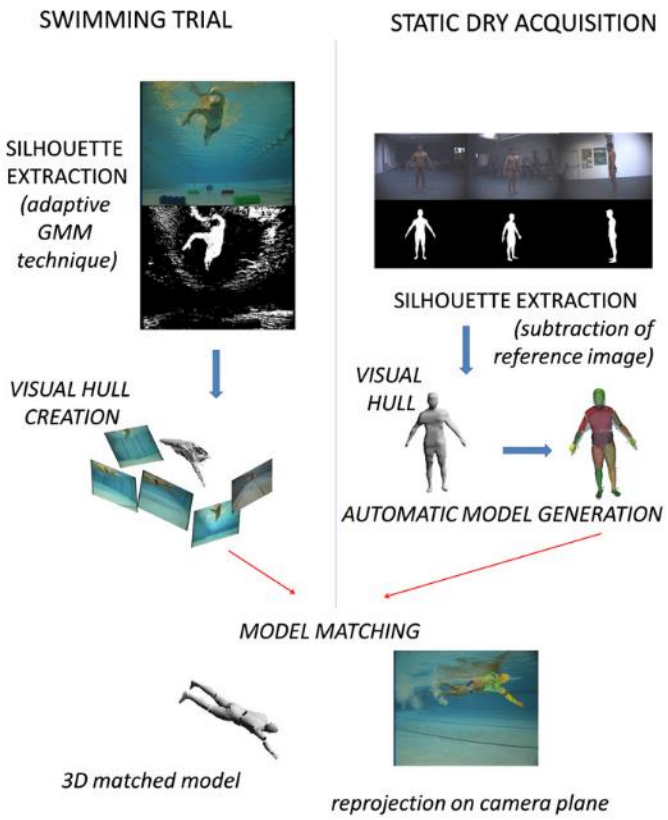

Figure 1.7 The overview of the markerless processing procedure [46]

In addition to model generation, another challenging stage is the tracking process. Tracking is the task of correctly identifying a target from a sequence of frames. The tracking of humans is a difficult task because the appearance of the target changes over time. This process begins with obtaining a body segment from the camera recording, often referred to as image segmentation. Image segmentation algorithms are generally based on one of two basic properties of the pixel intensity value of an image, namely discontinuity, and similarity. Edge-based segmentation is an example of a segmentation method based on the discontinuity of the pixel intensity values. On the other hand, the image segmentation method that uses the principle of similarity of pixel intensity values is region-based segmentation. Along with the development of computer vision technology, there are several algorithms that can be used to obtain a silhouette of the human body, namely background subtraction [52], [53], semantic segmentation [54], [55], and multi-view segmentation [56].

After obtaining the silhouette of the human body, the next challenging stage in the development of markerless optical motion capture is an algorithm to obtain the kinematics parameters of the subject's body. This process is often called image registration, which is an algorithm to move the model so that it overlaps the silhouette [57]. There are many methods in image registration, such as principal component analysis [58] and Iterative Closest Point [59], [60]. The result of image registration is a pose that has been estimated so that the angle of the subject's body segment can be obtained.

1.2 Research Approach

Based on exploring the various methods that can be used in movement analysis described in Section 1.1, the most suitable method for daily training is a registration-based markerless optical motion capture system. This system does not use markers so the data acquisition process could be done quickly. In addition, this system also does not require a learning process as is usually done in the machine learning process. Thus, the computational cost of the registration-based markerless optical motion capture system is low and can be applied to any pose.

One of the simplest setups for data collection is using only one camera. However, one camera can only take the movement in two dimensions. Some sports motions are mainly performed and/or could be evaluated in two dimensional, such as in the sagittal plane or side view. However, some sports movements occur in three dimensional. Therefore, this research's

challenge is to extend the possibility of a single-camera registration-based markerless optical motion capture system.

The present study's approach in responding to the challenge is taking running motion as the targeted movement first. The running motion occurs primarily in two dimensional or sagittal plane. Therefore, running motion is the easiest sport to be analyzed. When the result of analyzing running motion is acceptable, the development of a registration-based markerless optical motion capture system is enhanced to analyze more challenging motion, that is, bilaterally symmetrical swimming stroke. The butterfly stroke is chosen as the investigated stroke in this study. The movement of butterfly stroke occurs in three dimensional, and the movement of the right and left limbs could be considered symmetry. Then, the registration-based markerless optical motion capture system is further developed into an asymmetrical swimming stroke. The front crawl stroke is selected as the targeted stroke. Beside three-dimensional motion, the challenging point in analyzing front crawl stroke is the different movements for the right and left limbs.

1.3 Research objectives

Due to the potential of a registration-based markerless optical motion capture system for daily training, the main objective of this research is to develop a single-camera markerless optical motion capture system for daily training. The system developed must be simple so that data collection preparation can be done quickly and the computational load is not too heavy. In this research, three movements are used as objects to test the accuracy of the developed system. The first movement is the running motion, which occurs mostly in the sagittal plane. Then the next two movements are the butterfly and front crawl stroke of swimming movements. The kinematic results of this system are then combined with kinetic analysis using Swimming Human Simulation Model (SWUM) developed by Nakashima et al. [61]. This application is a powerful analysis tool for various dynamical problems in human swimming to obtain the kinematics and kinetics parameters of swimming motion from relative body motions (joint angles) using the equations of motions for fluid force and body inertia. It is expected that athletes and coaches could use the proposed system for daily training in a shorter time than the use of manual tracking to obtain body motion.

1.4 Advantages of the present Study

As explained in Section 1.3, the main objective of this study is to develop a single-camera markerless optical motion capture system for daily training. One of the advantages of the developed system is it needs only one camera. Since it only uses one camera, the camera placement is easy and simple. There is no required camera arrangement for image acquisition as long as the camera can record a minimum of two movement cycles. Therefore, the experimental setup for daily training could be done in a short period.

Another advantage of the present system is that it does not need any computational learning because it is based on image registration. Therefore, this system can be used for movement analysis, whose datasets are hard to find. Besides, the computational cost of the developed registration-based markerless optical motion capture system could be decreased.

Although the present system uses only one camera, it is applicable for pure two-dimensional and three-dimensional motions. To provide the data in all planes of movements, two methods could be applied. The first method is to acquire the motion data in another two planes separately with additional cameras. Then, the data from all planes could be combined together to obtain three-dimensional data. This three-dimensional data acquisition could be applied in a long period of training, i.e., once a year. However, it is better to conduct a two-dimensional analysis for daily training. The second method in providing three-dimensional analysis for the present system is to combine SWUM databases. This method is applied in this thesis in Chapter 3 and 4.

One of the limitations of the present study is that the body segment is considered a rigid body. Hence, the length of the segment in the model does not change. Therefore, the present study is not suitable for very three-dimensional motions.

1.5 Structure of thesis

The thesis report entitled " Development of a Single-Camera Markerless Optical Motion Capture System for Biomechanical Analysis" is divided into five parts. The five sections will be explained as follows.

The first part is an introductory chapter. This chapter explains the background for selecting the thesis topic, the research approach, and the objective of this research to answer

the requirement proposed in this study, such as should be suitable for daily training. The chapter ends with the structure of the thesis.

The second part is developing a registration-based markerless optical motion capture system for running motion. In this chapter, we will discuss the introduction of the running motion and continue with the research methodology, which contains data collection, model generation, image segmentation, image registration, and identification of right and left limbs. The developed system is also validated with the marker-based optical motion capture system. This chapter ends with a conclusion.

The third part is developing a markerless optical motion capture system for butterfly swimming motion. In this chapter, we will discuss the introduction of the butterfly swimming style and continue with the research methodology, which contains data collection, model making, image segmentation, and image registration. The image registration results are then entered into the SWUM application for kinetic analysis. This chapter ends with a conclusion.

The fourth part is developing a markerless optical motion capture system in the front crawl stroke of swimming. This is conducted because the crawl stroke of swimming motion involves different left and right body movements. Therefore, one of the things discussed in this chapter is the development of algorithms to identify left or right body movements.

The last part is the concluding chapter, which contains the conclusions from the research. In addition, this last chapter also discusses various possibilities for further development of this markerless optical motion capture system.

Chapter 2
Construction of Basic System and Validation for Running Motion

2.1 Introduction

Running is the oldest sport since it started in the first Olympics in 776 BCE. Due to its simplicity and the possibility to perform it anywhere, this sport has become very popular. In the last ten years, running activity has grown around 57% globally [62]. Besides the simplicity, the increase of running activity is also triggered by its benefits, such as health and fitness [63]; and depression and anxiety prevention [64], [65].

The growth of running escalates the attention of researchers in running analysis, either biomechanically or physiologically. The running movement is quantified in biomechanics to obtain running parameters, i.e., spatiotemporal, kinematics, and kinetics parameters. The spatiotemporal parameters in running biomechanics consist of stride length, stride frequency, contact time, flight time, and stride angle [66]. With these parameters, runners' performance could be improved, and the injury could also be prevented. Therefore, the biomechanical analysis of running plays an essential part in sports.

The biomechanical analysis of running could be conducted with the help of several systems, such as optical motion capture [67], [68], force platform [69], [70], or Inertial Measurement Unit (IMU) [71]. In the research conducted by Wouda et al., the running movement was represented by the motion of 41 retroreflective markers attached to the participant's skin [67]. This system is called the marker-based optical motion capture system. There are many commercial marker-based optical motion capture systems, for example, Vicon or Optitrack. However, the price is relatively high. One of the efforts to make the system cheaper is the use of Action Sports Camera (ASC). In 2019, Bernardina et al. compared action sports cameras' accuracy for 3D motion analysis with the commercial motion capture system. It was concluded that the joint angles constructed from the action sports cameras were positively correlated with those obtained from the commercial motion capture system [72].

Even though the application of action sports cameras has cut the cost of a marker-based optical motion capture system, the marker-based system has another disadvantage related to

the biomechanical aspects. Those disadvantages are (a) markers attached to the participant could affect the participant's movements, (b) the time required for marker placement could be excessive, (c) the experimental environment must be controlled, and (d) the markers on the skin could move relative to the underlying bone [26]. One of the proposed methods for dealing with those problems is introducing a markerless optical motion capture system. The markerless optical motion capture system has recently been developed to analyze human gait [73] and swimming motion [46], [74].

Recently, one markerless system, OpenPose has been developed to detect key points at the body, foot, or hand on single images based on a convolutional neural network [27]. OpenPose could perform gait analysis without the attached marker on the participant's anatomical landmarks. There have been studies that evaluate the accuracy of OpenPose in the gait analysis, such as research conducted by Ota et al. [75] and D'Antonio et al. [76]. Ota et al. compared the joint angles of treadmill walking and running using Vicon and OpenPose. They concluded that OpenPose gave good to excellent agreement of joint angle in the sagittal planes with those obtained from Vicon. However, the joint angle in the frontal plane had a significant error [18]. Moreover, in the study of D'Antonio et al., the OpenPose system was inaccurate in the estimation of maxima and minima joint angles compared to IMU [76].

As the result of ASC potential and the drawback of the marker-based optical motion capture system and OpenPose, the present research's aim is to develop a single-camera markerless optical motion capture system for running motion. The present work's main contribution is the system's affordability because it uses an ASC. Besides, the system is simple and time efficient for the use of coaches and athletes since it does not require markers in the data acquisition. Although it is affordable and simple, the proposed system is also accurate in obtaining the joint angle of the participant. It is expected that athletes could use this markerless system in biomechanical analysis to increase their performances and prevent injury.

2.2 Methodology

This section will discuss the methodology used in building the basic construction of a markerless optical motion capture system. This construction will then be used for running movements and other more complicated movements. In general, the basic construction of this system consists of (1) image segmentation, (2) model generation, (3) image matching, and (4) identification of right and left limbs. These four processes will be explained in detail below.

2.2.1 Image Segmentation

The movement images captured by a camera were in the Red, Green, Blue (RGB) format. When an RGB image is fed into a color monitor's red, green, and blue inputs, it creates a color image on the screen. An RGB image can be thought of as three separate images: a red scale image, a green scale image, and a blue scale image stacked on top of one another. Each pixel in each scaled image has an intensity value ranging from zero to $2^p - 1$ where p is the scale image's bit depth. An RGB image in MATLAB is essentially a U x V x 3 array of color pixels, where each color pixel has three values associated with it that represent the red, blue, and green color components of the RGB image at a given spatial location. The U x V denotes the resolution of the image. Figure 2.1 shows the example of RGB image with a resolution 650 x 350 pixels and 8-bit depth on each scale image. As shown in Figure 2.1, the pixel with image coordinate (483, 167) has the intensity value 153, 153, and 255 for red, blue, and green components, respectively.

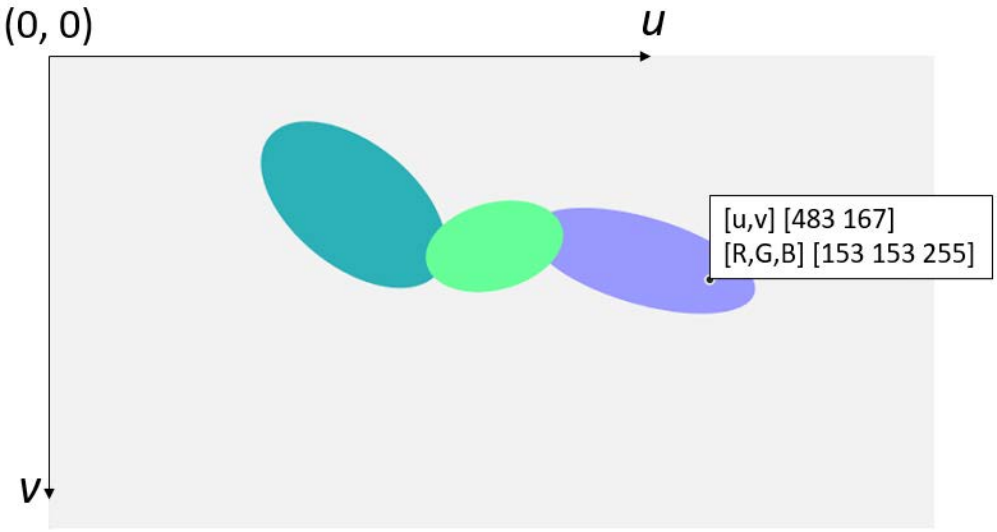

Figure 2.1 Example of intensity value of RGB image

An image segmentation procedure was conducted to extract the silhouette of the body from the background in Figure 2.1. Image segmentation is obtaining the foreground from the background of images. In this case, the foreground was the silhouette of the body. The silhouette was then used in the process of image registration. The result of image segmentation is called a silhouette image, a binary image where each pixel in the image has two intensity values, namely zero for black and one for white, as depicted in Figure 2.2.

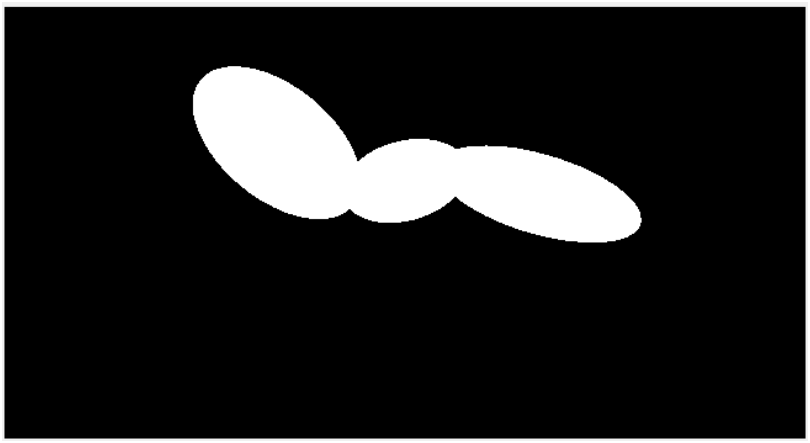

Figure 2.2 The silhouette image as the result of image segmentation

Many techniques of image segmentation have been explored by researchers, such as (1) characteristic feature thresholding or clustering, (2) edge detection, and (3) region extraction [77]. In this research, an adaptive background mixture model was applied to obtain the silhouette from the background. This method models each image pixel as a mixture of Gaussian distribution [53], [78]. The pixel is then classified as either background or foreground based on whether the Gaussian distribution, which represents it most effectively, is considered part of the background model. The advantages of this method were its stability and independent of lighting changes.

Mathematically, the silhouette image with resolution *U* x *V* could be represented as a matrix of real number, $f(u, v)$. Each element in the matrix is called as a pixel and has coordinates (u, v) where *u* is the pixel coordinate in the horizontal direction and *v* is the pixel coordinate in the vertical direction. Each pixel in the silhouettes has an intensity value $f(u, v)$. Since the silhouette images are binary images, then the value of $f(u, v)$ is either 0 (black) or 1 (white). Figure 2.3 shows an example of the intensity value of two pixels in the silhouette image with a resolution 650 x 350. The pixel with the coordinate (489, 167) has white color or intensity value 1 (one). On the other hand, the pixel with coordinates (489, 262) is in black color. Hence, its intensity value is 0 (zero).

2.2.2 Model Generation

This research generated a model to provide a priori information to track the body segment position in the recorded movement. The generated model consisted of body segments that are connected by a corresponding joint. Thus, the preliminary information provided by the

model was the transformable kinematics chain. The body segments were transformed to match the pose of silhouette images.

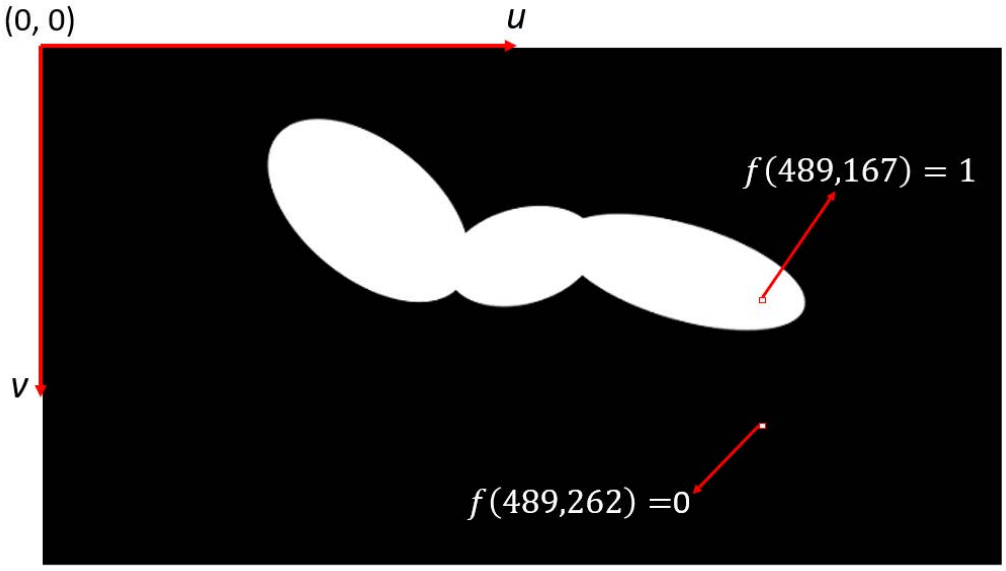

Figure 2.3 The coordinate of pixels and their intensity value for the silhouette image

The body as seen in Figure 2.4 was modeled into three segments and numbered as i = 1 to 3. In the model generation, the body segment was segmented and identified manually to enhance the body segment's accuracy from one of the recorded images. Each segment has centroid g^1, g^2, and g^3 for segment $i = 1$, $i = 2$, and $i = 3$, respectively. Besides the shape of the body segment, the joint's location was also identified in the model. The location of the joint was selected from the centroid of the overlapping area between two segments. For example, the point r^{12} in Figure 2.4 is the joint that connect segment $i = 1$ and $i = 2$. Moreover, the point r^{23} is the joint between segment $i = 2$ and $i = 3$. In Figure 2.4, the location of the segment's centroid and joint between the segment is indicated by • and *, respectively.

All generated body segments are stored in the form of an image model. The model image, $g(u, v)$, is the image of a generated model that will be transformed and registered to the silhouette images. In the model image, there are points belonging to each segment, (u_n^i, v_n^i) for $i = 1, \ldots, 3$ and $n = 1, \ldots, N_i$, where N_i is the total number of points for i^{th} segment, so that $g(u_n^i, v_n^i) = 1$. For example, Figure 2.4 shows the model image with emphasized intensity value of pixels belonging to segment $i = 3$. As seen in Figure 2.4, many points or pixels belong to segment $i = 3$. The intensity value of these pixels is 1 (one). Note that the numbering of points for each segment, $n = 1, \ldots, N_i$, is done by column first, then by row. The image

coordinate of centroid g^1, g^2, and g^3 could be written as (u_g^1, v_g^1), (u_g^2, v_g^2), and (u_g^3, v_g^3), respectively. Moreover, the image coordinate of joint r^{12} and r^{23} is written as (u_r^{12}, v_r^{12}) and (u_r^{23}, v_r^{23}), correspondingly.

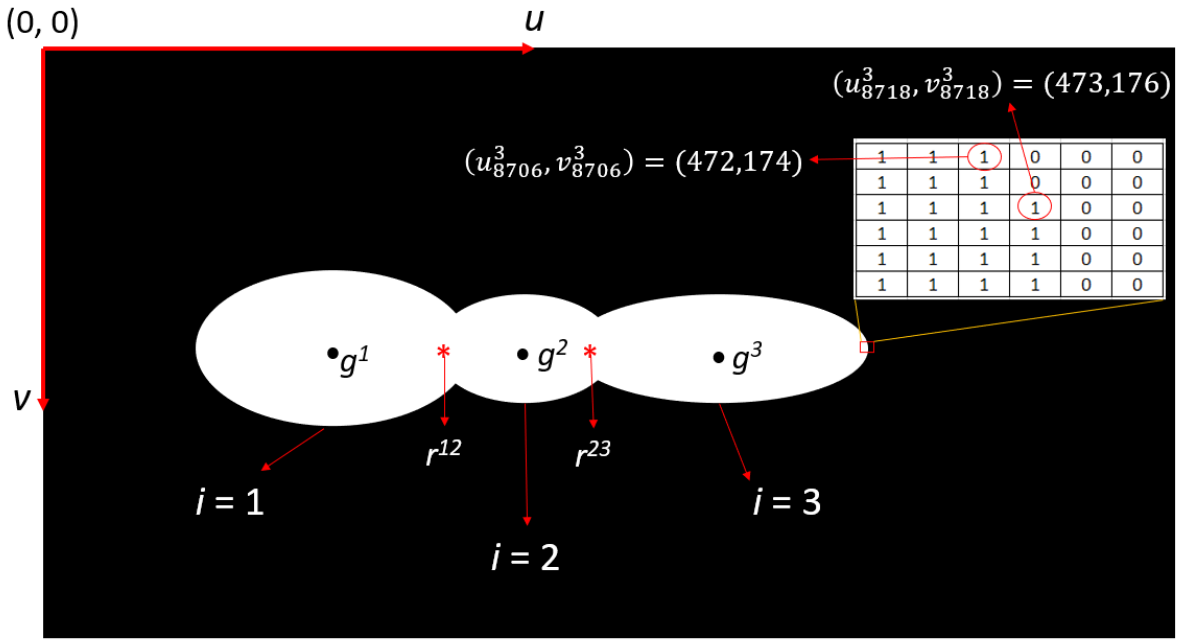

Figure 2.4 The model image

2.2.3 Image Matching

After the model generation, the next step in the present method was image registration. Image registration is a process of matching two images obtained at two different times and conditions, one is taken as the silhouette image, and the other is the model image [57]. The silhouette images are assumed as static, while the model image is an image that is transformed to match the silhouette images. The image registration's target was to obtain the body segment's pose that matched the participant's silhouette. Thus, the rotation angle of each body segment could be acquired.

In general, the image registration process is divided into four steps, i.e., feature detection, feature matching, transform model estimation, and image resampling and transformation [57]. The feature is a unique object and could be easily detected in both reference and sensed images. In the present work, the body segment's shape was utilized as the feature because each body segment has a unique shape and could be easily identified in the

reference and sensed image. The body segment's shape was defined by the points of each segment that has an intensity value is one (white).

After detecting the feature to be used in the image registration, the silhouette and model images' features were matched. The model images' features were transformed by translation and rotation parameters so that the pose of each body segment was similar to those in the silhouette images. The similarity of pixel intensity value between the model and silhouette image was evaluated for each pixel. If the pixel with the same location between the model and silhouette images has the same intensity value, then the pixel similarity increase. Otherwise, if the intensity value of a certain pixel between the silhouette and the model images is different, then there is no increase in pixel similarity.

As explained before, the point for each body segment in the model image, (u_n^i, v_n^i), was transformed in translation and rotation to attain maximum pixel similarity. If every point in each body segment in the model image overlaps perfectly with the silhouette image, then the transformed model image is the same as the silhouette image. Thus, the segment's centroid and joint positions in the transformed model image will be the same as those in the silhouette image. In transforming the body segments in the image model, first, a translation is performed with the parameter (t_u, t_v) so that the centroid of 1st segment in the model (g^1) coincides with the centroid of 1st segment in the silhouette image $(\bar{g}^1)$. The illustration of the translation parameter (t_u, t_v) is shown in Figure 2.5. Note that the red dashed line in Figure 2.5 is the initial position of the segment in the model image.

After the centroid of the first segment in the model (g^1) and the silhouette image coincides $(\bar{g}^1)$, the next transformation is rotation. The first segment is rotated with the parameter θ^1 with respect to the centroid of the first segment (g^1). Next, segments $i = 2$ and $i = 3$ are rotated with respect to their joints, namely r^{12} and $r^{23}$with the parameters θ^2 and θ^3, respectively. Thus, θ^i is the angle of i^{th} segment relative to the initial segment angle in the model. Since the orientation of the segments in the model is horizontal, and their initial angle is zero degrees, then parameter θ^i is defined as the angle of i^{th} segment relative to the horizontal axis, as shown in Figure 2.6. The variable $\bar{r}^{12}$ and $\bar{r}^{23}$ in Figure 2.6 are the position of the joint between segments 1 – 2 and 2 – 3, respectively, after the transformation of the model.

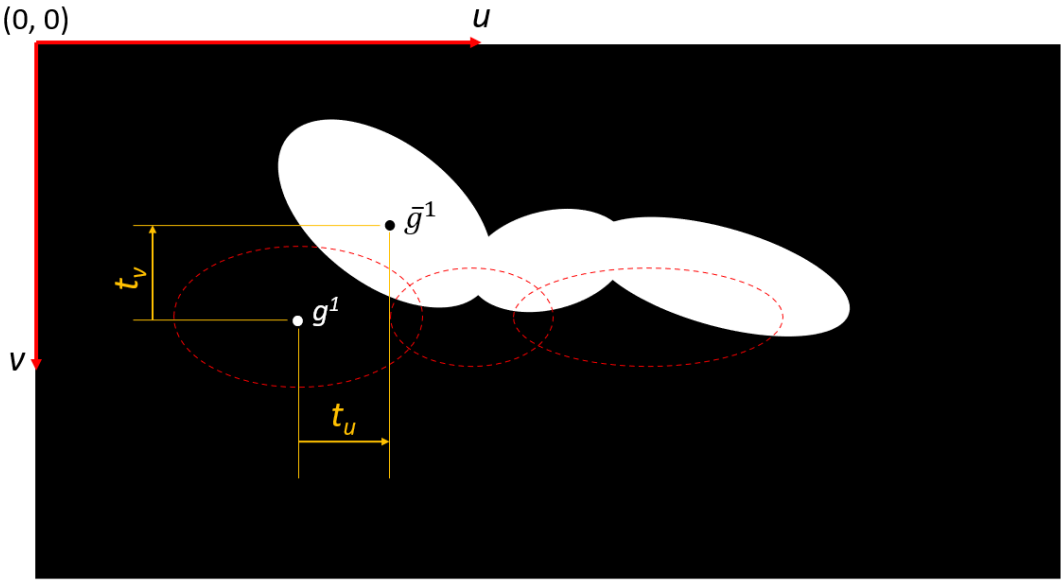

Figure 2.5 Illustration of translation parameter (t_u, t_v) in the transformation of the model

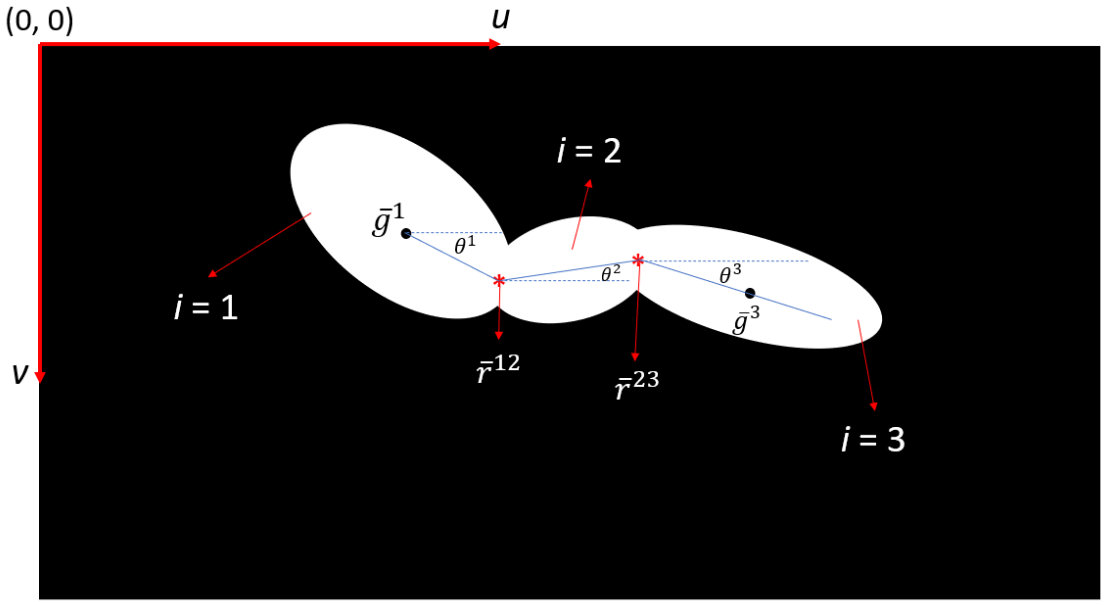

Figure 2.6 The definition of segment angle θ^i for i^{th} segment

Mathematically, every point in each body segment in the transformed model could be determined using Equations 1 – 3 as follows:

$$\bar{u}_n^1 = \left(u_n^1 - u_g^1\right)\cos\theta^1 + \left(v_n^1 - v_g^1\right)\sin\theta^1 + t_u \quad (1a)$$

$$\bar{v}_n^1 = -\left(u_n^1 - u_g^1\right)\sin\theta^1 + \left(v_n^1 - v_g^1\right)\cos\theta^1 + t_v \quad (1b)$$

$$\bar{u}_n^2 = \left(u_n^2 - u_r^{12}\right)\cos\theta^2 + \left(v_n^2 - v_r^{12}\right)\sin\theta^2 + \bar{u}_r^{12} \quad (2a)$$

$$\bar{v}_n^2 = -(u_n^2 - u_r^{12})\sin\theta^2 + (v_n^2 - v_r^{12})\cos\theta^2 + \bar{v}_r^{12} \quad (2b)$$

$$\bar{u}_n^3 = (u_n^3 - u_r^{23})\cos\theta^3 + (v_n^3 - v_r^{23})\sin\theta^3 + \bar{u}_r^{23} \quad (3a)$$

$$\bar{v}_n^3 = -(u_n^3 - u_r^{23})\sin\theta^3 + (v_n^3 - v_r^{23})\cos\theta^3 + \bar{v}_r^{23} \quad (3b)$$

where (u_n^i, v_n^i) is the coordinate of each point for i^{th} segment in the model image that has intensity value one, $(\bar{u}_n^i, \bar{v}_n^i)$ is the coordinate of the transformed point for i^{th} segment, (u_g^1, v_g^1) is the coordinate of the centroid of the first segment, (u_r^{12}, v_r^{12}) is the coordinate of the joint that connects segments 1 – 2 before transformation, (u_r^{23}, v_r^{23}) is the coordinate of the joint that connects segments 2 – 3 before transformation, $(\bar{u}_r^{12}, \bar{v}_r^{12})$ is the coordinate of the joint that connects segments 1 – 2 after transformation, $(\bar{u}_r^{23}, \bar{v}_r^{23})$ is the coordinate of joint that connects segments 2 – 3 after transformation, θ^i is the angle of i^{th} segment, (t_u, t_v) is the translation parameter. Note that i is the segment number where i = 1, 2, or 3. From Equation 1 – 3, it could be seen that the transformation parameters involved in the image matching are $\mathbf{T} = [t_u, t_v, \theta^1, \theta^2, \theta^3]^T$. The coordinate of joint $(\bar{u}_r^{12}, \bar{v}_r^{12})$ and $(\bar{u}_r^{23}, \bar{v}_r^{23})$ could be determined by Equations 4 and 5 below.

$$\bar{u}_r^{12} = \left(u_r^{12} - u_g^1\right)\cos\theta^1 + \left(v_r^{12} - v_g^1\right)\sin\theta^1 + t_u \quad (4a)$$

$$\bar{v}_r^{12} = -\left(u_r^{12} - u_g^1\right)\sin\theta^1 + \left(v_r^{12} - v_g^1\right)\cos\theta^1 + t_v \quad (4b)$$

$$\bar{u}_r^{23} = (u_r^{23} - u_r^{12})\cos\theta^2 + (v_r^{23} - v_r^{12})\sin\theta^2 + \bar{u}_r^{12} \quad (5a)$$

$$\bar{v}_r^{23} = -(u_r^{23} - u_r^{12})\sin\theta^2 + (v_r^{23} - v_r^{12})\cos\theta^2 + \bar{v}_r^{12} \quad (5b)$$

All points in the transformed image model $(\bar{u}_n^i, \bar{v}_n^i)$ are saved as images. The image is called a transformed model image, denoted by $\bar{g}(u, v)$. The intensity value of the transformed model image is stated in Equation 6 below.

$$\bar{g}(u, v) = \begin{cases} 1 & \text{if } (u, v) = (\bar{u}_n^i, \bar{v}_n^i) \\ 0 & \text{otherwise} \end{cases} \quad (6)$$

To ensure the silhouette pose between the model and silhouette image was similar, an optimum transformation parameter $\mathbf{T} = [t_u, t_v, \theta^1, \theta^2, \theta^3]^T$ should be evaluated. The optimum transformation parameters could be estimated by minimizing the objective function (Equation 3). The objective function is the difference in intensity value between transformed points in the model and silhouette image.

$$E = \sum_{u=1}^{U} \sum_{v=1}^{V} |f(u,v) - \bar{g}(u,v)| \tag{7}$$

The transformation parameters were obtained by minimizing the objective function, as shown in the Equation 8.

$$\mathbf{T} = \underset{\mathbf{T}}{\operatorname{argmin}}\, E \tag{8}$$

The expression $\underset{\mathbf{T}}{\operatorname{argmin}}\, E$ is the value of T that makes the dissimilarity E minimum [79]. Equation 8 could be solved by an optimization method.

2.2.4 Identification of Right and Left Limb

The image registration procedure's output was the angle of each body segment for the movement. However, there was no information about the right and left body segment's angle, especially for the upper and lower limb. Therefore, it was necessary to develop an algorithm to identify the right and left lower limb angles based on image registration. Here, running motion is taken as an example of movement.

The developed algorithm to identify the right and left limb's rotation angle employed a least square approach. The least distance approach identified the right or left limb based on the next-frame-rotation angle's distance to the rotation angle in the current frame. For example, the right thigh's rotation angle in the current frame classified the closest rotation angle in the next frame as the right thigh. This approach is based on the fact that the body segment in the running movement should move continuously, and it was unlikely to move too fast that the angle difference between the two frames was so large for the same body segment.

Besides the angle difference between two consecutive frames, other problems need to be considered in identifying on which side the rotation angle is. Those problems were the angular velocity of the right and left limbs in the current frame. The angular velocity affected the classification because of the inertia principle, i.e., if the right limb rotated counter-clockwise in the current frame, then the right limb's candidate should also move in the counter-clockwise direction for the next frame. Hence, this algorithm needed prior information, such as the right and left body segments' initial rotation angle and their direction.

After identifying the rotation angle for the right and left body segment, the present method then obtain the rotation angle for the occluded body segment, particularly the upper arm, forearm, and hand. A curve-fitting procedure estimated their rotation angles.

2.3 Experiment

The main objective of this work is to develop a markerless optical motion capture system for running movement. To assess the performance of the developed program, an experiment was conducted. The experiment was to video the running movement on a treadmill by an ASC. The running movement was recorded only in the sagittal plane. The camera used in this research was the GoPro Hero5 Black series with a resolution of 1080P and a speed of 120 frames per second (fps). The ASC was set on a tripod that was separated 385 cm from the center of the treadmill, as shown in Figure 2.7. The distance between the ASC and the center of the treadmill could be altered on the condition that all the body segments are captured in the camera frame.

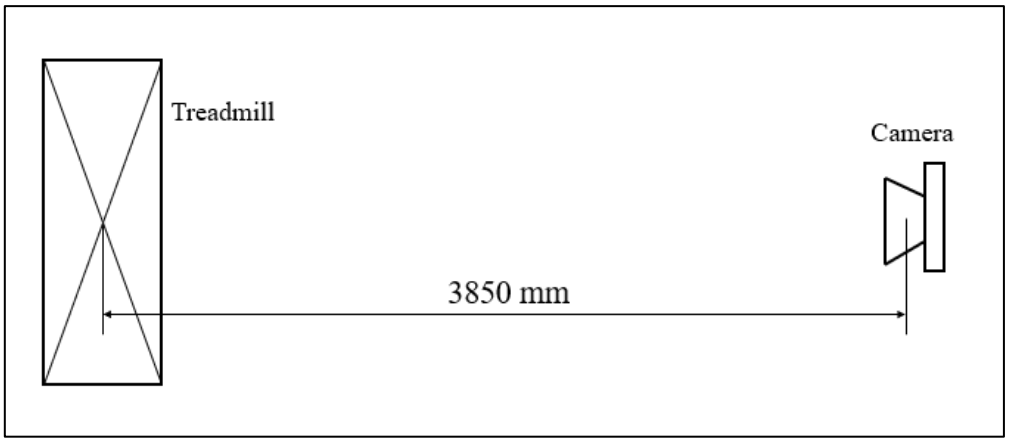

Figure 2.7 The location of camera

Since the present work's objective is to develop a markerless optical motion capture system, the experiment conducted involved only one male participant. The participant had a body weight of 53 kg and a height of 164 cm. Thus, the participant had a Body Mass Index (BMI) of 19.7 which could be categorized as normal. The participant also had normal body posture and did not suffer any abnormality, such as scoliosis, lordosis, or kyphosis. Before data acquisition, the participant was dressed in a white outfit to intensify the participant's image contrast to the background. The higher contrast enhanced the accuracy of image segmentation.

Prior to data acquisition, Zhang camera calibration was conducted to obtain the camera parameters. Those camera parameters were used in 2D reconstruction to obtain the kinematics parameter of running motion. In the data acquisition, the participant ran ten cycles on the treadmill with 3.58 m/s speed or 04:39 minutes per kilometer pace while ASC recorded his movement. Although the speed of 3.58 m/s was used in this experiment, there was no limitation regarding the running speed. Basically, the developed system could be used for any running speed.

2.4 Result and Discussion

The result of the running movement recorded by the GoPro Hero5 Black series camera was a running video which was then extracted into its constituent frames. Figure 2.8 presents the images of running motion recorded by ASC. Note that each frame is labeled with a non-dimensional time normalized to the gait cycle. As could be seen in Figure 2.8, the running movement image is in RGB format.

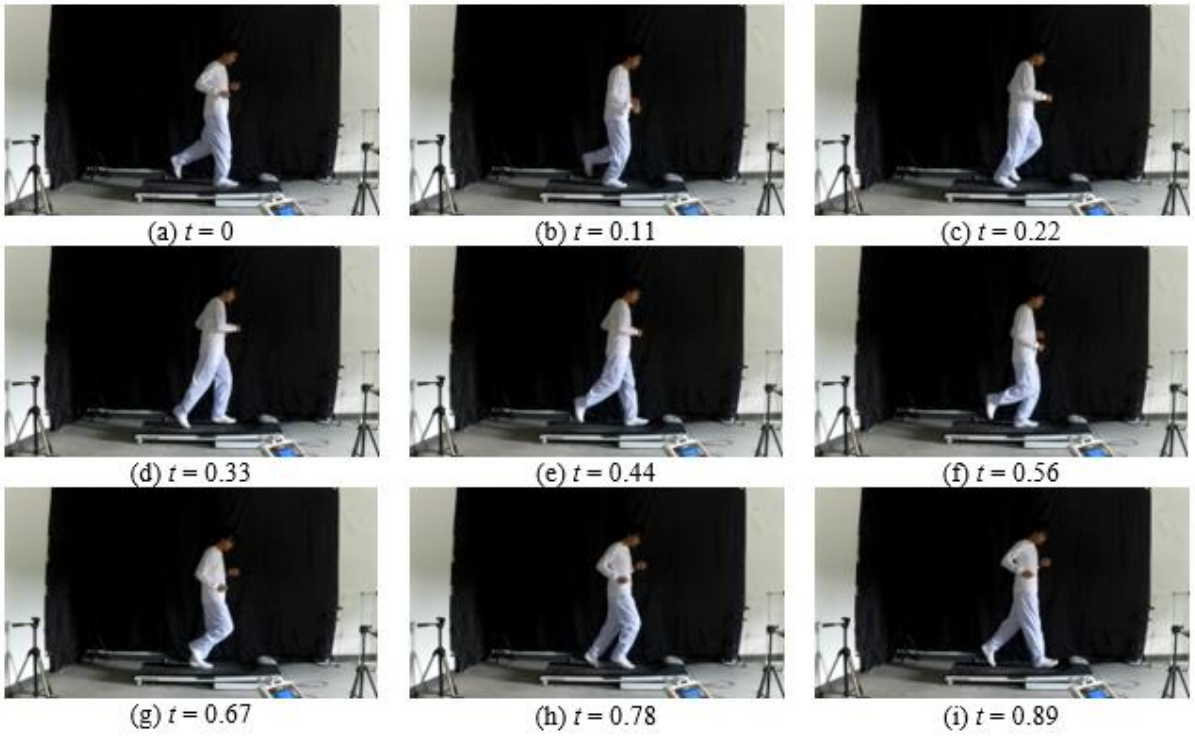

Figure 2.8 The images of running motion recorded by an action sports camera at 120 frames per second. Each frame was labeled by non-dimensional time normalized by the gait cycle

As mentioned in the Methodology, image segmentation is the first step after obtaining the running images. The result of image segmentation is the silhouette images that are binary images. Hence, the intensity value of each pixel in the silhouette images is either zero for black color or one for white color. The method used in the image segmentation is the adaptive background mixture model. Figure 2.9 shows the silhouette images of running motion.

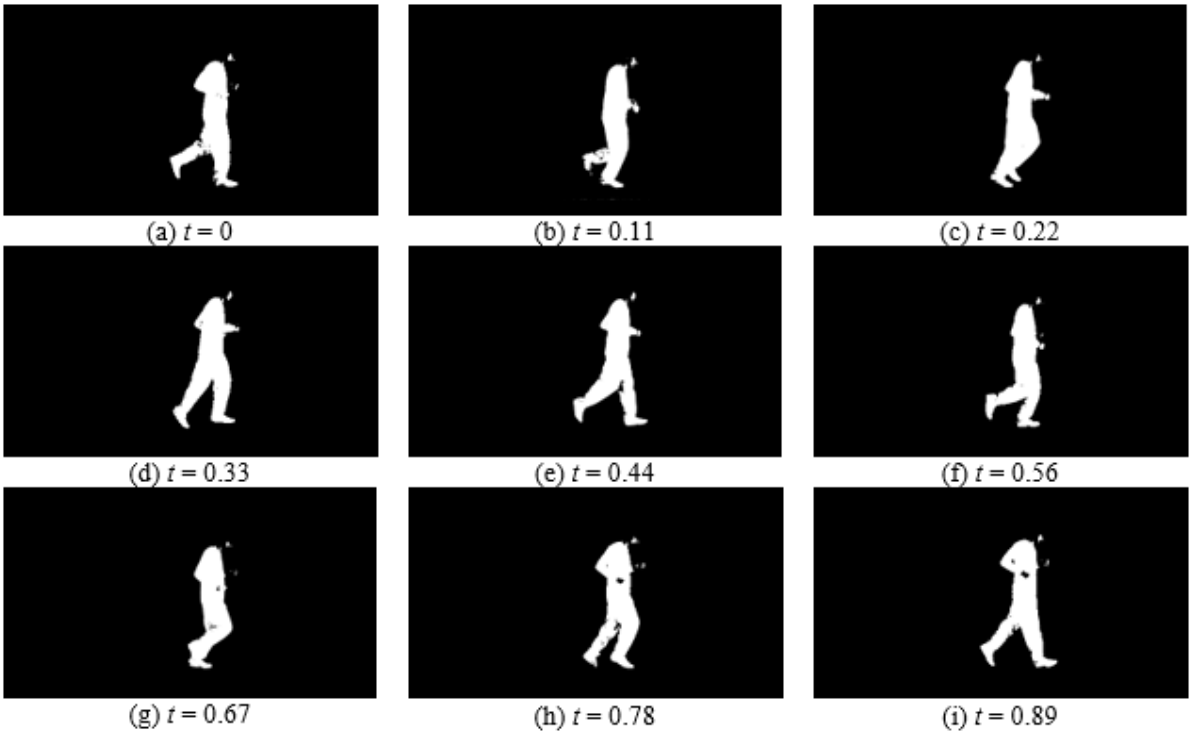

Figure 2.9 The silhouette images as the result of image segmentation of running images. Each frame is in non-dimensional time

Model generation is the next step in building the basic construction of a markerless optical motion capture system. The participant's body was modeled into eight segments for the running motion and numbered as i = 1 to 8. Those body segments were: (1) Head, trunk, and upper limbs as one segment, (2) Hip, (3) Right thigh, (4) Left thigh, (5) Right shank, (6) Left shank, (7) Right foot, (8) Left foot. The head, trunk, and upper limbs were modeled as one segment because the focus of the present research was the biomechanics parameters of the lower body. In the model generation, the body segment was segmented and identified manually to enhance the body segment's accuracy. The model generated for the present work is presented in Figure 2.10. Besides the shape of the body segment, the joint's location was also identified in the model. The location of the joint was selected from the centroid of the overlapping area

between two segments. For instance, the centroid of the overlapping area of the right thigh and right shank was distinguished as the right knee joint. In Figure 2.10, the location of the joint is indicated by *.

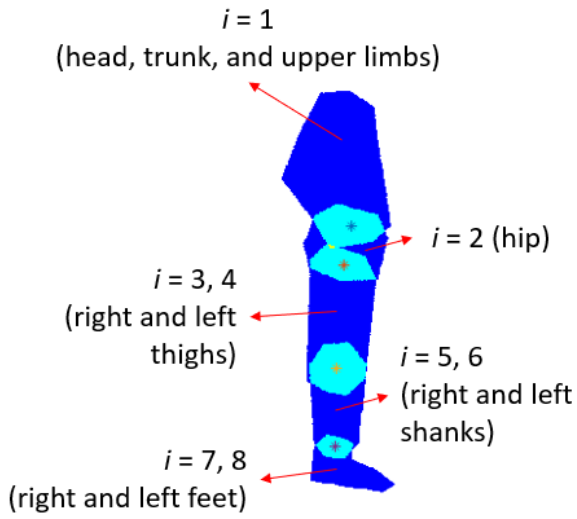

Figure 2.10 The generated model as a priori information for image registration. The * indicates the location of joint

The generated model is then transformed so that its body segments overlap with the silhouette image. Since the human body was modeled as eight segments, then Equations 1 – 5 should be extended they could be applied for the transformation of eight segments. Hence, the transformation parameters in the image matching for this running movement are $\mathbf{T} = [t_u, t_v, \theta^1, \dots, \theta^8]^T$. The objective function in Equation 7 was then minimized so that the transformed model image corresponded perfectly to the silhouette image. In solving Equation 8, the particle swarm optimization method [80] available in MATLAB was used. In the optimization, the transformation parameters were constrained based on the range of motion of each body segment in the running motion. In addition, the constraint of transformation parameters was also helpful to save computational cost. The lower and upper boundaries of the optimization constraints were set to – 90 and 90 degrees, respectively for all body segments. The angle for each segment was then inputted to the algorithm to identify right and left limbs, especially for the lower and upper limbs. Then, a curve-fitting procedure was employed to estimate the angle for the occluded body segment. In this work, the smoothing spline method was exploited with the parameter smoothing of 0.8.

Reference data validated the smoothed rotation angle obtained from the image matching process. The reference data were obtained from manual image matching in this research. The

model was transformed with a pre-developed Graphical user Interface (GUI), as shown in Figure 2.11. The transformation parameters could be inputted to the textbox to translate and rotate the body segment, and the result of the transformation was observed manually. When the transformed model perfectly overlapped with the running image, the transformation parameters were recorded. Those transformation parameters were then called the references.

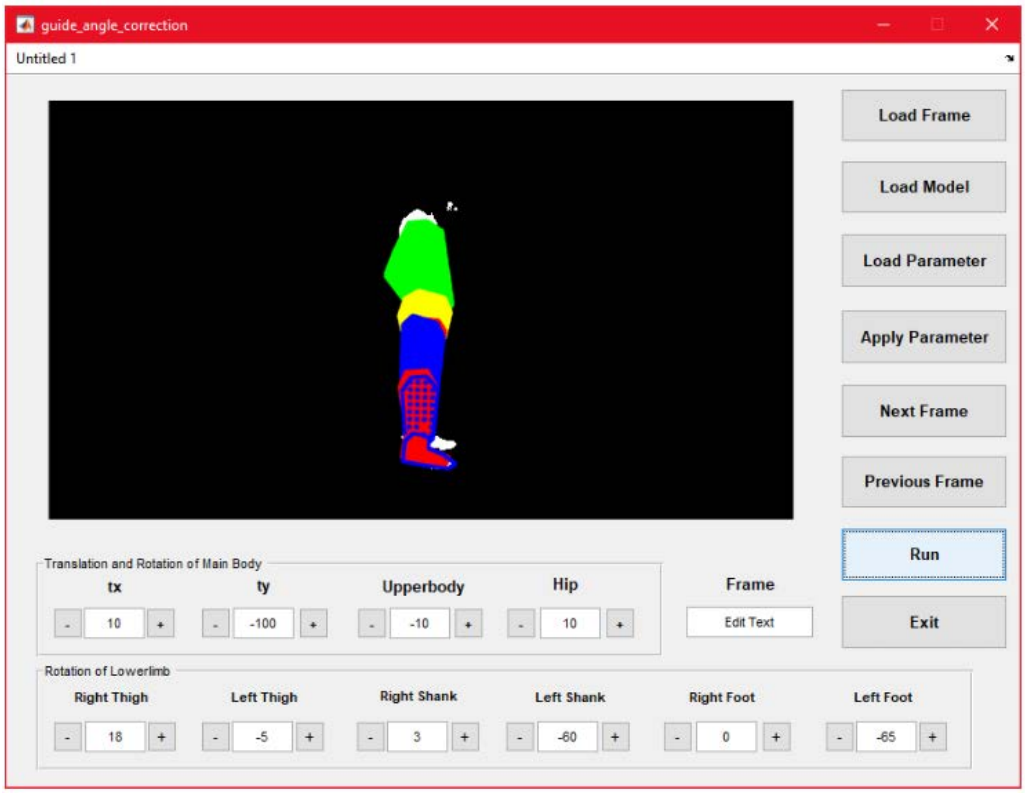

Figure 2.11 The pre-developed Graphical user Interface (GUI) to help the manual matching procedure in obtaining the actual rotation angle

A correlation coefficient between two data was evaluated to confirm the agreement between the rotation angle obtained from image registration and the references. The correlation coefficient ranged from -1 to +1. A good agreement between two data sets was indicated by a correlation coefficient value close to +1. Table 2.1 shows the correlation coefficient between image registration and the references for the present study. As shown in Table 2.1, image registration results were correlated with the references with the lowest correlation coefficient of 0.977. These high correlation coefficients implied that the present work's developed markerless optical motion system for running motion was acceptable. The rotation angle obtained from the developed system is presented in Figure 2.12.

Table 2.1 The Correlation Coefficient of Rotation Angle of Body Segment Obtained from the Developed System Compared to the Reference Data

Body Segment	**Correlation Coefficient**
Head, trunk, and upper limbs	1
Hip	1
Right thigh	0.996
Left thigh	0.995
Right shank	0.989
Left shank	0.992
Right foot	0.991
Left foot	0.977

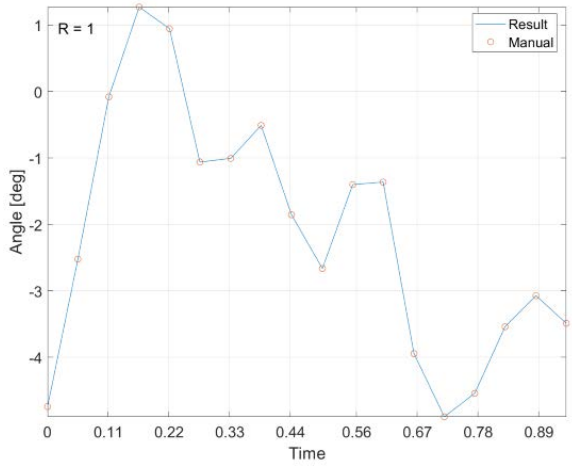

(a)

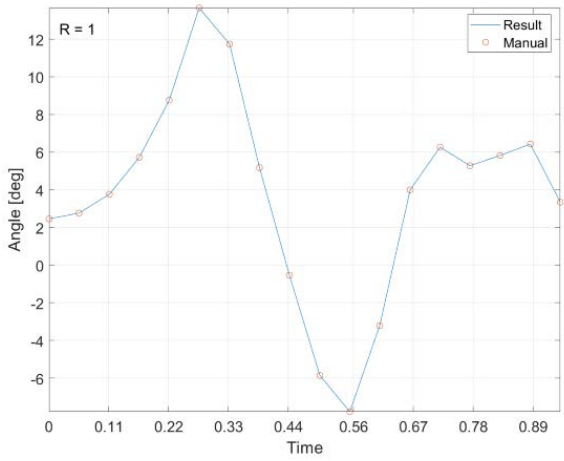

(b)

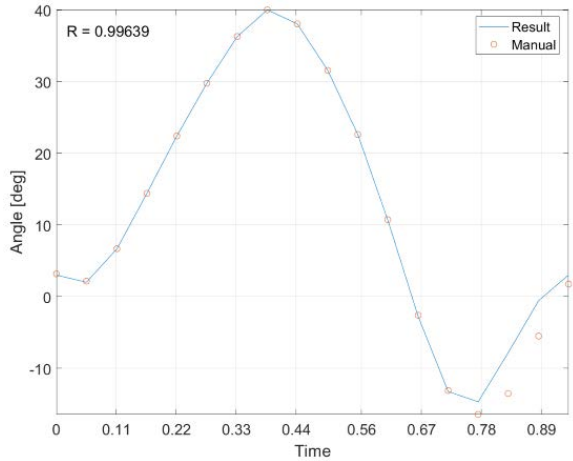

(c)

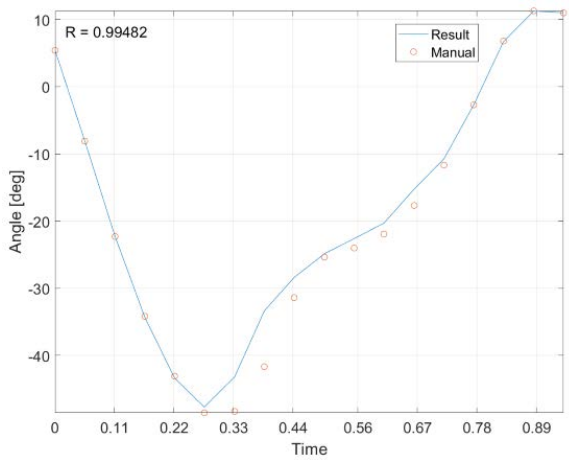

(d)

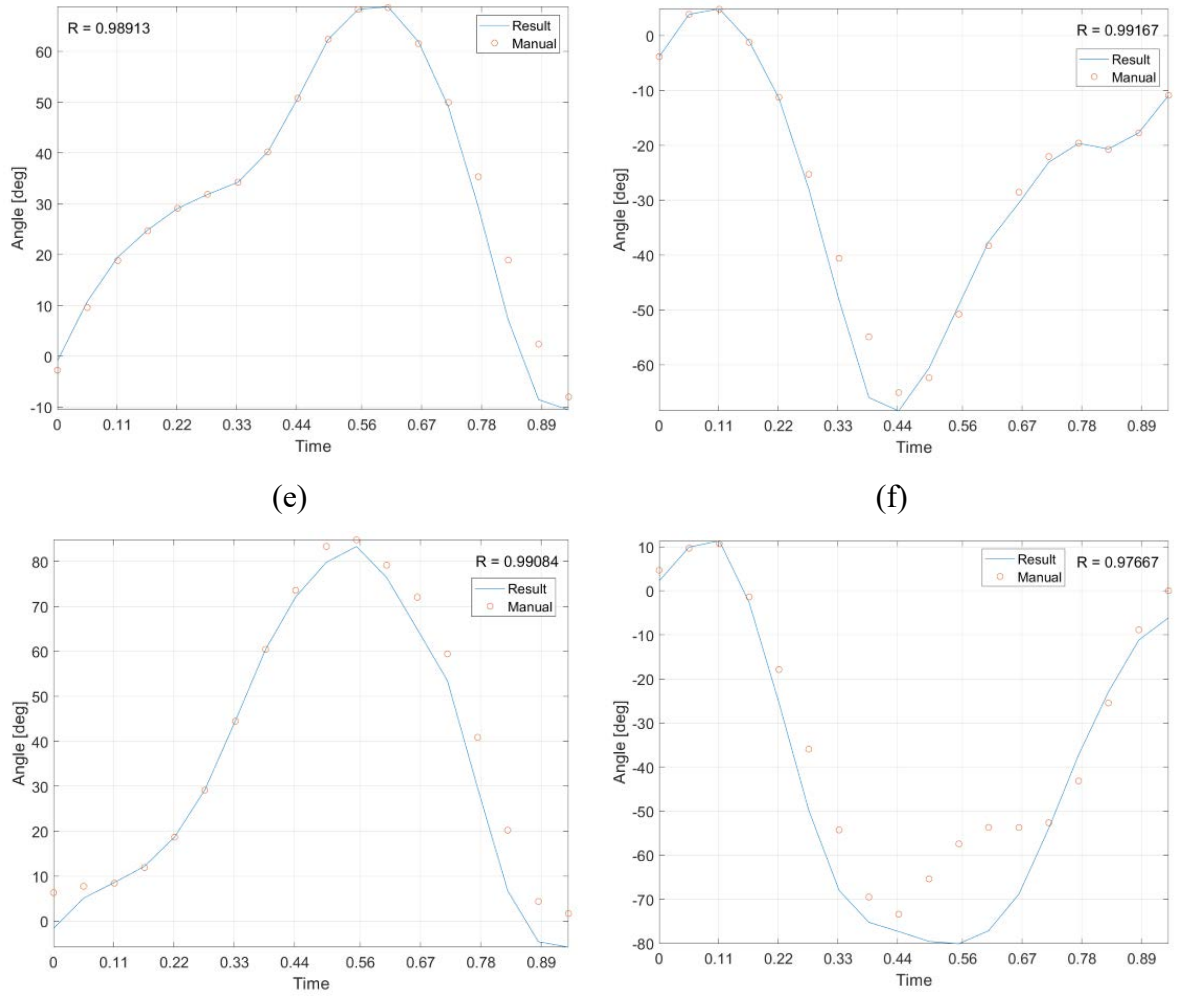

Figure 2.12 The rotation angle obtained from the developed system compared to the rotation angle obtained from the manual matching: (a) head, trunk, and upper limbs as one segment, (b) hip, (c) right thigh, (d) left thigh, (e) right shank, (f) left shank, (g) right foot, and (h) left foot. The time scale in the *x*-axis corresponds to the running frame of Figure 2.8

The rotation angle of each body segment was then used to obtain running parameters, such as spatiotemporal and kinematics parameters. The spatiotemporal parameters of the present running motion are presented in Table 2.2. The parameters were also compared to the result of the Lucas-Cuevas et al. study [66]. It was confirmed that the spatiotemporal parameters of running motion obtained from the developed system were in good agreement with the parameters from Lucas-Cuevas, et al. study. The only different parameter was stride length because the running speed was pre-determined in this study. Hence, the developed

markerless optical motion capture was useful in evaluating the spatiotemporal parameters of running motion.

Table 2.2 The spatiotemporal parameters of present running motion compared to the study of Lucas-Cuevas et al.

Spatio-temporal parameter	Result	Reference [66]
Stride length (m)	3.21	2.25
Stride frequency (Hz)	1.33	1.49
Contact time (s)	0.26	0.24
Flight time (s)	0.11	0.12
Stride angle (degree)	3.14	3.30

Besides the spatiotemporal parameters, kinematics parameters were also investigated to evaluate the advantages of the present system. The joint angle was one of the kinematics parameters investigated in the present study. The joint angle was calculated from the difference of the rotation angle between two body segments. For example, the knee angle is the rotation angle difference of the thigh and shank angle. Here, hip, knee, and ankle angles were calculated for both rights limbs. Figure 2.13 shows the calculated joint angle. The rotation angle could be further analyzed to obtain kinematics parameters. Therefore, the advantages of the developed system were its affordable price since it uses an action sports camera, and ease of use without any need for special configuration in the data acquisition yet yields acceptable running parameters.

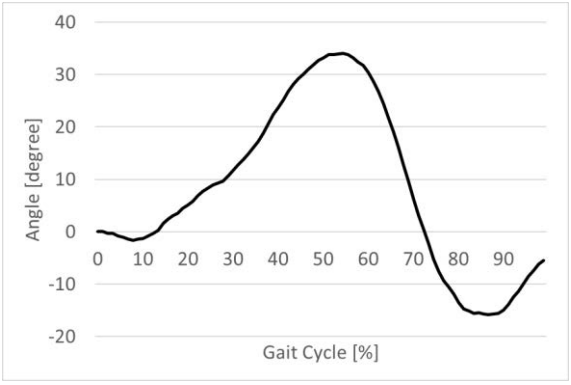

(a)

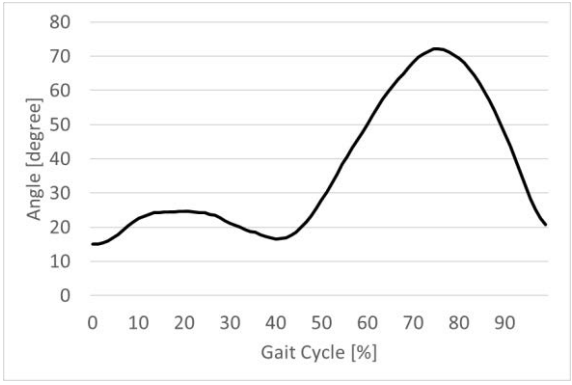

(b)

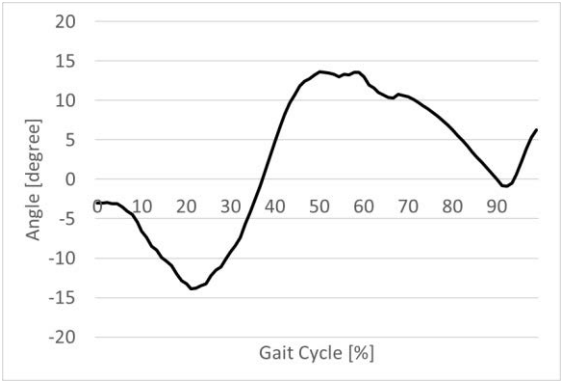

(c)

Figure 2.13 The calculated joint angle: (a) Hip, (b) Knee, and (c) Ankle

2.5 Validation Against Marker-based Optical Motion Capture System

The result of the developed markerless optical motion capture system has been validated with the rotation angle obtained by manual image matching, and it shows good agreement. However, the accuracy of the developed system compared to the marker-based optical motion capture system was still unknown. Therefore, the validation of the system against the marker-based optical motion capture system is described in this section.

In validating the system developed in this study, an additional experiment was carried out to accommodate marker attachment in a marker-based optical motion capture system. Five markers were attached to the hip, knee, ankle, heel, and 5th metatarsal as shown in Figure 2.14. The camera used is the same as described in Section 2.3. The results of data collection are shown in Figure 2.15.

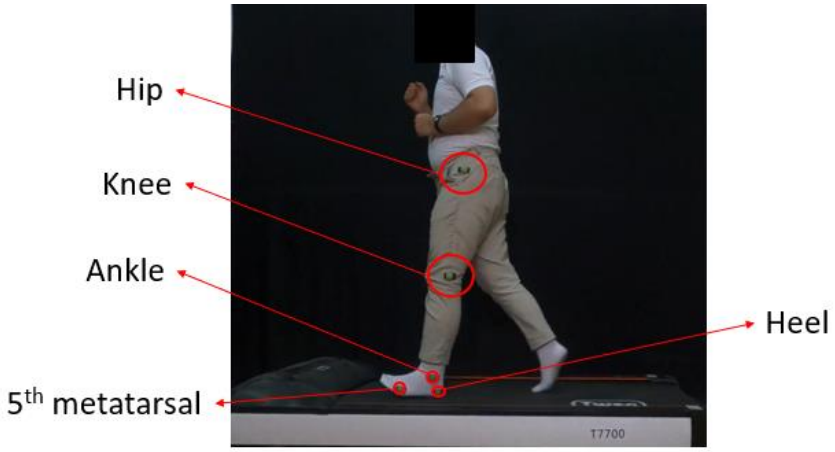

Figure 2.14 Marker placement

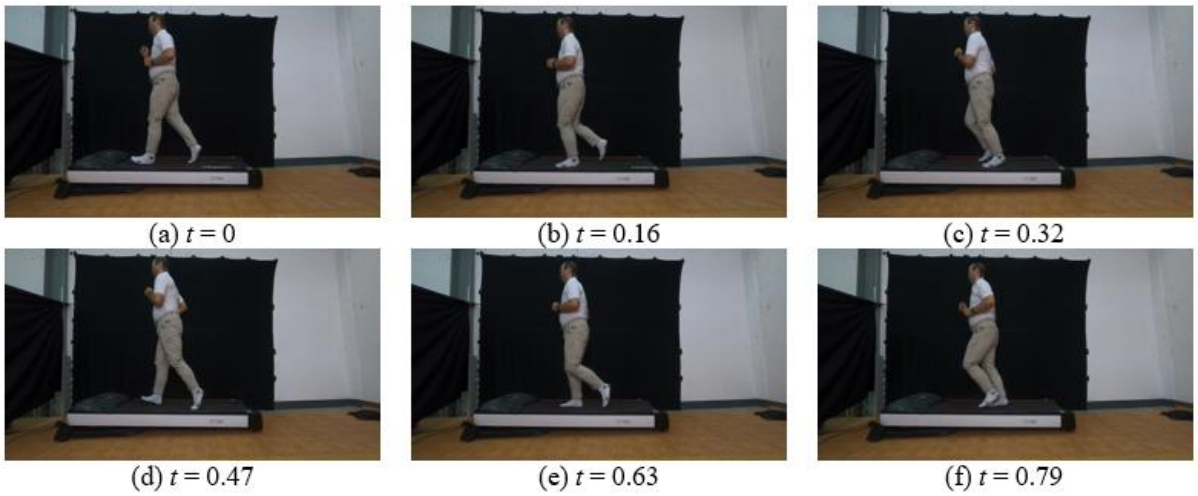

Figure 2.15 The images of running motion recorded by an action sports camera for validation of present system against marker based optical motion capture

After the data acquisition procedure, model generation is the next step in using the markerless optical motion capture system. First, the model is generated by manual image segmentation on one of the frames. The number of body segments in the model is the same as described in Section 2.4. The next step is image segmentation to get the subject's silhouette while running. Figure 2.16 shows the silhouette of image segmentation results. The participant's silhouette is then used for the image matching process and identification of right and left limbs. The methods used in image matching and identification of the right and left bodies are also the same as those described in the Methodology of Section 2.2 with an extension of the number of the segments.

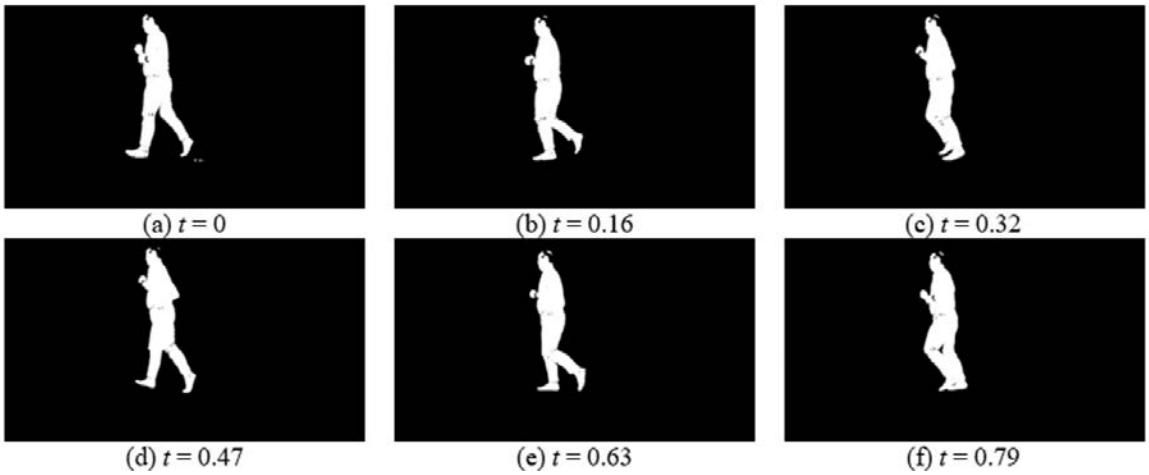

Figure 2.16 Silhouettes of participant as the result of image segmentation

In processing the marker-based optical motion capture system data, the position of each marker for each frame is detected and tracked. The position of the marker is used to calculate the angle of rotation of the lower body segment. Figure 2.17 shows a graph of the rotational angles of the thigh, shank, and foot body segments obtained from a markerless and marker-based optical motion capture system. The segment rotation angle is then used to calculate the joint rotation angle, namely the knee angle and ankle angle. Figure 2.18 shows the knee and ankle angles obtained using the two optical motion capture systems.

To quantitatively compare the results obtained by the markerless and the marker-based optical motion capture systems, their correlation coefficients and root mean square error (RMSE) were calculated. Table 2.3 shows the correlation coefficient and RMSE rotation angles of the segments and joints of the two systems. Table 2.3 shows that the angles of segments and joints obtained from markerless and marker-based optical motion capture systems have good agreement. Therefore, this study's markerless optical motion capture system can be said to have been validated.

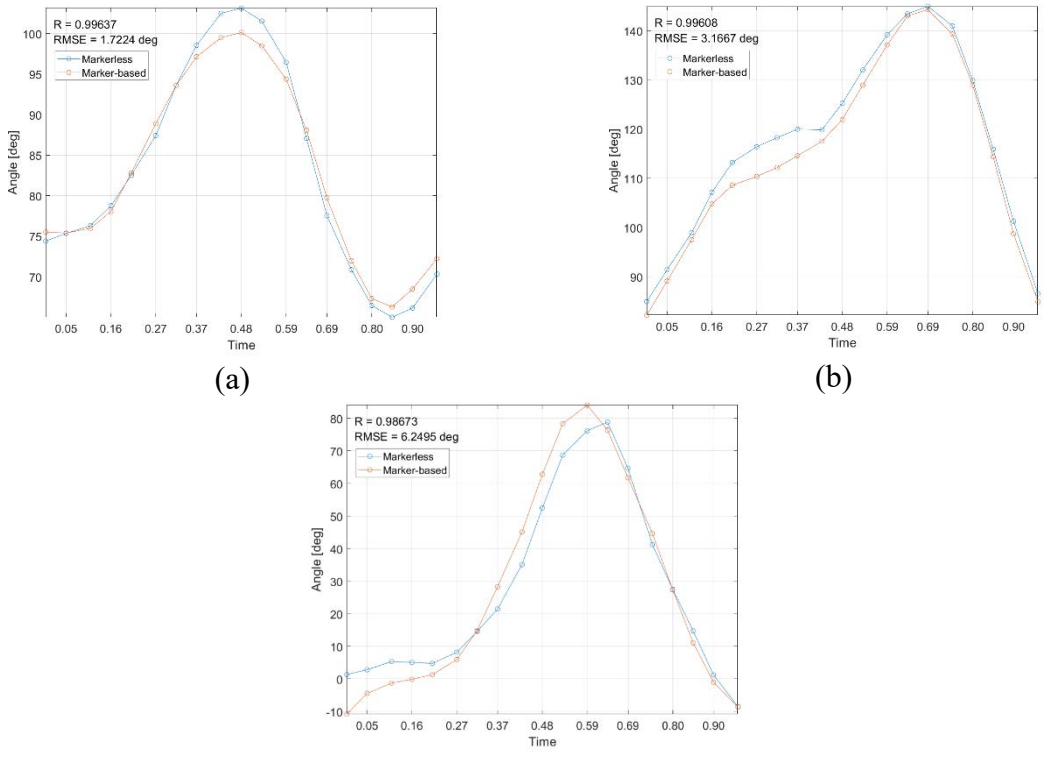

Figure 2.17 Rotation angle of segment (a) thigh, (b) shank, and (c) foot for markerless and marker-based optical motion capture system

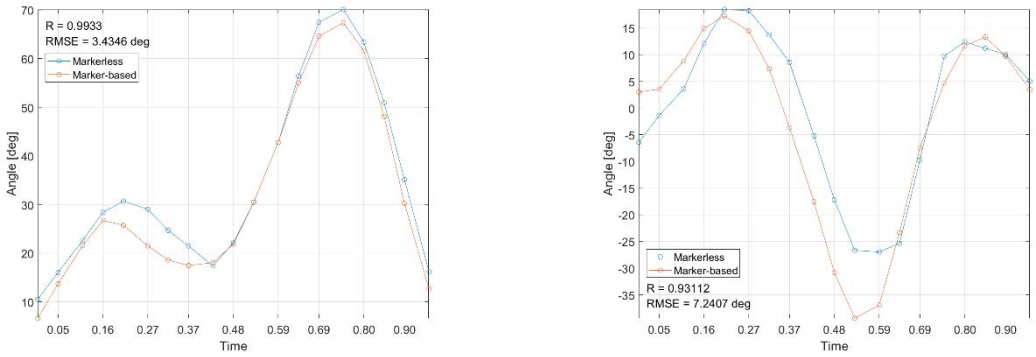

(a) (b)

Figure 2.18 Joint angle of (a) knee and (b) ankle for markerless and marker-based optical motion capture system

Table 2.3 Correlation coefficient and RMSE of rotation angle obtained from markerless and marker-based optical motion capture for running motion

Rotation Angle	Correlation Coefficient	RMSE (degrees)
Segment thigh	0.996	1.72
Segment shank	0.996	3.17
Segment foot	0.987	6.25
Joint knee	0.993	3.43
Joint ankle	0.931	7.24

2.6 Conclusion

The marker-based optical motion capture system has been widely used in the running analysis. The problem of this system is the high-price, and the attached markers could influence the participant's movement. Therefore, the development of a markerless optical motion capture for running movement was proposed in the present work. The system used an action sports camera to capture the movement of the runner. The images of running movement were segmented into binary images to obtain the silhouettes of the participant. Moreover, the human body was modelled as eight segments, i.e., head, trunk, and upper limb as one segment, hip, right thigh, left thigh, right shank, left shank, right foot, and left foot. The model was transformed translationally and rotationally so that its pose is similar to the silhouettes. The pose similarity was indicated by maximum pixel similarity. Particle swarm optimization was

used to maximize the pixel similarity to obtain all the transformation parameters. The obtained transformation parameters were validated by the correlation coefficient to the rotation angle obtained from manual matching. The lowest correlation coefficient was 0.977 for the left foot. It means that the proposed system could be used to obtain the rotation angle of the running analysis. Further analysis was also conducted to obtain the kinematics parameters of running. The developed markerless optical motion capture system has been also validated with the marker-based optical motion capture system. From the segment and joint rotation angle, the lowest correlation coefficient and largest RMSE between both systems are 0.931 and 7.24 degrees. Since the correlation coefficient and RMSE was satisfactory, the development of a markerless optical motion capture system was successful. The system is simple and time-efficient for coaches and athletes since it does not require markers in the data acquisition.

Chapter 3
Extension to Bilaterally Symmetrical Swimming Stroke

3.1 Introduction

Swimming is a motion in which a human self-propels in water. When a human body moves in water, fluid forces act on the body. The fluid forces strongly depend on the motion of the body. Indeed, fluid forces can be propulsive forces as well as drag forces. Therefore, the body motion in the water is very important in swimming. In particular, athletes and coaches of swimming need to measure and acquire the body motion in water since they have to maximize the propulsive force and minimize the drag force to improve performance.

Although the markerless gait analysis has been studied extensively, a markerless optical motion capture system for swimming motion in particular has not been investigated widely. Dubois et al. addressed the problem of detection, segmentation and estimation of body configuration in the biomechanic measures of swimming using a normalized cuts algorithm and the global probability of boundaries [81]. However, the movement of limb segments overtime has not been extracted yet. To the best of the author's knowledge, there was only one research about a markerless analysis of front crawl swimming which used six underwater cameras [46]. While accuracy can be improved by increasing the number of cameras, a large number of cameras could make the system more costly. In addition, the placement of six cameras could be limited due to the swimming pool environment, so the system would be difficult to use in daily training and coaching.

As an alternative to the above system, a more affordable quantitative markerless optical motion capture system for swimming was developed in the present study. The system consisted of only one underwater camera, so the camera placement was not as difficult as the previous research. Consequently, the set up for this system was quite simple and time efficient. Moreover, the system also featured semi-automatic tracking instead of manual tracking to save processing time of the swimming motion analysis. It is expected that the proposed system could be used by athletes and coaches for daily training in a shorter time compared to the time needed to use manual tracking to obtain a swimmer's body motion. Fluid forces, such as the propulsive and drag forces could be calculated from body motion so that the most efficient swimming

motion could be acquired. In addition, the present system has the special function to cooperate with the swimming human simulation model SWUM, which was developed by Nakashima et al. [61]. By using SWUM, the fluid forces acting on a swimmer can be quantified and visualized. Such results will be useful information for athletes and coaches. In the present study, the butterfly stroke was taken as the targeted stroke, since it is considered a bilaterally-symmetric motion [82].

The butterfly stroke of swimming is a symmetrical stroke where the upper and lower body movements on the right will move together with the left side of the body. In addition, the body does not perform rolling movements such as freestyle swimming and backstroke but undulation movements up and down. Therefore, the butterfly stroke is often referred to as an undulation stroke. Undulated movements of body segments in skilled swimmers resemble the movement of water waves from head to toe [83]. Generally, this butterfly movement can be divided into five phases: release and recovery, entry, outsweep and catch, Insweep, and upsweep. The release and recovery phase occurs when the hands release the water at the end of their pull and start the over-water recovery in preparation for the next pull. When starting the entry phase, the combination of forward rotation of the body and the effect of gravity makes the upper body move downwards. At this point, the elbow should be high enough and the forearm moving forward to avoid sweeping the water. Then at the beginning of the outsweep, so called because the arms sweep outward rather than backward, the arms have reached forward, the trunk is angled downward, the hips are elevated, and the legs are up near the surface. In the insweep phase, both arms move together and there is no body roll about the longitudinal axis of the body. Swimmers will flex their elbows and combine shoulder movements with internal rotation, horizontal adduction, and extension to produce great hand speed and, therefore, strong propulsive forces. The upsweep is a strong backward push that also brings the hands toward the surface. This action is fast and strong, and the hands accelerate progressively through the upsweep.

3.2 Methodology

The methodology used in developing a registration-based markerless optical motion capture system for bilaterally symmetrical swimming stroke movements is similar to that in running movements. However, there are some differences considering the swimming movement is occurred in the water. In addition, the dynamic analysis for swimming movements

is more complex because of its three-dimensional movement and the forces resulting from the interaction of the swimmer's body and the water. The interaction force is in the form of lift and drag force which will produce a propulsive swimming force.

The methodology developed for bilaterally symmetrical swimming stroke movements is (1) requirements for SWUM analysis, (2) segmentation of the participant's silhouettes, (3) model generation, (4) image matching, and ends with (5) dynamic analysis using SWUM. In the present work, the butterfly stroke was taken as the example of the bilaterally symmetrical swimming stroke.

3.2.1 Requirements for SWUM Analysis

SWUM is a powerful analysis tool for various dynamical problems in human swimming developed by Nakashima et al [61]. In SWUM, swimming motion's kinematics and kinetics parameters could be calculated from relative body motions (joint angles) using the equations of motions for fluid force and body inertia. The software and three-dimensional joint motion of the butterfly strokes are freely available on http://www.swum.org/swumsuit/index.html [84]. The joint motion was obtained from a video of "model swimming" [85], which was made by the Japan Swimming Federation, and is open to the public on the internet. In this research, this available joint motion was used as a priori information of kinematics data for the butterfly stroke's motion. SWUM was also employed in calculating the kinematics and kinetics parameters of the swimming motion.

Unlike the running motion which could be considered as a movement in two dimensions, the butterfly stroke has movements that work in three dimensions, especially the movement of the hands. The system developed in this study used only one camera, so data collection could be done simply and quickly. However, the use of a single camera could generally only analyze motion in two dimensions. Therefore, this study used the butterfly stroke movement database available in SWUM, so dynamic analysis could still be carried out even if only using one camera.

The dynamic analysis by SWUM or shortly SWUM analysis requires several data. The first is the segment angle in three planes: sagittal, transverse, and frontal. The segment angle in the sagittal plane could be obtained from the developed markerless optical motion capture data. Then, the segment angle in transverse and frontal plane could be obtained from the

SWUM database. Beside the segment angle, the other data required for SWUM analysis were the velocity of center of mass for the butterfly stroke and the anthropometry of the participant.

3.2.2 Segmentation of the Participant's Silhouettes

The idea of segmentation is to obtain the participant's silhouettes for each video frame. The participant's body is extracted from the background so that the participant's movement for each frame could be estimated. Image thresholding was used for segmentation in this work because of its simple implementation and time saving [86]. The optimum threshold value could be obtained by using the Otsu Method [87]. Image thresholding might be applied to the blue color channel of the frame due to its significant contrast between the participant's body and the environment.

To compensate for the non-uniformity of illumination on the image, variable thresholding was applied in the process of segmentation. One of the simplest approaches to variable thresholding was to subdivide an image into non-overlapping rectangles [88]. The threshold value in the region that had darker lighting was set smaller than the other regions. Moreover, the region above the water surface could be set as the background, as that region was not of interest. The result of the image segmentation is called as the silhouette image and mathematically is written as $f(u, v)$.

3.2.3 Model Generation

The model represents the prior knowledge available about the participant's morphology and kinematics. The model generation for the bilaterally symmetrical swimming stroke was similar with that in the Section 2. The model was obtained from a swimming frame that contained a complete body segment. The identification of each body part was also conducted manually to enhance the accuracy. The main difference in the model of this movement compared to the running movement is the right and left segments. Since the movement of the right and left sides of the body in the butterfly stroke is basically the same and synchronized, the right and left segments were considered the same. All generated body segments are stored in the form of an image model. The model image, $g(u, v)$, is the image of a generated model that will be transformed and registered to the silhouette images. The joint positions could also be determined by looking for the centroid of the intersection between two body parts.

3.2.4 Image Matching

After the participant's silhouettes and model were established, the next step was to match the model to the participant's silhouettes so that the pose of the silhouettes could be estimated. The image matching procedure for butterfly stroke was similar with that was in the running motion (Section 2.2.3). Prior to the image matching, proper features must be decided. The features must be easily detectable objects in both the model and silhouette images. In this research, the shape of the human body in the silhouette and the model were employed as the feature for the image-matching task because it was independent of the change of illumination [57].

Matching the model to the silhouettes was conducted by mapping the model so that it aligned with the silhouettes. The similarity of intensity value between the mapped model and the silhouettes was investigated to ensure good results of image matching. In measuring the similarity, each pixel of the swimming data and the transformed model were compared. Similarity will increase if the same pixel location in both images has the same intensity value.

In model mapping, the shape of each segment and their kinematic links are preserved. Then, all the points belong to each body segment in the model image, (u_n^i, v_n^i), were transformed in translation and rotation. Note that i is the segment number and n denotes the number of points for each segment. The segment transformation in the model image follows Equation 1 – 5 with the extension of the number of segments. Then, the segment angle could be evaluated by solving Equation 6 – 8 by an optimization method. In the optimization, the standard segment angle of butterfly stroke in SWUM could be used as a priori information in the tracking process and as a kinematic and kinetic analysis tool. Consequently, the data in SWUM and the experiment should be correlated. In addition, two issues should be adjusted in SWUM, i.e., the number of body segments and the swimming phase.

3.2.5 Dynamics Analysis by SWUM

The results of image matching, such as the angle of each segment and the joint position of the trunk, were used to conduct a dynamics analysis of the butterfly stroke by SWUM. Prior to performing the dynamics analysis, the missing angles in some frames, shown in Figure 3.7, were interpolated by the smoothing spline curve fitting method. Direct Linear Transformation

(DLT) parameters to convert the joint position in the image coordinate to the world coordinate were obtained by the method proposed by Kwon [89]. The velocity of the center of the mass was then derived from the world coordinate of the trunk position.

In camera calibration, the position of control points in image and world coordinate should be known exactly. The world coordinate of control points is obtained from measurement. The number of control points determines the accuracy of camera calibration. The higher number of control points will increase the accuracy. The image coordinate (*u, v*) and world coordinate (*x, y*) of control points is used to calculate DLT parameters (L_1 - L_8) by solving Equation 9 and 10 below. The control points used in this research could be the joints of subject's body.

$$u = \frac{L_1 x + L_2 y + L_3}{L_7 x + L_8 y + 1} \tag{9}$$

$$v = \frac{L_4 x + L_5 y + L_6}{L_7 x + L_8 y + 1} \tag{10}$$

The segment angle obtained from this work was two-dimensional. However, the swimming motion, in fact, took place in a three-dimensional space, especially in the outsweep and insweep cycle. For that reason, the rotation angle of the upper limb in the transverse and frontal planes were imported from the three-dimensional joint motion of the butterfly strokes available on the SWUM website [84]. The inclusion of movement in the frontal and transverse plane from the available joint motion was conducted to show the capability of the system. Although the joint motion in the frontal and transverse plane was obtained from different swimmers, the calculation result is still useful for feedback to athletes and coaches since the sagittal plane motions are considered the most important in swimming. However, the user of this system does not always have to combine the obtained motion with different swimmers' motions. For example, the user can film the swimmer's motion from the front to obtain the frontal and transverse motions first. Then, for daily training, the user can save time by using the pre-acquired frontal and transverse motions and combine them with sagittal motion observed on the training day.

The upper limb motion available in SWUM homepage is the combination of rotation in three axes. The definition of axis could be seen in Figure 3.6. For example, the rotation angle of forearm is a sequential rotation in the order of *z*, *y*, *z*, *x*, *z*, *y*-axis. Therefore, the order of

rotation of upper limb should be modified so that the rotation angle in transverse and frontal plane should not affect "observable rotation angle" in sagittal plane. For that purpose, the order of rotation of upper limb is modified so that in the order *z*, *x*, and *y*-axis.

The procedure of modifying the rotation order of upper limbs was initiated with expressing the length of upper limbs as a vector. Then, the rotation matrix $\boldsymbol{R}$ of upper limbs could be calculated based on the order that are available in SWUM's database. On the other hand, the rotation matrix $\boldsymbol{R}$ could be also derived from new order rotation shown in Equation 11 below.

$$\boldsymbol{R} = \boldsymbol{R_z}(\gamma)\boldsymbol{R_x}(\alpha)\boldsymbol{R_y}(\beta) \tag{11}$$

Equation 11 could be expanded into Equation 8 by multiplying the rotation matrix about *z*, *x*, and *y*-axis.

$$\boldsymbol{R} = \begin{bmatrix} \cos\beta\cos\gamma + \sin\beta\sin\alpha\sin\gamma & -\cos\beta\cos\gamma + \sin\beta\sin\alpha\sin\gamma & \sin\beta\cos\alpha \\ \cos\alpha\sin\gamma & \cos\alpha\cos\gamma & -\sin\alpha \\ -\sin\beta\cos\gamma + \cos\beta\sin\alpha\sin\gamma & \sin\beta\sin\gamma + \cos\beta\sin\alpha\cos\gamma & \cos\beta\cos\alpha \end{bmatrix} \tag{12}$$

The rotation angle α, β, and γ could be obtained by using known matrix $\boldsymbol{R}$ and Equation 12 as below.

$$\beta = \tan^{-1}\left(\frac{r_{13}}{r_{33}}\right) \tag{13}$$

$$\alpha = \tan^{-1}\left(\frac{-r_{23}}{r_{13}\sin\beta + r_{33}\cos\beta}\right) \tag{14}$$

$$\gamma = \tan^{-1}\left(\frac{r_{32}\sin\beta - r_{12}\cos\beta}{r_{11}\cos\beta - r_{31}\sin\beta}\right) \tag{15}$$

where r_{ij} denotes the element of matrix $\boldsymbol{R}$ in row *i* and column *j*. Then, Equation 13 to Equation 15 was applied to the upper arm, forearm, and hand to obtain the resultant rotation angle for each plane. Then, the resultant rotation angle was inputted to dynamics analysis procedure.

3.3 Experiment

In this research, the development was initiated with the acquisition of the butterfly stroke motion. One 60-frame-per-second camera was operated to record the swimming motion on the sagittal plane inside the water without any specially arranged lighting. The camera was positioned 4.5 meters from the left side of participant and 0.75 meters below the water surface.

There was no required camera arrangement for the image acquisition as long as the camera could record a minimum of two strokes of swimming motion in the sagittal plane and the camera was not moved during the process of acquisition. The image frames obtained from the video, as shown in Figure 3.1, were segmented to obtain the silhouettes of the participant.

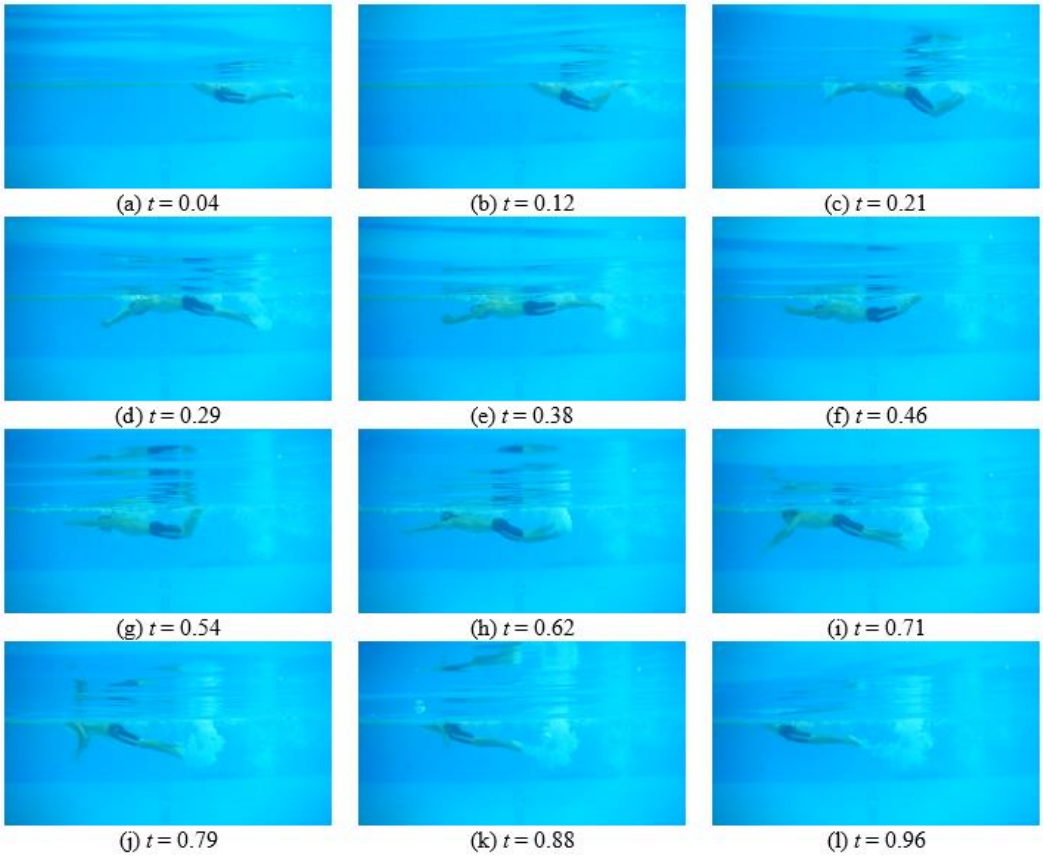

Figure 3.1 Swimming frames recorded by a static camera at 60 frames per second. Each frame was labeled by non-dimensional time normalized by the stroke cycle.

An image-matching algorithm was employed to track the motion of the silhouettes with the aim of attaining the movement of each body segment of the participant. In predicting the movement of each segment of the participant, the model to help the tracking process was generated. The model contained prior knowledge of a participant which could be used to constrain the tracking and pose estimation process [36]. Hence, the degree of freedom in estimating the motion of the silhouettes could be reduced so that the computing cost of a tracking process could be minimized. The silhouettes of each frame and the model were matched by using the algorithm described in this paper. The following sections explain the steps required to obtain the kinematic parameters of the butterfly strokes of the participant.

3.4 Results dan Discussion

In this sub-chapter, the results of image matching algorithm are described comprehensively. Then, the results of image matching are further analysed to obtain the dynamics parameter by SWUM.

3.4.1 Segment Angle of Butterfly Stroke

The output of the experiment explained in the Section 3.3 were the swimming images that were in the RGB format and resolution of 1280 x 760 pixels. The RGB images were then extracted into three color channels, as depicted in Figure 3.2. The variable thresholding described in Section 3.2.2 were applied at blue color channel to obtain the silhouette images of the swimmer. Mathematically, the silhouette images were denoted by $f(u, v)$. The result of the image segmentation in this research is shown in Figure 3.3.

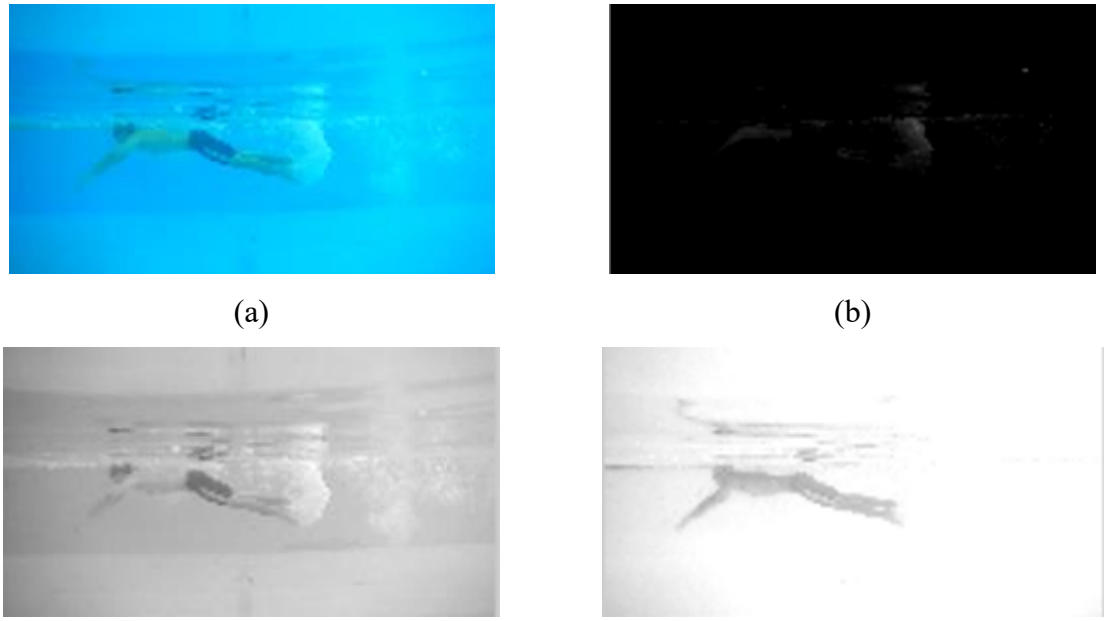

(a) (b)

(c) (d)

Figure 3.2 The contrast of silhouettes: (a) original image, (b) red color channel, (c) green color channel, (d) blue color channel

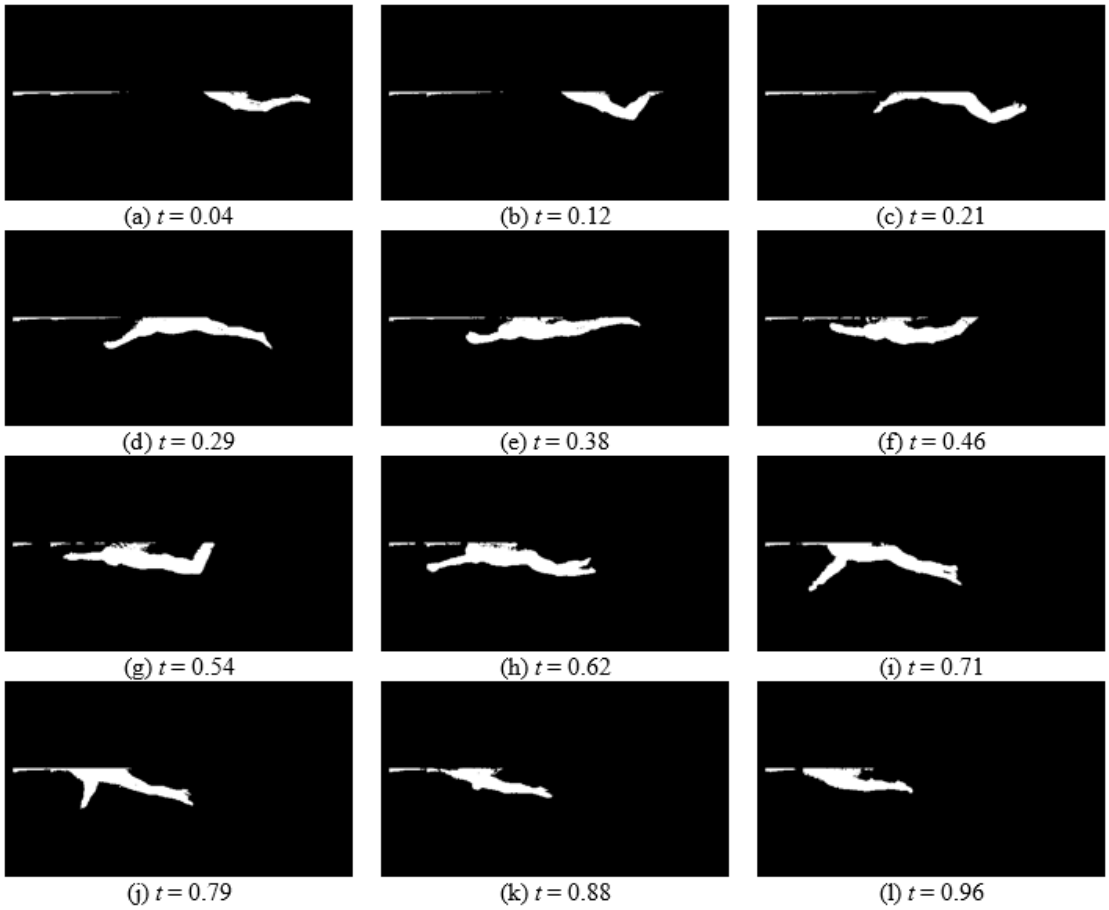

Figure 3.3 Participant's silhouettes obtained by variable thresholding on the blue color channel of swimming frames. Each frame is in non-dimensional time.

One of the frames in the swimming images with complete segment was used to generate the human body model. The frame was segmented manually to obtain the subject's silhouettes in more accurate. For the butterfly stroke, the segmented body was numbered from i = 1 to 9 for the head, trunk, hip, thigh, shank, foot, upper arm, forearm, and hand, respectively. Figure 3.4 shows the generated model used in the butterfly stroke. In the body-part segmentation and identification, the neck was not modeled as one of the body parts because the movement of the neck was not significant in swimming motion. The position of joints was obtained from the centroid of the overlapped region between two segments. The joint positions are indicated by * marks in Figure 3.4. All the segments and joint position of the model was stored as the model image, written as $g(u, v)$.

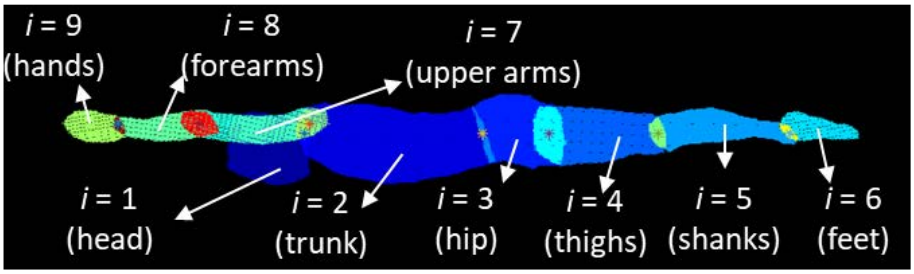

Figure 3.4 The model used in the tracking process, made of 9 body segments. The * marks indicate the position of the model's joints.

In the model image, there are points belongs to i^{th} segment with image coordinate (u_n^i, v_n^i) for $i = 1, \ldots, 9$ and $n = 1, \ldots, N_i$, where N_i is the total number of points for i^{th} segment. The pixel or point with coordinate (u_n^i, v_n^i) has white color or intensity value one. Then, those points were transformed based on Equation 1 – 5. Since the subject's body was modelled as nine segments, then the transformation parameters involved in the image matching for the butterfly stroke were $T = [t_u, t_v, \theta^1, \ldots, \theta^9]^T$. To obtain optimum transformation parameter so that the transformed model image overlapped perfectly with the silhouette image, particle swarm optimization technique was used in this work to minimize the objective function (Equation 7).

One of the contributions of the present research is the use of SWUM as a priori information in the tracking process and as a tool for the kinematic and kinetic analysis. Consequently, the data in SWUM and the experiment should be correlated. There were two issues that should be adjusted in SWUM, i.e., the number of body segments and the swimming phase.

A human body model in the current development consisted of nine segments. However, the number of segments in SWUM was 21 segments. Thus, the number of segments in SWUM had to be adjusted to become nine segments. The adjustment of segments in SWUM was conducted by combining the neck, shoulder, upper breast, lower breast, upper waist, and lower waist of SWUM into the trunk, as shown in Table 3.1. The motion of the trunk was set using the average motion of the neck, shoulder, upper breast, lower breast, upper waist, and lower waist.

Table 3.1 Adjustment of body's segment in SWUM

Segment in Swimming Data	Segment in SWUM
Head	Head
Trunk	Neck, shoulder, upper breast, lower breast, upper waist, lower waist
Hip	Upper hip, lower hip
Thigh	Thigh (R = L)
Shank	Shank (R = L)
Foot	Foot (R = L)
Upper arm	Upper arm (R = L)
Forearm	Forearm (R = L)
Hand	Hand (R = L)

Prior to adjusting the swimming phase, the number of frames for one cycle of swimming in the experiment and SWUM was adjusted to be 24 frames per swimming cycle. Since the number of frames of both the experiment and SWUM were the same, a frame in the experiment could correspond precisely with one in SWUM. To do so, the key frame between SWUM and the experiment should be obtained by using the trajectory of the lowest body part in the vertical direction both for SWUM and the experiment shown in Figure 3.5. The key frame is the frame number of SWUM and the experiment which has the same swimming phase, whether on the upper limb or lower limb, to synchronize the motion in SWUM and the experiment. With the same phase, the rotation angle of the body part in SWUM is exploited as the lower and upper boundary in the optimization.

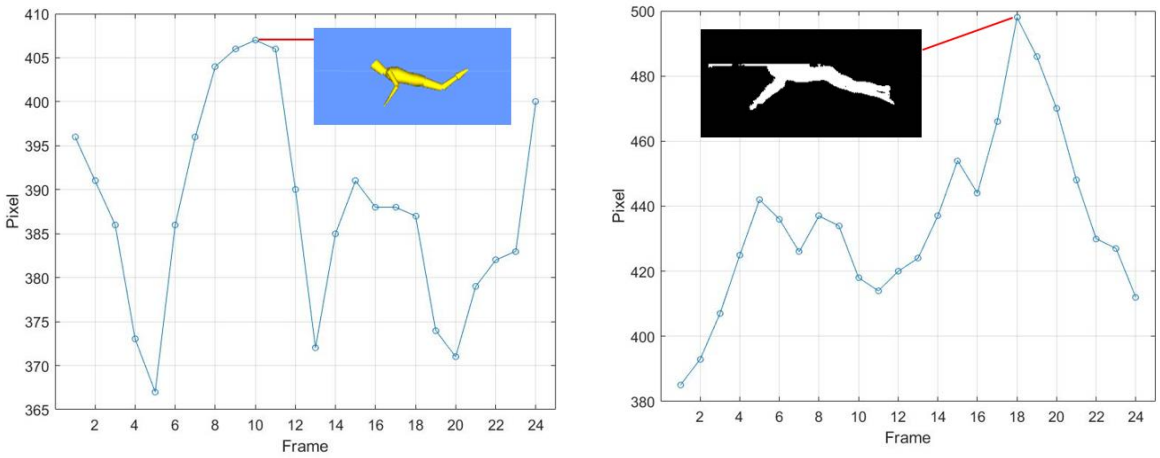

(a) (b)

Figure 3.5 Obtaining the key frame between the experiment and SWUM by the trajectory of the lowest body part in the vertical direction in (a) SWUM and (b) the experiment. The key frame is the frame number of SWUM and the experiment which has the same swimming phase

Prior to the optimization, the rotation angle of upper limbs in sagittal plane of SWUM should be further calculated because the movement of upper limbs in SWUM occurs in the frontal, transverse, and sagittal plane. Hence, the movement of upper limbs in sagittal plane of SWUM could not be directly used as the priori information in the tracking process.

To obtain correct rotation angle of upper arm, forearm, and hand, the length and consecutive joint motion of related body part are required. Prior to obtain correct rotation angle of upper limb, the initial orientation of body in SWUM have to be identified first. From Figure 3.6, it can be recognized that sagittal plane is plane x_b-z_b and the longitudinal axis of body is in the z_b direction. Therefore, the length of i-th body part (b_i = 5, 6, 7) can be expressed as a vector in z_b direction ($\mathbf{v}_{bi}$).

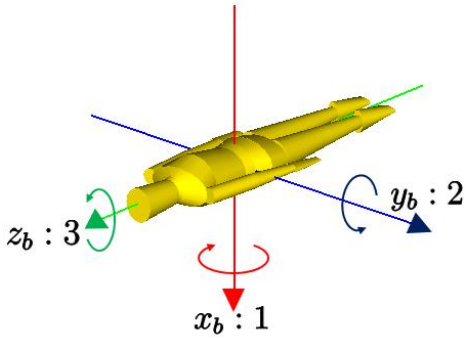

Figure 3.6 Initial orientation of body in SWUM

The orientation of upperlimb in sagittal, frontal, and transverse plane then is projected orthogonally to sagittal plane for each frame. The orthogonal projection for each frame of upperarm, forearm and hand can be written mathematically as

$$\mathbf{v}'_{bi} = \mathbf{T_o R v}_{bi} = \begin{bmatrix} 1 & 0 & 0 \\ 0 & 0 & 0 \\ 0 & 0 & 1 \end{bmatrix} \mathbf{R} \begin{bmatrix} 0 \\ 0 \\ l_{bi} \end{bmatrix} \quad \text{for } i = 5, 6, 7 \tag{8}$$

which $\mathbf{T_o}$ is orthogonal projection matrix on the x_b-z_b plane, $\mathbf{R}$ is resultant rotation matrix of body part b_i for each frame and $\mathbf{v}_{bi}$ is the length of body part (l_{bi}) expressed in vector form. The resultant rotation matrix $\mathbf{R}$ can be generated from joint motion of SWUM. The rotation angle of body part observed on sagittal plane is calculated by using inverse tangent of $\mathbf{v}'_{bi}$. The observable rotation angle in sagittal plane of SWUM for upper limbs resulted from orthogonal projection were then used to define upper and lower boundary in the optimization procedure.

As a reference for evaluating the result, each segment of the model was transformed manually in the Graphical User Interface (GUI) of image matching developed before so that the whole segment of the model matched perfectly with the silhouettes. The transformation

parameters obtained from the GUI were used to evaluate the result of the image-matching algorithm developed in this research. The result of the image-matching algorithm and the reference is shown in Figure 3.7.

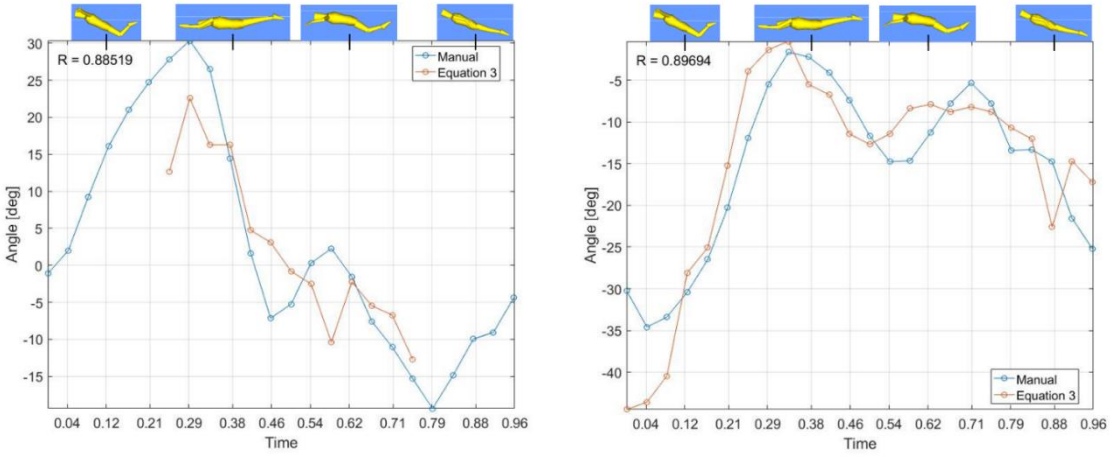

(a)

(b)

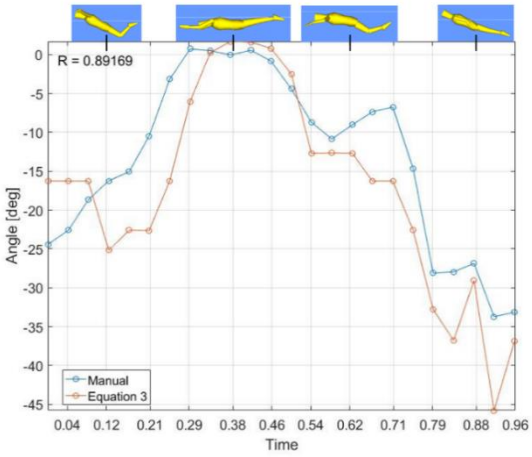

(c)

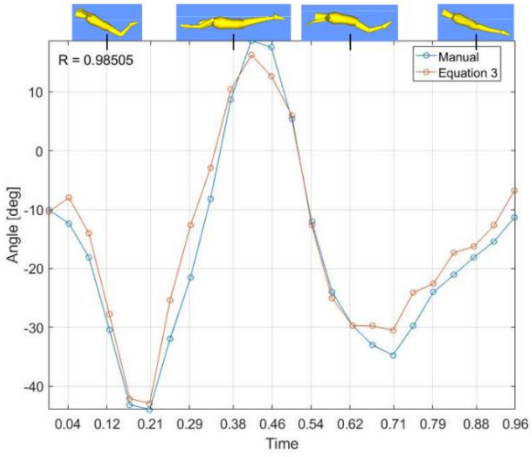

(d)

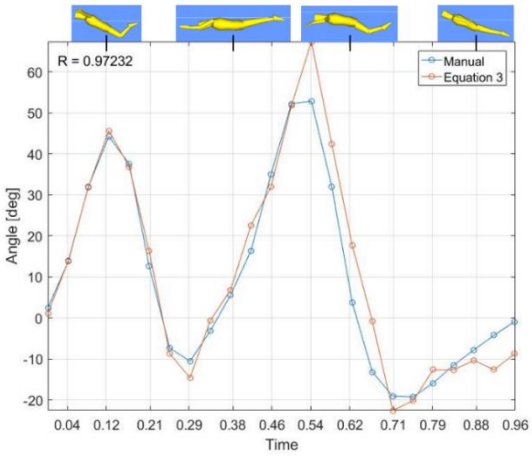

(e)

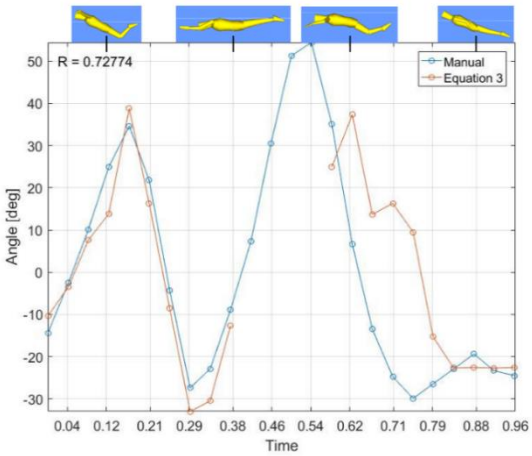

(f)

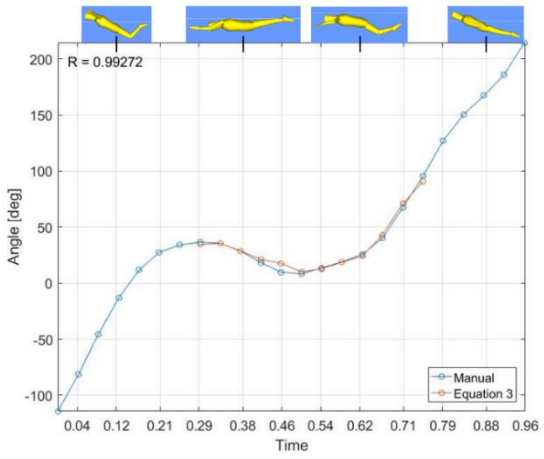

(g)

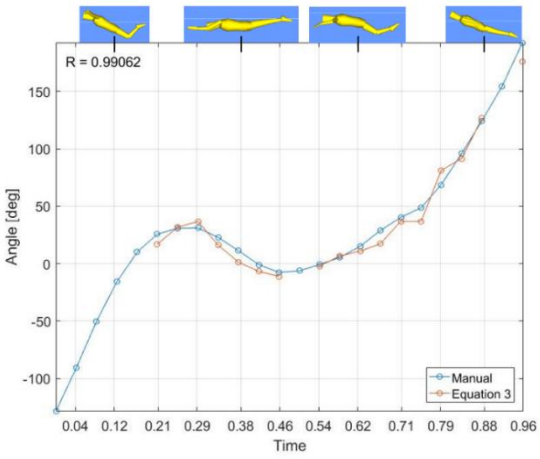

(h)

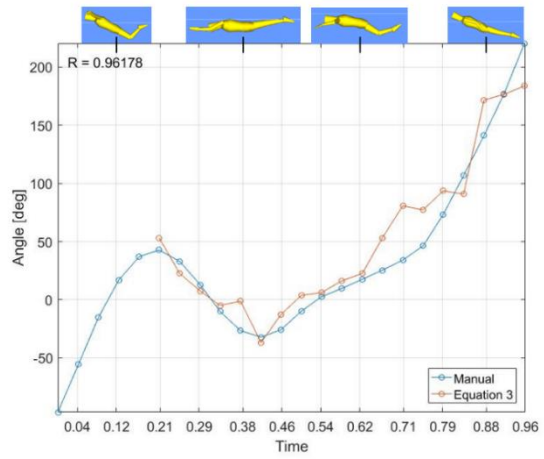

(i)

Figure 3.7 The results of the image matching algorithm in which the rotation angle of each segment of body is shown compared to the reference: (a) head, (b) trunk, (c) hip, (d) thigh, (e) shank, (f) foot, (g) upper arm, (h) forearm, and (i) hand. A schematic annotation swimmer is provided in each graph. The time scale in the *x*-axis corresponds to the swimming frame of Figure 3.1

Figure 3.7 shows that there are some missing data on some frames of rotation angle, especially in the head, foot, upper arm, forearm, and hand. These missing data are the result of those segments being above the water surface so that their motion could not be recorded by the camera. However, since there will be no interaction force between the body and the water when the participant is outside the water, the missing data will not affect the kinematic and kinetic analysis conducted by SWUM.

The correlation coefficient *R* between the references and the result was calculated to examine the accuracy of the developed markerless optical motion capture system for the

butterfly swimming stroke. The coefficient correlated the rotation angle of a body segment obtained from the image matching algorithm and references. An image-matching algorithm was performed ten times to investigate the reliability of the algorithm. The computational time was around 1 hour 50 minutes for the whole cycle of swimming. With the long computational time, the system could not give the result in real time. However, the proposed system could provide the swimmer's body motion in the same day, which is much shorter than the time required for manual tracking. The correlation coefficients and their standard deviations are summarized in Table 3.2.

Table 3.2 Summary of correlation coefficients between the result and reference. The coefficients correlate the rotation angle of the body segment obtained from the image matching algorithm and reference.

Body Segment	**R**	**ΔR**
Head	0.789	0.044
Trunk	0.929	0.021
Hip	0.784	0.059
Thigh	0.974	0.011
Shank	0.942	0.022
Foot	0.784	0.073
Upper arm	0.984	0.007
Forearm	0.985	0.008
Hand	0.950	0.020

Generally, Table 3.2 shows promising results of matching the model to the participant's silhouettes in order to obtain the rotation angle of each body segment. However, the results for the foot, head, and hip are not in line with expectations. The foot and head are located at the end or tip of the human body. Their shapes were blurred by the presence of bubbles while the participant was swimming. Therefore, matching for both the foot and head could not be completed well. The hip also experienced poor matching because it rotated slightly relative to the trunk. Hence, it was difficult to differentiate between the trunk and hip in the matching process.

3.4.2 Dynamics Parameters by SWUM

In conducting the camera calibration, there were five control points used in the present work, i.e., points with number 1 to 5 as shown in Figure 3.8. The image and world coordinate of those control points were summarized in Table 3.3. The world and image coordinates of control points in Table 3 were utilized to obtain DLT parameters by using Equation 9 and 10. Then, the positions of joint shown in Figure 3.9 were calculated with the help of their image coordinate and DLT parameters to investigate the accuracy of the camera calibration. Table 3.3 shows the result of 2D reconstruction in the link's length form which implies acceptable accuracy of camera calibration.

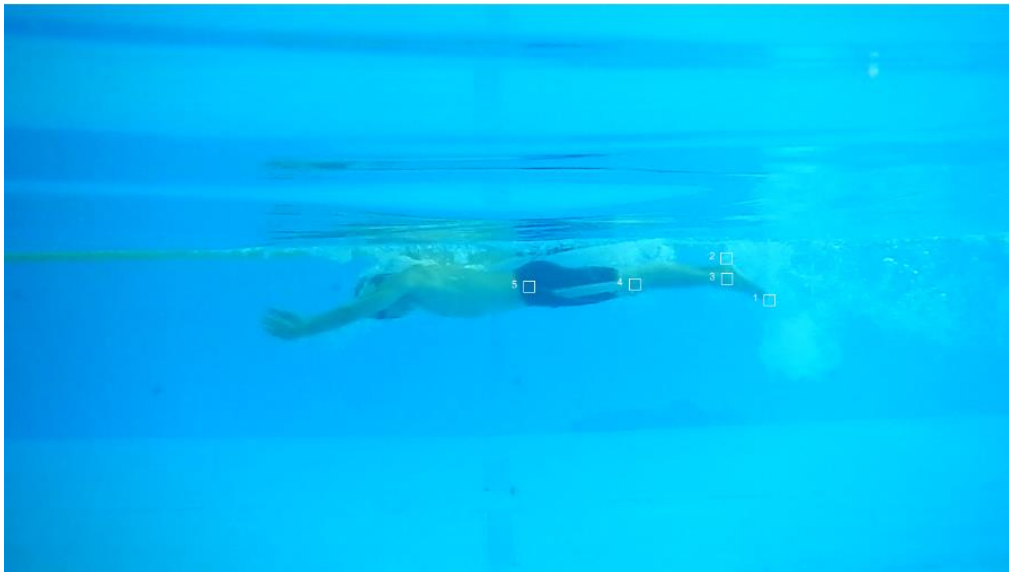

Figure 3.8 Image of control points used in present work

Table 3.3 The world and image coordinate of control points

Control Points	World Coordinate [mm]		Image Coordinate [pixel]	
	x	y	u	v
1	0.00	0.00	972	376
2	-169.22	163.06	917	323
3	-178.89	89.44	918	349
4	-598.14	64.36	801	356
5	-1068.02	53.84	667	359

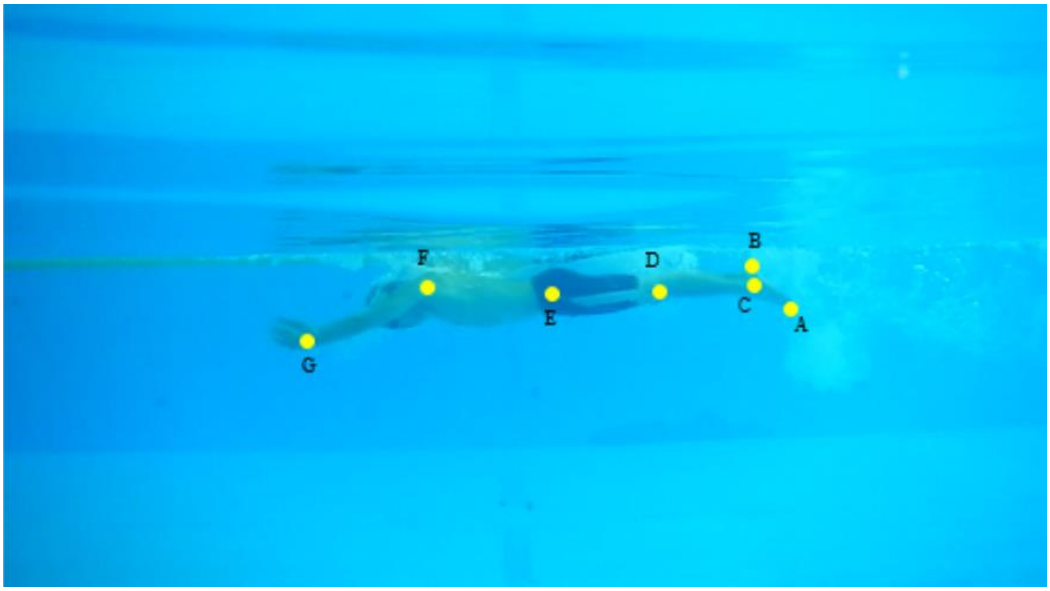

Figure 3.9 Joint position of subject

Table 3.4 Result of reconstruction

Link	Reconstructed Length [mm]	Measured Length [mm]
AB	235	238.598
AC	200	200.3597
BC	100	72.06247
CD	420	422.8629
DE	470	467.2098
EF	490	485.8662
FG	530	511.8457

Figure 3.10 shows the simulation results of the butterfly stroke with lines representing the fluid forces on that segment. In addition, the velocity of the center of the mass, the fluid force acting on the right lower and upper limbs in the propulsive direction, are presented in Figure 3.11 – Figure 3.13, respectively. In Figure 3.11, it can be observed that there were two large peaks in the whole cycle which started at $t = 0.15$ and $t = 0.53$, occurring at $t = 0.26$ and $t = 1.00$, respectively. Note that t is the non-dimensional time normalized by the stroke cycle. The first peak was produced by the kick motion of the lower limb (see Figure 3.12). The second largest peak was generated by the combination of the kick motion of the lower limb and the catch motion of the upper limb. From Figure 3.12, it can be noticed that the kick motion at $t = 0.55$ produced the thrust and then it directly continued through the catch motion of the upper limb at $t = 0.65$ in Figure 3.13. In addition, it is also found that all the thrust from the upper limb was due to the normal drag force, and the thrust by the lower limb was generated by the inertial force due to added mass and the normal drag force.

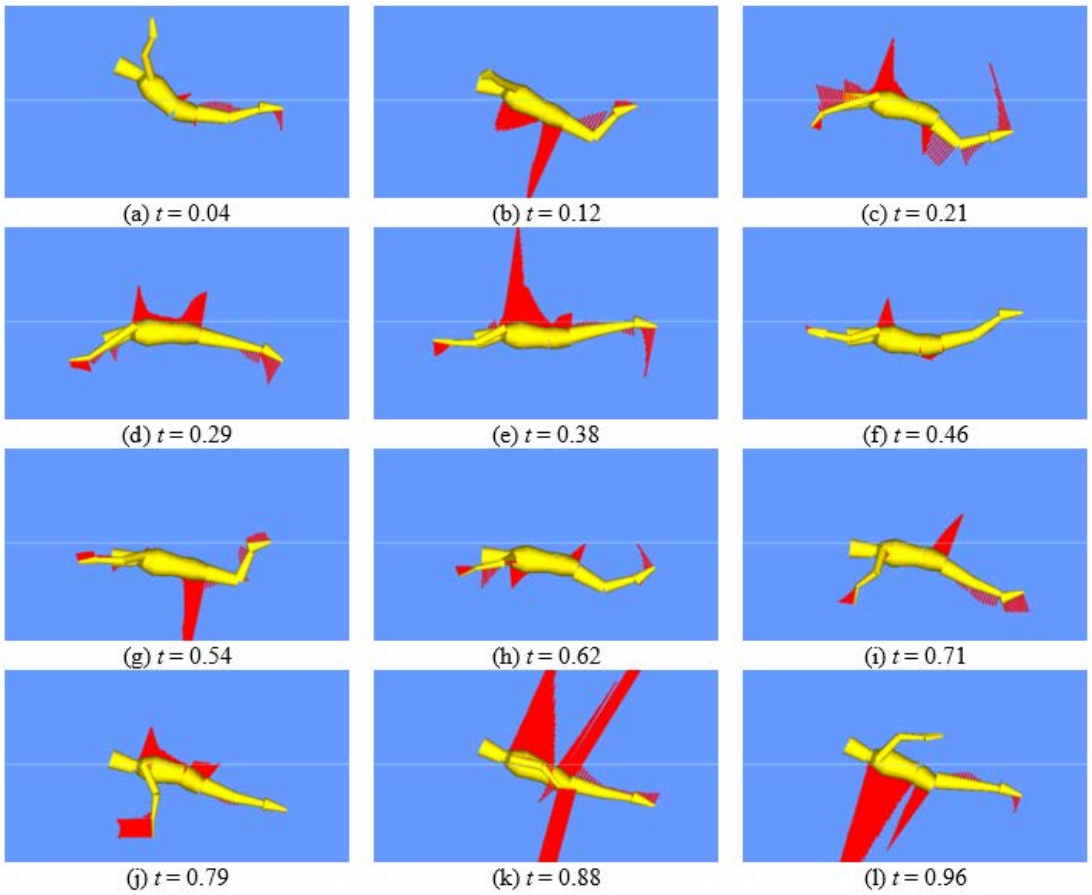

Figure 3.10 Simulation results of the butterfly stroke swimming motion for one cycle from the side view with non-dimensional time. The lines in the simulation results represent the vectors of fluid forces on the segments.

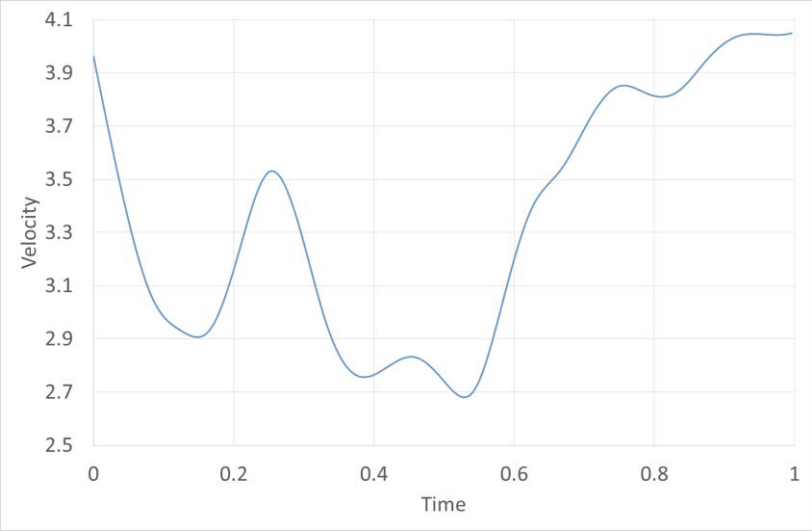

Figure 3.11 Velocity of the center of mass in the propulsive direction of the butterfly stroke obtained from the experiment.

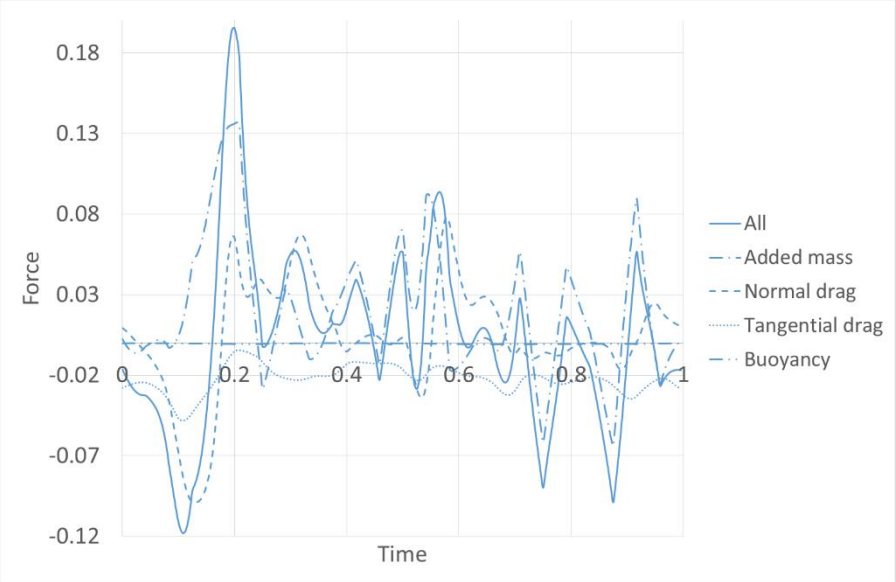

Figure 3.12 Fluid force acting on the right lower limbs in the propulsive direction of the butterfly stroke, calculated by SWUM. The kick motion generated two large peaks of swimming velocity, which started at t = 0.15 and t = 0.53, respectively.

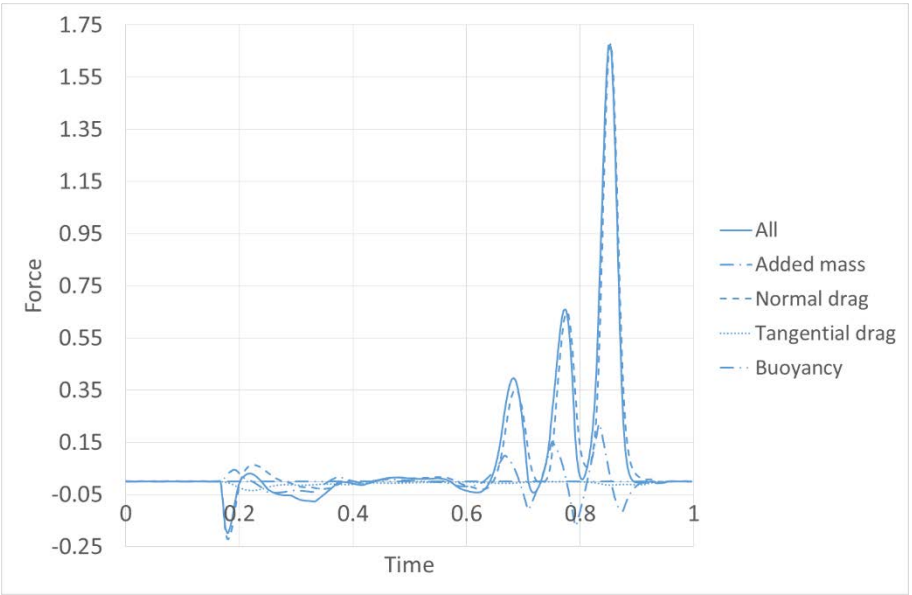

Figure 3.13 Fluid force acting on the right upper limbs in the propulsive direction of the butterfly stroke which was calculated by SWUM. The catch motion at t = 0.65 contributed to the second large peaks of swimming velocity.

The fluid force data calculated by SWUM from the body motion of a swimmer are useful for athletes and coaches in daily training. They could modify the motion of a body

segment based on analysis information in the style of the present work to enhance the swimming velocity. For example, the rotation angle of the hand when t = 0.88 (see Figure 3.10) should be smaller. In order to produce propulsive force efficiently, the hand angle should be around 90 degrees, that is, the hand should be vertical. However, the angle of the participant was about 150 degrees. This means that the participant pushed the water upward. Therefore, it can be suggested to the participant that the hand should be more extended.

3.5 Conclusion

In this chapter, the development of a markerless optical motion capture system for swimming motion has been presented. Generally, the system began with the swimming motion acquisition by using one underwater camera. The swimming images then were segmented by variable thresholding to obtain the participant's silhouettes. A model was also generated to assist with the tracking and pose estimation process so that the rotation angle of each body segment could be obtained. The rotation angle as well as the velocity of the center of mass were put into the swimming human simulation model for a dynamics analysis. Simulation results show that the velocity obtained in the experiment corresponded to the fluid force exerted on the lower and upper limbs. The main advantage of this system is that it is relatively simple and cheap. Moreover, the system also provides semi-automatic tracking instead of manual tracking to reduce the processing time of swimming motion analysis. It is expected that the proposed system could be used by athletes and coaches for daily training in a shorter time than the use of manual tracking to obtain a swimmer's body motion.

Chapter 4
Extension to Asymmetrical Swimming Stroke

4.1 Introduction

In the Chapter 3, it has been explained that the markerless optical motion capture system has been used for the analysis of the butterfly style swimming motion. The developed method could be used to study any bilaterally symmetrical motion. However, the application of the developed system for asymmetrical swimming strokes was still in question. The main reason for this limitation is the number of links in the human body model, and it cannot distinguish the right and left sides of the body segment. Hence, the main objective of the present work was to improve the developed system so it can be used to obtain joint angle and dynamics parameters for asymmetrical swimming strokes. The improvement of the present study was the adjustment of the human body model and the inclusion of an algorithm to identify the right and left body segments. As a case study, the front-crawl stroke motion was investigated in the experiment for markerless analysis. The main contribution of the developed system is to decrease the required time to analyze the swimming movement, especially asymmetrical strokes. Compared to manual digitizing, which can take several days, the system could obtain the front-crawl kinematics data in just one hour.

There are four phases in the front crawl stroke cycle, divided based on the upper limb's movements, as seen in Figure 4.1. According to Pink M, et al. the upper limb position marks each phase, i.e., (1) Early pull-through phase begins right after the arm enters the water and extends forward in front of the shoulder, (2) Late pull-through phase starts after the arm is perpendicular to the body at which point is called the mid pull-through, (3) Early recovery phase begins after the arm exits the water until the elbow reaches the highest point above the surface of water, and (4) Late recovery phase follows the end of early recovery phase until the arm is swung above the water to bring the arm into position to the pulling phase once again in the next cycle [90]. The four phases could be simplified into two major phases: pull-through and recovery. Pull-through is essentially a propulsive act of the subject to move through the water. This means the phases aligned with the definition of swimming proposed by Shinichiro

Ito and Keisuke Okuno that described swimming as series of propulsive and recovery movements [91].

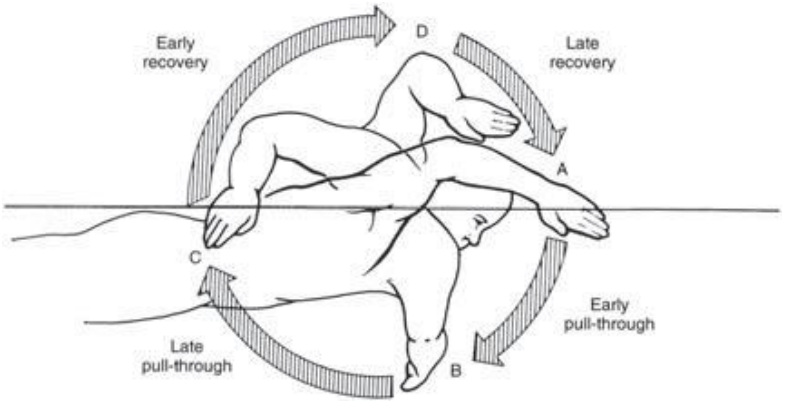

Figure 4.1 Phases of Front Crawl Swimming Stroke [90]

4.2 Methodology

The methodology in developing a markerless optical motion capture system for asymmetrical swimming stroke was slightly different compared to bilaterally symmetrical swimming stroke. The main challenge in this swimming movement was the different movements of the left and right parts of the body, so an algorithm was needed to distinguish the left and right limbs. In addition, the kicking movement was more powerful, producing more bubbles. The presence of these bubbles made the image segmentation process more difficult. The methodologies were discussed in developing the system for this movement is (1) human body model generation, (2) image segmentation, (3) image matching, and (4) identification of right and left limb.

4.2.1 Human Body Model Generation

Since human movement has many degrees of freedom, a human body model is required. The model contains a priori information about the participant's body shape to be matched with real images of the participant [40], [92]. As a result, the movement of the participant's body segments could be obtained.

Human body models can be generated from a morphological description of the human body's anatomy [37]. The best way to generate a model is from direct measurement of the participant's outer body surface. Therefore, the model in this research was extracted from a

swimming frame that included all body segments. Manual image segmentation was conducted to exclude the participant's body segments from the environment. Joint positions should also be defined in the model as the center of rotation of each body segment. The joint positions can be obtained from the centroid of the intersection of two segments. The generated model, including the joint position was saved as a image, called as model image, $g(u, v)$. In the model image, there are points belong to each segment, (u_n^i, v_n^i) for $i = 1, \ldots, 8$ and $n = 1, \ldots, N_i$, where N_i is the total number of points for ith segment, so that $g(u_n^i, v_n^i) = 1$.

4.2.2 Image Segmentation

In this procedure, the silhouette of the participant was obtained to be used for the image matching step. The input for the image segmentation procedure were RGB images that were extracted from the recorded video of the participant swimming. The image segmentation process for swimming application is more challenging due to bubbles resulting from the flutter kick. Therefore, in the present work, the image segmentation was conducted using an adaptive background Gaussian Mixture Model (GMM) [93].

In the application, the blue channel of RGB was used in the image segmentation procedure since the participant's silhouette has the most contrast against the background in the blue channel. Then, the intensity value of the bubbles was modeled as a GMM component, so that the bubbles could be interpreted as background. To enhance the image quality, a morphological operation was applied. The higher image segmentation accuracy increases the developed system's accuracy. One of the methods to enhance the system's accuracy is to increase the participant's contrast with the environment. Hence, the accuracy of the image segmentation could be improved. The result of the image segmentation was called as silhouette image. Similar to description in Section 2, the silhouette image is denoted by $f(u, v)$.

4.2.3 Image Matching

After generating the human body model and reconstructing the swimming image, the following procedure was to match the model to the swimming images to track the participant's movement. All body segments in the model are transformed to align with the human body in the swimming images. The outcome of the image matching procedure is the participant's pose estimation, i.e., the rotation angle of each body segment.

In developing the image matching algorithm, proper features must be selected. The features in the image matching are objects that can be used to establish correspondence between two images [94], i.e., the human body model and the swimming images. Furthermore, the features must be easily detectable in both the model and the swimming images [57]. In general, the feature applied in the present matching algorithm is the shape of the human body in the model and swimming images. The shape of the human body was selected as the feature in this study because it is independent of changes in illumination [57].

The features detected in the model were then mapped to the swimming images by maximizing the similarity measure. The similarity measure used in this study was the intensity value between the mapped model and the swimming images. Thus, the intensity value of each pixel of the swimming images and the transformed model was investigated. If they had the same intensity value, then the similarity increased. This similarity measure was assessed only for the area below the water surface because the silhouette was only in this area.

The body segments were assumed to be rigid, with no change in shape occurring. Then all the body segments of the model were transformed using both translational and rotational parameters. The algorithm of image matching here was adapted from the basic transformation equation developed in the running motion (Equation 1 – 5) because of different number of segments. Objection function in Equation 7 was then minimized by an optimization method to obtain maximum pixel similarity between the transformed model and the swimming data. In this work, the optimization was conducted in two steps, i.e., optimization to obtain optimum segment angle of lower limbs and upper limbs.

4.2.4 Identification of Right and Left Limb

The result of the image matching algorithm was the rotation angle of all segments with right or left side unknown. Therefore, an additional algorithm was required to identify the right and left parts of the body. In identifying right and left limbs, the least distance approach was attempted. The least distance approach determined the right of the left limb based on the angle and angular velocity difference between two consecutive frames. The reason for this approach is that the body segments should move continuously in the front-crawl stroke. Hence, it is unlikely that the upper limbs rotate too fast or change direction suddenly.

4.3 Experiment

In the present work, an experiment was conducted to obtain the motion of front-crawl swimming. The participant in this experiment was a 23-year-old male swimmer who was active in the university's swimming club, with a height of 170.5 cm and a weight of 56.5 kg. The swimming speed in this experiment was 1.13 m/s. An underwater camera Nikon Coolpix AW110 with a resolution of 1280 x 760 pixels and a rate of 60 frames per second was located 4.5 m from the participant's right side and 0.75 m below the water surface. No special lighting equipment is required in the image acquisition. The camera should be able to capture a minimum of two strokes of swimming in the sagittal plane. Figure 4.2 shows the swimming images recorded by the camera. Since the arm movement defines the front-crawl stroke, one swimming stroke cycle was defined by observing the swimming images. The pose of the participant silhouette at t = 0.00 and t = 1.00 should be identical to the indicator of one swimming cycle. After recording the swimming motion, the next procedure was image segmentation, human body model generation, image matching, and identification of right and left limb. A detailed description of each step will be presented in the following section.

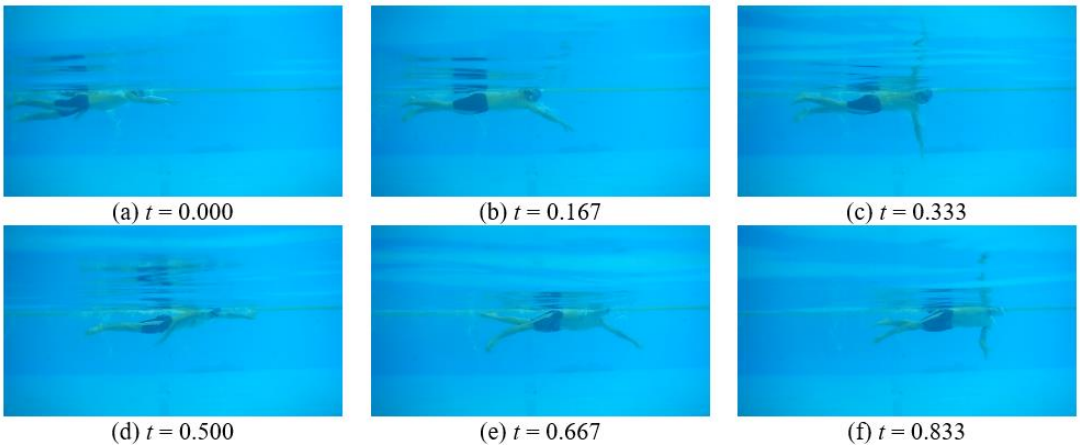

Figure 4.2 RGB swimming images. Each frame was described in non-dimensional time normalized by the cycle time.

4.4 Result and Discussion

This section discusses the result of the developed markerless optical motion capture. The angles of the body segments and the body geometry were then used for dynamics analysis by Swimming Human Simulation Model (SWUM) to obtain the kinetic parameters of

swimming. SWUM is software for dynamic analysis of swimming movements developed by Nakashima *et al.* [61].

4.4.1 Segment Angles of Front Crawl Stroke

The participant's body was modeled to obtain the segment angles of front crawl stroke. There were 15 body segments, which were numbered $i = 1$ to 15 in the present model, i.e., head, trunk, hip, right and left thigh, right and left shank, right and left foot, right and left upper arm, right and left forearm, and right and left hand, as presented in Figure 4.3. The * mark indicates the positions of all joints in the present model in Figure 4.3.

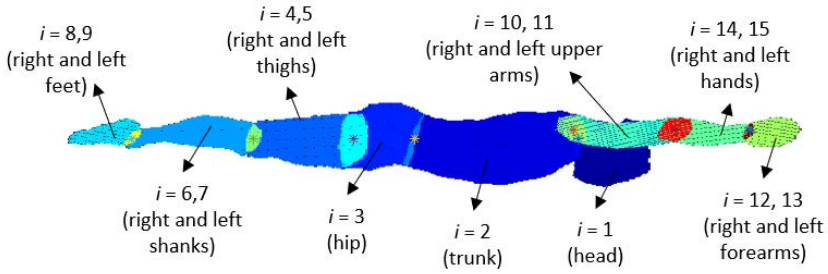

Figure 4.3 The generated model to assist the image matching process. The * marks indicate joints between two segments.

The recoded swimming images shown in Figure 4.2 was then segmented to obtain silhouette images by adaptive background Gaussian Mixture Model (GMM) described in the Section 4.2.2. The silhouette images as the results of image segmentation are presented in Figure 4.4.

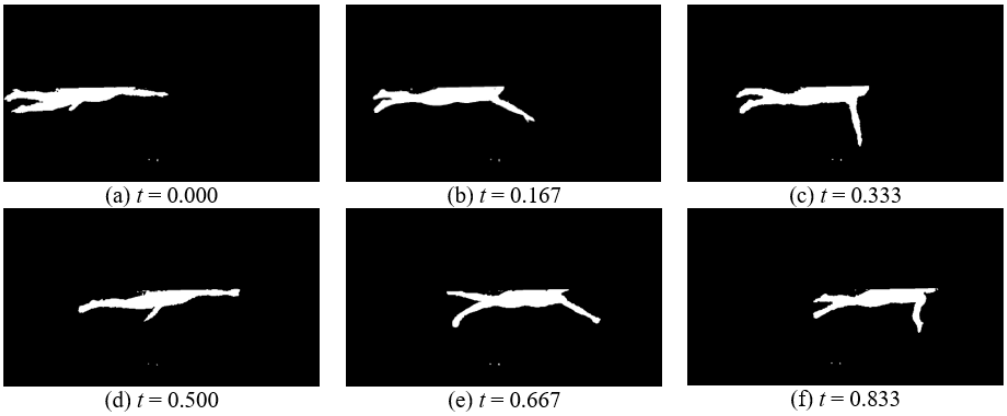

Figure 4.4 Silhouettes of the participant resulted from the image segmentation process. Each frame is in non-dimensional time.

Since the participant's body was modelled as 15 segments, then the transformation parameters involved in the image matching were $T = [t_u, t_v, \theta^1, \dots, \theta^{15}]^T$. The minimization of the objective function was evaluated by an optimization procedure. Particle swarm optimization [95] was conducted to obtain the transformation parameter for segment i = 1 to 9 with the bound from -30 degrees to 30 degrees, excluding trunk and hip. Since the trunk and hip motion in the front-crawl stroke are limited, the lower and upper bound for both segments were taken as -15 degrees and 15 degrees, respectively.

Genetic algorithm optimization [96] was used to obtain the upper limb's rotation angle, i.e., segments i = 10 to 15, by minimizing Equation 12. To decrease the degree of freedom in searching the optimum rotation angle of the upper limbs, the optimization by the genetic algorithm was bounded and constrained. The upper limb's motion was constrained by each upper limb's speed and the upper limb's rotation angle relative to their proximal limb. Image matching results were then inputted to identify right and left limb.

The accuracy of the image matching was measured by comparing the rotation angle obtained from the developed algorithm to the reference of the rotation angle. As the reference for evaluating the image matching algorithm, the predefined human body model was manually aligned to the swimming images' silhouettes. In this procedure, alignment was conducted manually with the help of an especially developed graphical user interface (GUI). For reproducibility, another operator tested the developed GUI. Firstly, all segments were translated and rotated so that the trunk in the model was aligned perfectly with the silhouettes. Then, the transformation was continued to the other segments so that all segments were matched perfectly with the silhouettes of the participant in the swimming images. An example of the rotation angle obtained from manual matching and Equation 1 – 5 is presented in Figure 4.5. As can be seen in Figure 4.5, the waveform of the rotation angle looks jagged, although a camera with 60 frames per second was used in the experiment. This jagged waveform means that not all the images were analyzed in the present study. Furthermore, one-third of the analyzed images were taken alternately to reduce the computational time.

Several body segments are above the water surface in the manual matching process, especially the head, feet, upper arms, forearms, and hands. The rotation angle of these segments was predicted by smoothing spline curve fitting [97]. The accuracy of the predicted rotation angle of segments above the water surface is not important because there is no interaction force

between the body and the water. Therefore, it has no effect on the kinematic and kinetic parameters of front-crawl swimming.

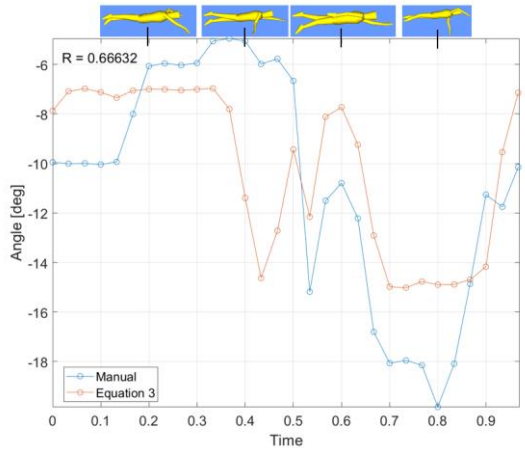

(a)

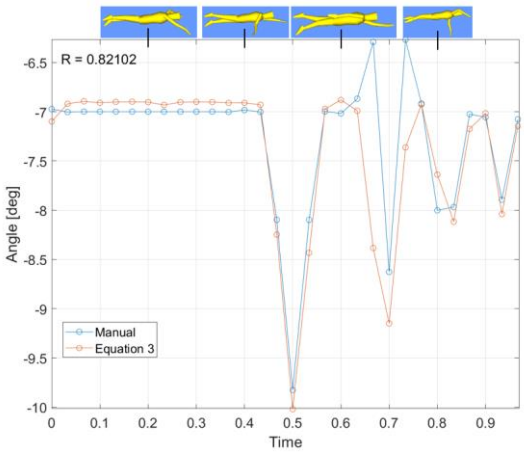

(b)

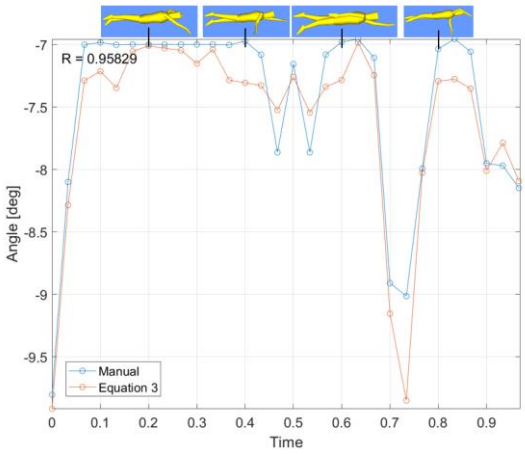

(c)

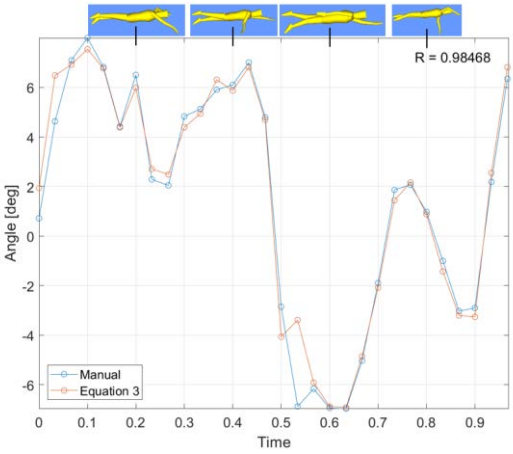

(d)

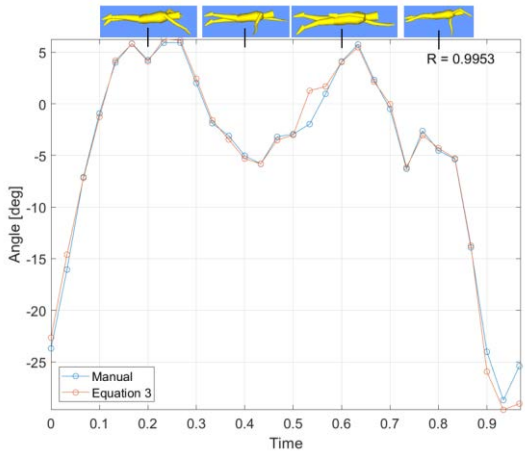

(e)

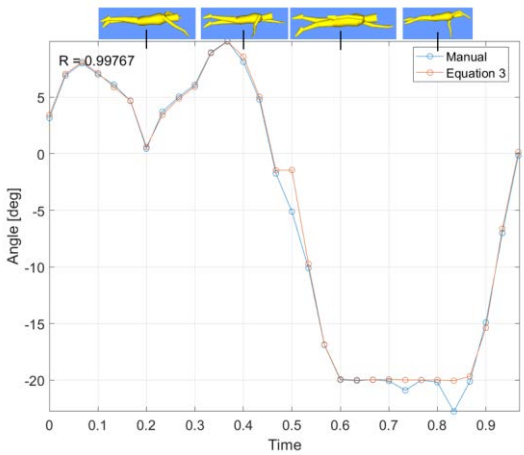

(f)

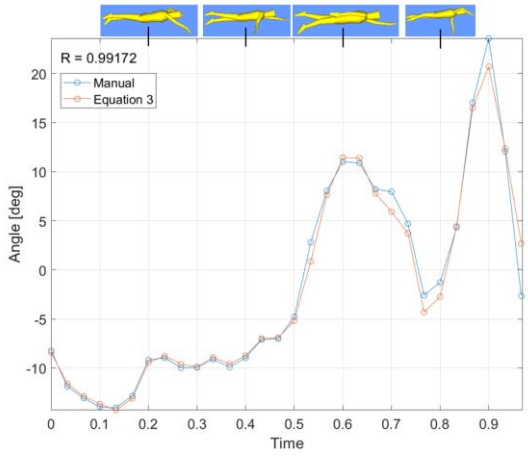
R = 0.99172
Manual
Equation 3
Angle [deg]
Time

(g)

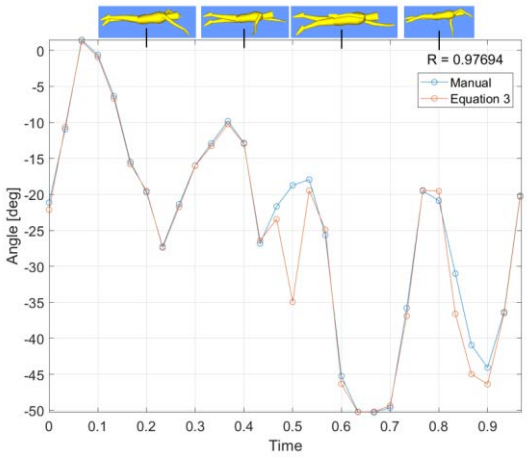
R = 0.97694
Manual
Equation 3
Angle [deg]
Time

(h)

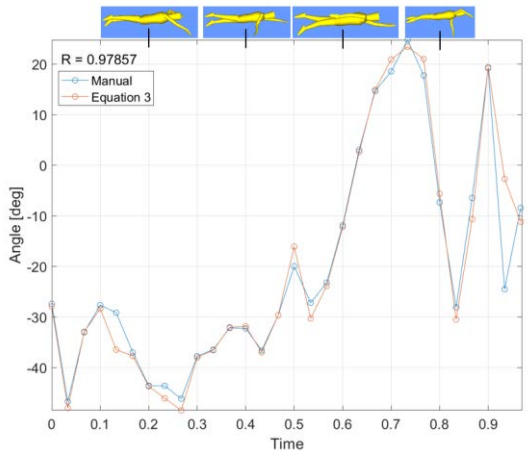
R = 0.97857
Manual
Equation 3
Angle [deg]
Time

(i)

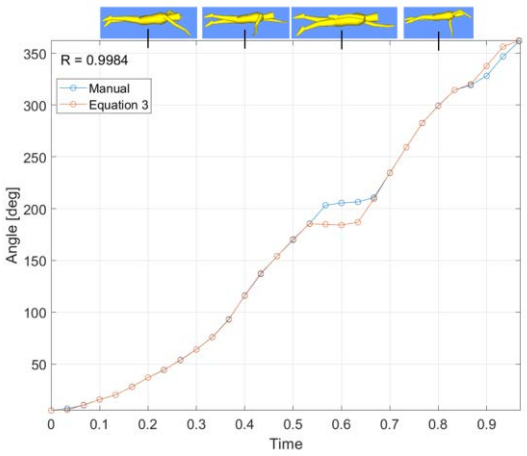
R = 0.9984
Manual
Equation 3
Angle [deg]
Time

(j)

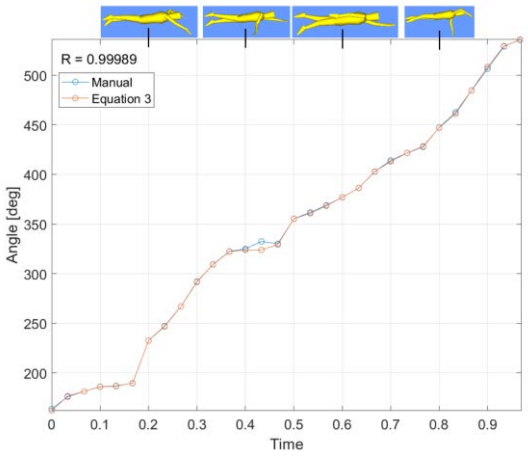
R = 0.99989
Manual
Equation 3
Angle [deg]
Time

(k)

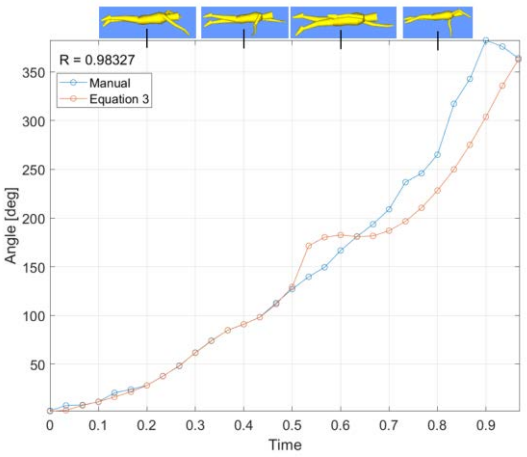
R = 0.98327
Manual
Equation 3
Angle [deg]
Time

(l)

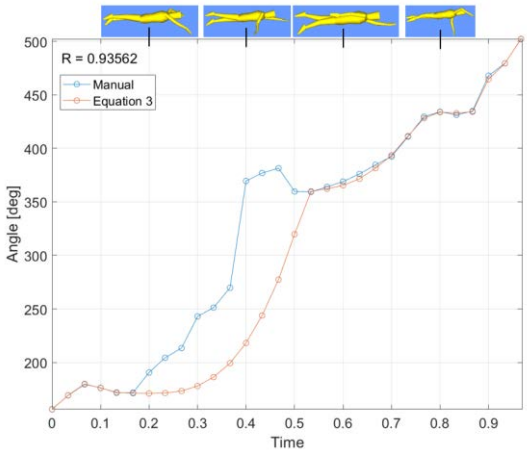

(m)

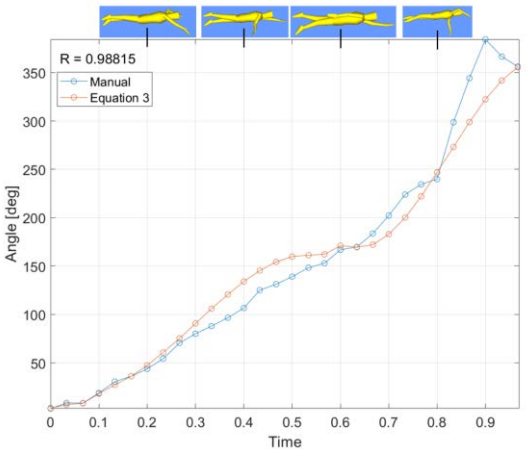

(n)

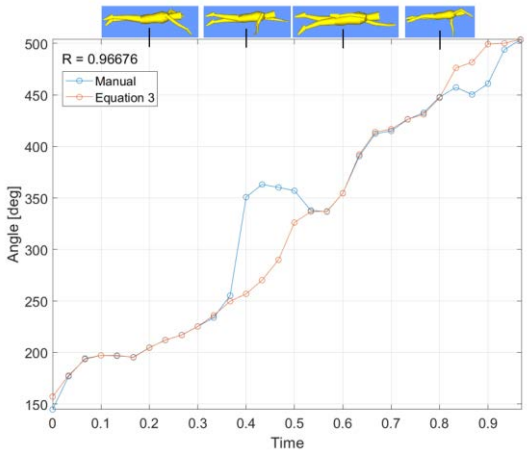

(o)

Figure 4.5 The rotation angle obtained from the developed system for body segments: (a) head, (b) trunk, (c) hip, (d) right thigh, (e) left thigh, (f) right shank, (g) left shank, (h) right foot, (i) left foot, (j) right upper arm, (k) left upper arm, (l) right forearm, (m) left forearm, (n) right hand, (o) left hand.

In comparing the rotation angle obtained from the developed algorithm to the reference of the rotation angle, an intraclass correlation coefficient, *ICC*, and root mean squared error, *RMSE*, were calculated. The intraclass correlation coefficient measures the reliability of the developed system based on the analysis variance and the estimation of variance between the rotation angle obtained from the image matching algorithm and the references [98]. The calculated *ICC* and *RMSE* are summarized in Table 4.1 for all body segments.

Table 4.1 The value of ICC and RMSE for all body segments. The RMSE in parentheses indicates an error of the body segment excluding the recovery phase.

i	**Body Segment**	**Intraclass Correlation Coefficient, *ICC***	**Root Mean Squared Error, *RMSE* (°)**
1	Head	0.629	3.49
2	Trunk	0.812	0.46
3	Hip	0.941	0.26
4	Right thigh	0.984	0.83
5	Left thigh	0.994	1.06
6	Right shank	0.997	0.88
7	Left shank	0.991	1.33
8	Right foot	0.974	3.30
9	Left foot	0.978	4.55
10	Right upper arm	0.998	6.74
11	Left upper arm	0.999	1.70
12	Right forearm	0.969	28.30 (1.85)
13	Left forearm	0.914	48.17 (2.13)
14	Right hand	0.983	19.95 (14.21)
15	Left hand	0.966	29.65 (14.28)

The *ICC* values presented in Table 4.1 indicate that the developed algorithm in the present work produced acceptable results with the markerless optical motion capture system for daily training application. The developed system could also obtain the rotation angle of left body segments with a high correlation coefficient, even though the camera was placed on the participant's right side. The rotation angles of the left body segments were obtained from the image matching between the transformed model and the participant's silhouette. Since the silhouette of the left segments is visible in the images, the image matching algorithm could still be evaluated. The *ICC* was mostly larger than 0.95, except for the head and trunk. The head segment had a lower correlation coefficient because this segment was mainly outside the water. Hence, the head segment was not captured by the underwater camera. In addition, the trunk also had a lower correlation coefficient due to its insignificant movement in swimming. This

is because, when the motion of the segment was very small, the fluctuation of the angle did not become a meaningful one but merely a measurement error.

Based on the *RMSE* value presented in Table 4.1, the rotation angle error obtained from the present system compared to those from manual matching was relatively minor. Therefore, it could be seen that the image matching algorithm was executed with good performance. In addition, the *RMSE* value in parentheses indicates an error when the recovery phase was excluded in the calculation. The forearm and hand are above the water surface in the recovery phase, so the camera cannot capture them. Hence, their rotation angles were predicted by a curve fitting algorithm that resulted in a relatively large *RMSE*. However, this error did not affect the dynamics analysis because no propulsive force is produced in the recovery phase. In addition, the *RMSE* of the hand was comparatively large, although the rotation angle obtained from the curve fitting algorithm was excluded. The errors were caused by the blurred image, especially in the hand area, so the silhouette of the participant's hand was not segmented perfectly.

4.4.2 Dynamics Parameters by SWUM

The dynamics analysis by SWUM to obtain dynamics parameters was conducted based on the methodology described in the Section 3.2.5. For dynamic analysis using SWUM, the linear velocity at the center of gravity (CoG) of the participant was required as input. The linear velocity at the CoG was obtained from the world coordinates of the CoG after camera calibration with the Direct Linear Transformation method [89], as explained in Chapter 3. By performing 2D reconstruction, the CoG trajectory in the world coordinate could be obtained by utilizing the CoG position in the image coordinate system and DLT parameters.

The CoG trajectory in the world coordinate system obtained from 2D reconstruction was then derived once against time to get the linear velocity of CoG. The linear velocity of CoG in the propulsive directions is shown in Figure 4.6. Apart from these data, body geometry and joint motion for each segment of the subject's body were also needed. The height and weight of the participants in this study were 1.705 m and 56.5 kg. In SWUM, all body segments were modeled as truncated elliptic cones and had a specific gravity (density relative to water) of 1.042, except for 0.7 for the chest [61].

The results of dynamics analysis by SWUM are presented in Figure 4.7 to Figure 4.10, respectively. Figure 4.7 shows the simulation result of the front crawl stroke. The red line represents the vector of fluid forces acting on that segment. Figure 4.8 to Figure 4.10 present the fluid forces in the propulsive direction acting on the whole body, right upper limb, and right lower limb, respectively. Note that the abscissa denotes the time that is normalized with the cycle time or non-dimensional time. The ordinate indicates the fluid force in the propulsive direction, and it is normalized by the participant's body weight, height, and cycle time.

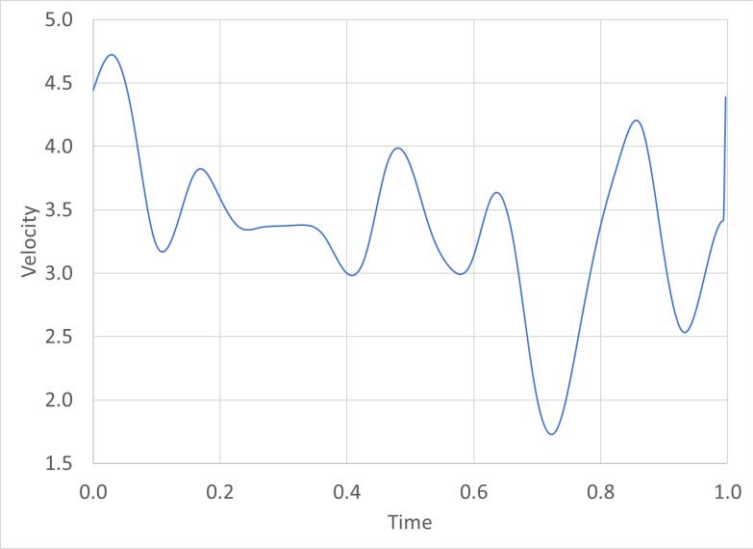

Figure 4.6 The velocity of CoG in the propulsive direction

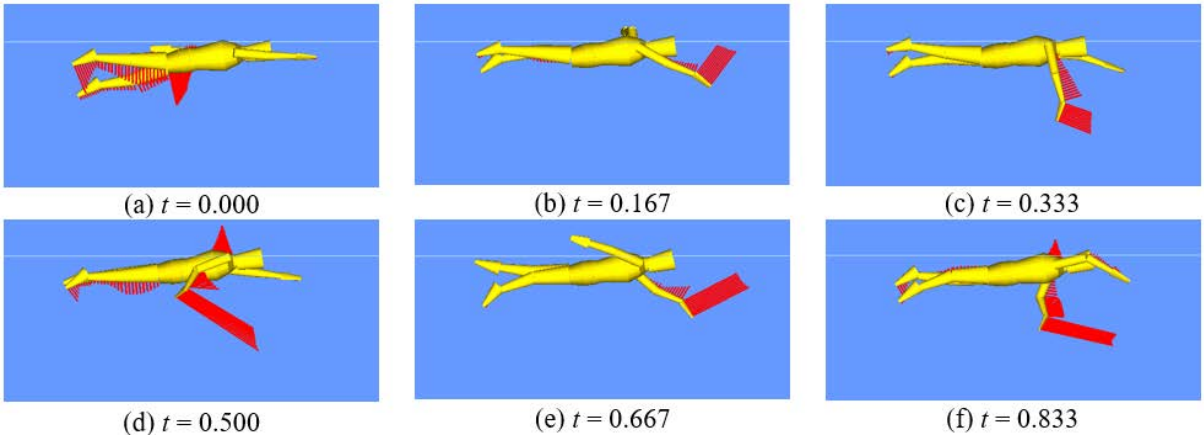

Figure 4.7 Result of the dynamics analysis by SWUM. The red line indicates the vector of fluid forces. Each frame is in non-dimensional time.

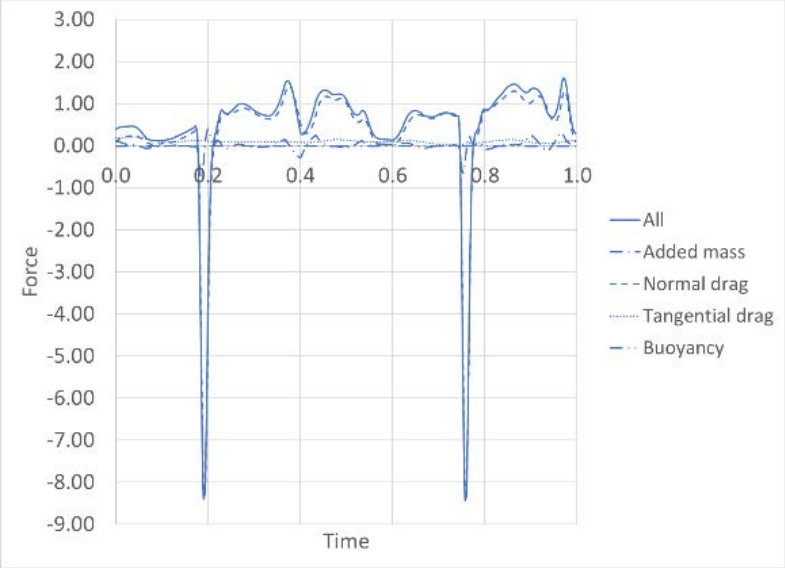

Figure 4.8 The fluid forces on the whole body in the propulsive direction. The force and time are in a non-dimensional unit.

In Figure 4.8, there was a large negative thrust force exerted on the participant's body in the short time at $t = 0.2$ and $t = 0.75$. The negative force that occurred at $t = 0.2$ was produced by the movement of the left upper limbs. In addition, the negative force at $t = 0.75$ was triggered by the right upper limb movement (see Figure 4.9). These negative forces were caused by the shortcoming of the present system that could not include the rolling movement. Since there is no rolling movement, the upper limbs of the participant interacted with water in the recovery phase. However, there should be a rolling movement in the front crawl stroke since it is the characteristic of this stroke.

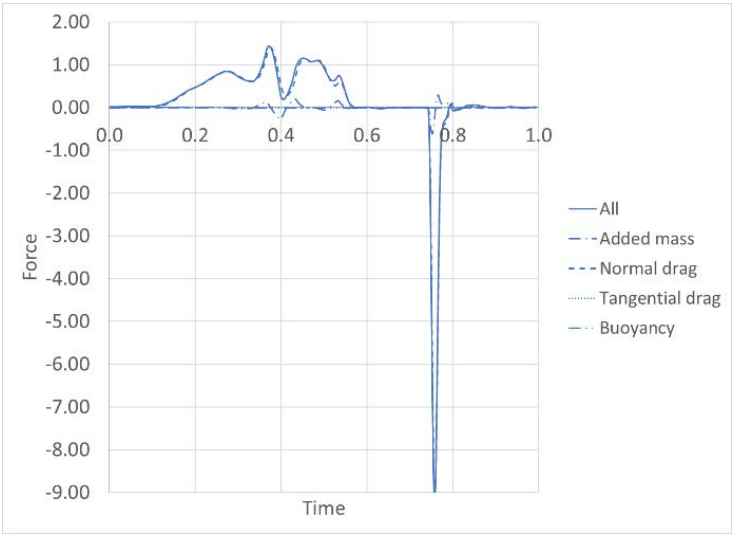

Figure 4.9 The fluid forces on the right upper limbs in the propulsive direction. The force and time are in a non-dimensional unit.

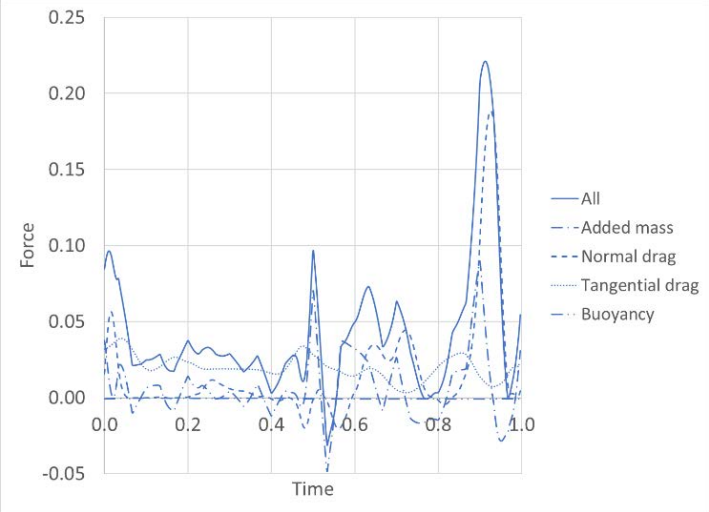

Figure 4.10 The fluid forces on the right lower limbs in the propulsive direction. The force and time are in a non-dimensional unit.

As could be seen in Figure 4.8 and Figure 4.9, the propulsive force at $t = 0.1$ to $t = 0.6$ was generated from the right upper limbs. On the other hand, the propulsive force at another time was contributed from the left upper limbs. Furthermore, Figure 4.10implies that the fluid force from the lower limb had an insignificant influence on the propulsive movement of swimming. The increasing propulsive force on the whole body shown in Figure 4.7 at $t = 0.1$, $t = 0.4$, $t = 0.7$, and $t = 0.95$ initiated the increasing velocity in the propulsive direction at the corresponding time.

The interaction between the water and the participant's body segments resulted from the analysis of the dynamics by SWUM is important for the athlete and the coach. By investigating the propulsive forces, they can evaluate the athlete's movement and learn a strategy to increase the athlete's performance. Hence, the system developed in the present work is suitable for coaches and athletes for daily training use due to its simplicity in data acquisition of swimming movement. The present study's total computational time to analyze the front-crawl stroke was around one hour. The stroke investigated in the present study was the front-crawl stroke, but the current system can also be used to evaluate the other asymmetrical swimming strokes. In addition, the developed system is helpful in analyzing swimming motion of any level of swimmer, including top-level swimmers. One of the limitations of the present study is that the system could be improved to analyze in real-time, which could be the subject of future investigation. Moreover, the system should be validated for full-strength swimming, which may generate more bubbles.

4.5 Conclusion

The development of a markerless optical motion capture system for the front-crawl swimming stroke was presented. The system uses an underwater camera to acquire the motion of swimming. No configuration, such as lighting or marker attachment, is required. The system consists of image segmentation, model generation, image matching, and identification of right and left limb procedures. To validate the rotation angle of all body segments, the intraclass correlation coefficient (ICC) between the result and reference was investigated. It showed acceptable reliability of the system. The joint motion and body geometry of the participant was then used to obtain dynamics parameters of swimming using the SWUM software. From this result, coaches can evaluate the athlete's movement and learn a strategy to increase the athlete's performance. Hence, the developed system is suitable for coaches and athletes for daily training use due to its simplicity in data acquisition of swimming motion.

Chapter 5
Conclusion

5.1 Conclusion

In this thesis, the affordable markerless optical motion capture system has been successfully developed. The system consists of four main processes, i.e., camera calibration, model generation, image segmentation, and image registration, as summarised in Figure 5.1. The camera calibration is conducted to obtain the camera parameter that could be used to establish the relationship between image coordinate system and world coordinate system. Then, the calibrated camera is used to record the targeted movement. One of the recorded frames is used to generate the human body model by manual segmentation to enhance the accuracy. The model is used as the priori information in the tracking process. On the other hand, all the recorded frames are segmented by Otsu or background subtraction method to achieve the silhouette of the subject. The next procedure is image registration where the model is rotated until the pose resembles the silhouette on the recorded frame. Optimization is used in the image matching process to maximize the similarity between the pose rotated model and the silhouettes. The output of the image registration is the rotation angle of each segment of human body. The rotation angle could be further used in the dynamics analysis.

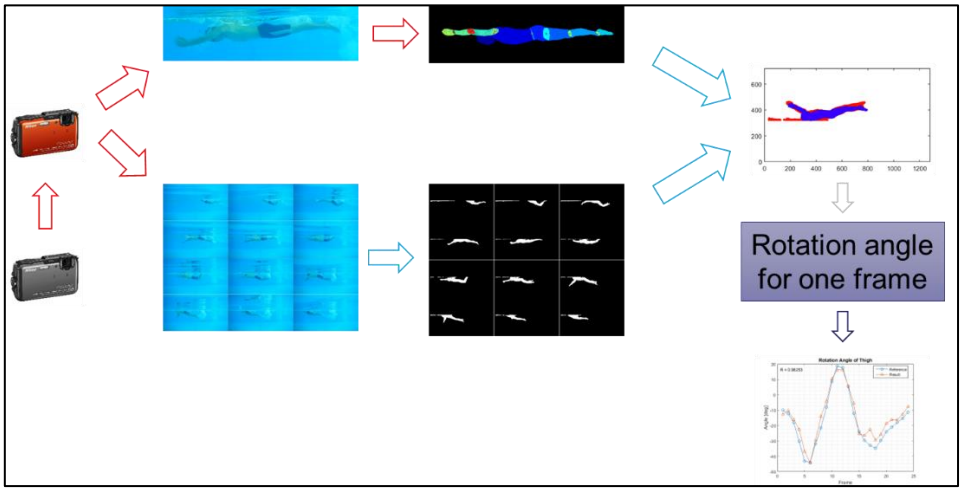

Figure 5.1 The procedure of using the developed markerless optical motion capture system

The system is tried out in three main applications, i.e., bilateral symmetrical swimming stroke, asymmetrical swimming stroke, and running motion to investigate the accuracy and the

reliability of the system. In the application bilateral symmetrical swimming stroke, the butterfly stroke is employed to investigate the system. As a result, the rotation angle's correlation coefficients between the references and result of the matching process were around 0.95 for trunk, thigh, shank, upper arm, forearm, hand and 0.78 for head, hip, and foot. On the other hand, the front crawl swimming stroke is conducted to explore the performance of the system. The intraclass correlation coefficient between the results of the developed system and references were evaluated. In general, all body segments, except head and trunk, had a correlation coefficient higher than 0.95. The last movement that is applied to the system is the running motion. The correlation coefficient between the rotation angle from image registration and the actual rotation angle was then evaluated. It was found that the lowest correlation coefficient was 0.977 for the left foot. It implies that the accuracy of the developed system in the present work is acceptable.

The main advantage of this system is that it is relatively simple and cheap. Moreover, the system also provides semi-automatic tracking instead of manual tracking to reduce the processing time of swimming motion analysis. It is expected that the proposed system could be used by athletes and coaches for daily training in a shorter time than the use of manual tracking to obtain an athlete's body motion. By using this system, the coaches can evaluate the athlete's movement and learn a strategy to increase the athlete's performance.

5.2 Suggestion and future work

Based on the available data, analysis, and the conclusion. Several suggestions may be made for better improvement in the future related to this report results. The suggestions are listed below:

1. Vary the segment length to obtain better accuracy for more 3D motions.
2. The automatic procedure could be further automized by incorporate low level Artificial Intelligence (AI)
3. The algorithm of image registration could be further improved to cut the computational cost.

References

[1] D. M. Clancy, “Chapter | 38 | - Movement analysis: Science meets practice,” in *A Comprehensive Guide to Sports Physiology and Injury Management*, S. Porter and J. Wilson, Eds. St. Louis (MO): Elsevier, 2020, pp. 465–479. doi: 10.1016/B978-0-7020-7489-9.00038-7.

[2] R. C. Z. Cohen, P. W. Cleary, B. R. Mason, and D. L. Pease, “The Role of the Hand during Freestyle Swimming,” *Journal of Biomechanical Engineering*, vol. 137, no. 11, pp. 1–10, 2015, doi: 10.1115/1.4031586.

[3] W. Ben Kibler, “The role of the scapula in athletic shoulder function,” *American Journal of Sports Medicine*, vol. 26, no. 2, pp. 325–337, 1998, doi: 10.1177/03635465980260022801.

[4] J. N. Johnson, J. Gauvin, and M. Fredericson, “Swimming biomechanics and injury prevention: New stroke techniques and medical considerations,” *Physician and Sportsmedicine*, vol. 31, no. 1, pp. 41–46, 2003, doi: 10.3810/psm.2003.01.165.

[5] E. Hoummadi, M. Safaei, and S. R. Anton, “Design, analysis, and fabrication of a piezoelectric force plate,” *Health Monitoring of Structural and Biological Systems 2017*, vol. 10170, p. 101700W, 2017, doi: 10.1117/12.2260381.

[6] F. Ferryanto, M. M. Akbar, S. Wicaksono, and A. I. Mahyuddin, “Design, Manufacture, and Testing of a Low-Cost Force Platform with 3-Axis Load Cell,” *IOP Conference Series: Materials Science and Engineering*, vol. 1109, no. 1, p. 012021, 2021, doi: 10.1088/1757-899x/1109/1/012021.

[7] C. J. De Luca, “The Use of Surface Electromyography in Biomechanics,” *Journal of Applied Biomechanics*, vol. 13, no. 2, pp. 135–163, May 1997, doi: 10.1123/JAB.13.2.135.

[8] N. Massó, F. Rey, D. Romero, G. Gual, L. Costa, and A. Germán, “Surface electromyography applications in the sport,” *Apunts: Medicina de l’esport*, vol. 45, no. 166, pp. 121-131–131, 2010.

[9] C. L. Vaughan, B. L. Davis, and J. C. O'Connor, *Dynamics of Human Gait*, 2nd ed. Kiboho, 1999.

[10] E. Muybridge, "The science of the horse's motions," *Sci Am*, vol. 39, p. 241, 1878.

[11] LastMinuteEngineers.com, "Interface MPU6050 Accelerometer and Gyroscope Sensor with Arduino," 2022. https://lastminuteengineers.com/mpu6050-accel-gyro-arduino-tutorial/ (accessed Sep. 19, 2022).

[12] D. A. Winter, *Biomechanics and Motor Control of Human Movement*, 4th ed. John Wiley & Sons, Inc., 2009. doi: 10.1002/9780470549148.

[13] Qualysis, "Motion Capture System," 2022. https://www.qualisys.com/ (accessed Sep. 19, 2022).

[14] Vicon Motion Systems Ltd, "VICON," 2022. https://www.vicon.com/ (accessed Sep. 19, 2022).

[15] Inc. D. O. NaturalPoint, "OptiTrack - Motion Capture Systems," 2022. https://optitrack.com/ (accessed Sep. 19, 2022).

[16] Y. I. Abdel-Aziz and H. M. Karara, "Direct Linear Transformation from Comparator Coordinates into Object Space Coordinates in Close-Range Photogrammetry," *Photogrammetric Engineering & Remote Sensing*, vol. 81, no. 2, pp. 103–107, Feb. 2015, doi: 10.14358/PERS.81.2.103.

[17] H. Hatze, "High-precision three-dimensional photogrammetric calibration and object space reconstruction using a modified DLT-approach," *Journal of Biomechanics*, vol. 21, no. 7, pp. 533–538, Jan. 1988, doi: 10.1016/0021-9290(88)90216-3.

[18] R. Y. Tsai, "A Versatile Camera Calibration Technique for High-Accuracy 3D Machine Vision Metrology Using Off-the-Shelf TV Cameras and Lenses," *IEEE Journal on Robotics and Automation*, vol. 3, no. 4, pp. 323–344, 1987, doi: 10.1109/JRA.1987.1087109.

[19] O. Faugeras and G. Toscani, "The Calibration Problem for Stereo," in *Proceeding of the IEEE Conference on Computer Vision and Pattern Recognition*, 1986, pp. 15–20.

[20] Z. Zhang, "A Flexible New Technique for Camera Calibration (Technical Report)," *IEEE Transactions on Pattern Analysis and Machine Intelligence*, vol. 22, no. 11, pp. 1330–1334, 2002, doi: 10.1109/34.888718.

[21] J. Garza-Ulloa, *Kinematic and kinetic measurements of human body*. Elsevier Inc., 2018. doi: 10.1016/b978-0-12-812594-6.00003-2.

[22] Z. Zhang, "A flexible new technique for camera calibration," *IEEE Transactions on Pattern Analysis and Machine Intelligence*, vol. 22, no. 11, pp. 1330–1334, 2000, doi: 10.1109/34.888718.

[23] D. Tabakin and C. L. Vaughan, "A comparison of 3D gait models based on the Helen Hayes marker set," *Proceedings of the sixth international symposium on the 3D analysis of human movement*, pp. 98–101, 2000.

[24] P. Castagno, J. Richards, F. Miller, and N. Lennon, "Comparison of 3-dimensional lower extremity kinematics during walking gait using two different marker sets," *Gait & Posture*, vol. 2, no. 3, p. 87, 1995.

[25] S. Mihradi, Ferryanto, T. Dirgantara, and A. I. Mahyuddin, "Development of an optical motion-capture system for 3D gait analysis," in *Proceedings - International Conference on Instrumentation, Communication, Information Technology and Biomedical Engineering 2011, ICICI-BME 2011*, Nov. 2011, pp. 391–394. doi: 10.1109/ICICI-BME.2011.6108633.

[26] S. Corazza, L. M??ndermann, A. M. Chaudhari, T. Demattio, C. Cobelli, and T. P. Andriacchi, "A markerless motion capture system to study musculoskeletal biomechanics: Visual hull and simulated annealing approach," *Annals of Biomedical Engineering*, vol. 34, no. 6, pp. 1019–1029, 2006, doi: 10.1007/s10439-006-9122-8.

[27] Z. Cao, G. Hidalgo, T. Simon, S. E. Wei, and Y. Sheikh, "OpenPose: Realtime Multi-Person 2D Pose Estimation Using Part Affinity Fields," *IEEE Transactions on Pattern Analysis and Machine Intelligence*, vol. 43, no. 1, pp. 172–186, 2021, doi: 10.1109/TPAMI.2019.2929257.

[28] K. Sun, B. Xiao, D. Liu, and J. Wang, "Deep High-Resolution Representation Learning for Human Pose Estimation," presented at the Proceedings of the IEEE/CVF Conference on Computer Vision and Pattern Recognition, 2019, pp. 5693–5703. Accessed: Jan. 30,

2023. [Online]. Available: https://openaccess.thecvf.com/content_CVPR_2019/html/Sun_Deep_High-Resolution_Representation_Learning_for_Human_Pose_Estimation_CVPR_2019_paper.html

[29] L. Pishchulin *et al.*, "DeepCut: Joint Subset Partition and Labeling for Multi Person Pose Estimation," presented at the Proceedings of the IEEE Conference on Computer Vision and Pattern Recognition, 2016, pp. 4929–4937. Accessed: Jan. 30, 2023. [Online]. Available: https://www.cv-foundation.org/openaccess/content_cvpr_2016/html/Pishchulin_DeepCut_Joint_Subset_CVPR_2016_paper.html

[30] H.-S. Fang *et al.*, "AlphaPose: Whole-Body Regional Multi-Person Pose Estimation and Tracking in Real-Time," *IEEE Transactions on Pattern Analysis and Machine Intelligence*, pp. 1–17, 2022, doi: 10.1109/TPAMI.2022.3222784.

[31] G. Boesch, "The Complete Guide to OpenPose in 2023," *viso.ai*, Jan. 01, 2023. https://viso.ai/deep-learning/openpose/ (accessed Jan. 30, 2023).

[32] E. Insafutdinov, L. Pishchulin, B. Andres, M. Andriluka, and B. Schiele, "DeeperCut: A Deeper, Stronger, and Faster Multi-person Pose Estimation Model," in *Computer Vision – ECCV 2016*, Cham, 2016, pp. 34–50. doi: 10.1007/978-3-319-46466-4_3.

[33] M. Nakai, Y. Tsunoda, H. Hayashi, and H. Murakoshi, "Prediction of Basketball Free Throw Shooting by OpenPose," in *New Frontiers in Artificial Intelligence*, Cham, 2019, pp. 435–446. doi: 10.1007/978-3-030-31605-1_31.

[34] Y.-C. Li, C.-T. Chang, C.-C. Cheng, and Y.-L. Huang, "Baseball Swing Pose Estimation Using OpenPose," in *2021 IEEE International Conference on Robotics, Automation and Artificial Intelligence (RAAI)*, Apr. 2021, pp. 6–9. doi: 10.1109/RAAI52226.2021.9507807.

[35] M. Ben Gamra and M. A. Akhloufi, "A review of deep learning techniques for 2D and 3D human pose estimation," *Image and Vision Computing*, vol. 114, p. 104282, Oct. 2021, doi: 10.1016/j.imavis.2021.104282.

[36] T. B. Moeslund, A. Hilton, and V. Kr??ger, "A survey of advances in vision-based human motion capture and analysis," *Computer Vision and Image Understanding*, vol. 104, no. 2-3 SPEC. ISS., pp. 90–126, 2006, doi: 10.1016/j.cviu.2006.08.002.

[37] L. Mündermann, S. Corazza, and T. P. Andriacchi, "The evolution of methods for the capture of human movement leading to markerless motion capture for biomechanical applications," *Journal of NeuroEngineering and Rehabilitation*, vol. 3, pp. 1–11, 2006, doi: 10.1186/1743-0003-3-6.

[38] A. Fernández-Baena, A. Susín, and X. Lligadas, "Biomechanical validation of upper-body and lower-body joint movements of kinect motion capture data for rehabilitation treatments," *Proceedings of the 2012 4th International Conference on Intelligent Networking and Collaborative Systems, INCoS 2012*, pp. 656–661, 2012, doi: 10.1109/INCOS.2012.66.

[39] J.-H. Yoo and M. S. Nixon, "Automated Markerless Analysis of Human Gait Motion for Recognition and Classification," *ETRI Journal*, vol. 33, no. 2, pp. 259–266, 2011, doi: 10.4218/etrij.11.1510.0068.

[40] I. Bouchrika and M. S. Nixon, "Model-Based Feature Extraction for Gait Analysis and Recognition," *Computer vision/computer graphics collaboration technique*, pp. 150–160, 2007.

[41] M. Goffredo, J. N. Carter, and M. S. Nixon, "2D markerless gait analysis," in *IFMBE Proceedings*, 2008, vol. 22, no. 1, pp. 67–71. doi: 10.1007/978-3-540-89208-3_18.

[42] A. Leu, D. Ristic-Durrant, and A. Graser, "A robust markerless vision-based human gait analysis system," in *SACI 2011 - 6th IEEE International Symposium on Applied Computational Intelligence and Informatics, Proceedings*, May 2011, pp. 415–420. doi: 10.1109/SACI.2011.5873039.

[43] S. Corazza, L. Mündermann, E. Gambaretto, G. Ferrigno, and T. P. Andriacchi, "Markerless motion capture through visual hull, articulated ICP and subject specific model generation," *International Journal of Computer Vision*, vol. 87, no. 1–2, pp. 156–169, 2010, doi: 10.1007/s11263-009-0284-3.

[44] A. L. Sheets, G. D. Abrams, S. Corazza, M. R. Safran, and T. P. Andriacchi, "Kinematics differences between the flat, kick, and slice serves measured using a markerless motion

capture method," *Annals of Biomedical Engineering*, vol. 39, no. 12, pp. 3011–3020, Dec. 2011, doi: 10.1007/S10439-011-0418-Y/FIGURES/8.

[45] G. D. Abrams, A. H. S. Harris, T. P. Andriacchi, and M. R. Safran, "Biomechanical analysis of three tennis serve types using a markerless system," *British Journal of Sports Medicine*, vol. 48, no. 4, pp. 339–342, Feb. 2014, doi: 10.1136/BJSPORTS-2012-091371.

[46] E. Ceseracciu *et al.*, "Markerless analysis of front crawl swimming," *Journal of Biomechanics*, vol. 44, no. 12, pp. 2236–2242, 2011, doi: 10.1016/j.jbiomech.2011.06.003.

[47] J. Bray, "Markerless Based Human Motion Capture: A Survey," Brunel University, 2001. doi: 10.1080/02724634.1995.10011260.

[48] D. M. Gavrila and L. S. Davis, "Towards 3-D model-based tracking and recognition of human movement: a multi-view approach," in *Proceedings of the IEEE International Conference on Computer Vision*, 1995, pp. 253–258. doi: 10.1109/iscv.1995.477010.

[49] A. O. Bălan, L. Sigal, and M. J. Black, "A quantitative evaluation of video-based 3D person tracking," in *Proceedings - 2nd Joint IEEE International Workshop on Visual Surveillance and Performance Evaluation of Tracking and Surveillance, VS-PETS*, 2005, vol. 2005, pp. 349–356. doi: 10.1109/VSPETS.2005.1570935.

[50] I. A. Kakadiaris and D. Metaxas, "Model-based estimation of 3D human motion with occlusion based on active multi-viewpoint selection," *Proceedings of the IEEE Computer Society Conference on Computer Vision and Pattern Recognition*, pp. 81–87, 1996, doi: 10.1109/CVPR.1996.517057.

[51] K. M. Cheung, S. Baker, and T. Kanade, "Shape-from-silhouette across time part II: Applications to human modeling and markerless motion tracking," *International Journal of Computer Vision*, vol. 63, no. 3, pp. 225–245, Apr. 2005, doi: 10.1007/s11263-005-6879-4.

[52] M. Piccardi, "Background subtraction techniques: A review," *Conference Proceedings - IEEE International Conference on Systems, Man and Cybernetics*, vol. 4, pp. 3099–3104, 2004, doi: 10.1109/ICSMC.2004.1400815.

[53] C. Stauffer and W. E. L. Grimson, "Adaptive background mixture models for real-time tracking," *Proceedings of the IEEE Computer Society Conference on Computer Vision and Pattern Recognition*, vol. 2, pp. 246–252, 1999, doi: 10.1109/cvpr.1999.784637.

[54] S. Hao, Y. Zhou, and Y. Guo, "A Brief Survey on Semantic Segmentation with Deep Learning," *Neurocomputing*, vol. 406, pp. 302–321, Sep. 2020, doi: 10.1016/J.NEUCOM.2019.11.118.

[55] H. Yu *et al.*, "Methods and datasets on semantic segmentation: A review," *Neurocomputing*, vol. 304, pp. 82–103, Aug. 2018, doi: 10.1016/J.NEUCOM.2018.03.037.

[56] S. Nobuhara, Y. Tsuda, I. Ohama, and T. Matsuyama, "Multi-viewpoint Silhouette Extraction with 3D Context-aware Error Detection, Correction, and Shadow Suppression," *IPSJ Transactions on Computer Vision and Applications*, vol. 1, pp. 242–259, 2009, doi: 10.2197/IPSJTCVA.1.242.

[57] B. Zitová and J. Flusser, "Image registration methods: A survey," *Image and Vision Computing*, vol. 21, no. 11, pp. 977–1000, 2003, doi: 10.1016/S0262-8856(03)00137-9.

[58] H. Abdi and L. J. Williams, "Principal component analysis," *Wiley Interdisciplinary Reviews: Computational Statistics*, vol. 2, no. 4, pp. 433–459, Jul. 2010, doi: 10.1002/WICS.101.

[59] J. Zhang, Y. Yao, and B. Deng, "Fast and Robust Iterative Closest Point," *IEEE Transactions on Pattern Analysis and Machine Intelligence*, vol. 44, no. 7, pp. 3450–3466, Jul. 2022, doi: 10.1109/TPAMI.2021.3054619.

[60] L. Mündermann, "Markerless human motion capture through visual hull and articulated ICP," in *... Articulated Human Motion ...*, 2006, vol. 2.

[61] M. Nakashima, K. Satou, and Y. Miura, "Development of Swimming Human Simulation Model Considering Rigid Body Dynamics and Unsteady Fluid Force for Whole Body," *Journal of Fluid Science and Technology*, vol. 2, no. 1, pp. 56–67, Feb. 2007, doi: 10.1299/jfst.2.56.

[62] "The State of Running 2019 | RunRepeat." https://runrepeat.com/state-of-running (accessed Sep. 22, 2022).

[63] W. F. Major, "The Benefits and Costs of Serious Running," *http://dx.doi.org/10.1080/04419057.2001.9674226*, vol. 43, no. 2, pp. 12–25, Jan. 2011, doi: 10.1080/04419057.2001.9674226.

[64] L. L. Craft and F. M. Perna, "The Benefits of Exercise for the Clinically Depressed," *Primary Care Companion to The Journal of Clinical Psychiatry*, vol. 6, no. 3, p. 104, Jun. 2004, doi: 10.4088/PCC.V06N0301.

[65] V. E. Wilson, B. G. Berger, and E. I. Bird, "Effects of Running and of an Exercise Class on Anxiety," *http://dx.doi.org/10.2466/pms.1981.53.2.472*, vol. 53, no. 2, pp. 472–474, Oct. 2016, doi: 10.2466/PMS.1981.53.2.472.

[66] Á. G. Lucas-Cuevas, J. I. Priego Quesada, J. Gooding, M. G. C. Lewis, A. Encarnación-Martínez, and P. Perez-Soriano, "The effect of visual focus on spatio-temporal and kinematic parameters of treadmill running," *Gait & Posture*, vol. 59, pp. 292–297, Jan. 2018, doi: 10.1016/J.GAITPOST.2017.07.039.

[67] F. J. Wouda *et al.*, "On the Validity of Different Motion Capture Technologies for the Analysis of Running," *Proceedings of the IEEE RAS and EMBS International Conference on Biomedical Robotics and Biomechatronics*, vol. 2018-August, pp. 1175–1180, Oct. 2018, doi: 10.1109/BIOROB.2018.8487210.

[68] S. Mihradi, Ferryanto, T. Dirgantara, and A. I. Mahyuddin, "Tracking of Markers for 2D and 3D Gait Analysis Using Home Video Cameras," *International Journal of E-Health and Medical Communications*, vol. 4, no. 3, pp. 36–52, Jan. 2013, doi: 10.4018/jehmc.2013070103.

[69] R. Cross, "Standing, walking, running, and jumping on a force plate," *American Journal of Physics*, vol. 67, no. 4, p. 304, Mar. 1999, doi: 10.1119/1.19253.

[70] J. H. Challis, "The Variability in Running Gait Caused by Force Plate Targeting," *Journal of Applied Biomechanics*, vol. 17, no. 1, pp. 77–83, Feb. 2001, doi: 10.1123/JAB.17.1.77.

[71] E. Bergamini, P. Picerno, H. Pillet, F. Natta, P. Thoreux, and V. Camomilla, "Estimation of temporal parameters during sprint running using a trunk-mounted inertial measurement unit," *Journal of Biomechanics*, vol. 45, no. 6, pp. 1123–1126, Apr. 2012, doi: 10.1016/J.JBIOMECH.2011.12.020.

[72] G. R. D. Bernardina, T. Monnet, H. T. Pinto, R. M. L. de Barros, P. Cerveri, and A. P. Silvatti, "Are Action Sport Cameras Accurate Enough for 3D Motion Analysis? A Comparison With a Commercial Motion Capture System," *Journal of Applied Biomechanics*, pp. 1–17, Jul. 2018, doi: 10.1123/jab.2017-0101.

[73] A. Castelli, G. Paolini, A. Cereatti, and U. Della Croce, "A 2D markerless gait analysis methodology: Validation on healthy subjects," *Computational and Mathematical Methods in Medicine*, vol. 2015, 2015, doi: 10.1155/2015/186780.

[74] F. Ferryanto and M. Nakashima, "Development of a markerless optical motion capture system for daily use of training in swimming," *Sports Engineering*, vol. 20, no. 1, pp. 63–72, Sep. 2017, doi: 10.1007/s12283-016-0218-6.

[75] M. Ota, H. Tateuchi, T. Hashiguchi, and N. Ichihashi, "Verification of validity of gait analysis systems during treadmill walking and running using human pose tracking algorithm," *Gait & Posture*, vol. 85, pp. 290–297, Mar. 2021, doi: 10.1016/J.GAITPOST.2021.02.006.

[76] E. D'Antonio, J. Taborri, E. Palermo, S. Rossi, and F. Patane, "A markerless system for gait analysis based on OpenPose library," *I2MTC 2020 - International Instrumentation and Measurement Technology Conference, Proceedings*, pp. 1–6, 2020, doi: 10.1109/I2MTC43012.2020.9128918.

[77] N. R. Pal and S. K. Pal, "A review on image segmentation techniques," *Pattern Recognition*, vol. 26, no. 9, pp. 1277–1294, Sep. 1993, doi: 10.1016/0031-3203(93)90135-J.

[78] P. KaewTraKulPong and R. Bowden, "An Improved Adaptive Background Mixture Model for Real-time Tracking with Shadow Detection," *Video-Based Surveillance Systems*, pp. 135–144, 2002, doi: 10.1007/978-1-4615-0913-4_11.

[79] M. Schmidt, "Argmax and Max Calculus," 2016.

[80] R. Poli, J. Kennedy, and T. Blackwell, "Particle swarm optimization," *Swarm Intelligence 2007 1:1*, vol. 1, no. 1, pp. 33–57, Aug. 2007, doi: 10.1007/S11721-007-0002-0.

[81] R. P. Dubois, D. V. Thiel, and D. A. James, “Using image processing for biomechanics measures in swimming,” *Procedia Engineering*, vol. 34, pp. 807–812, 2012, doi: 10.1016/j.proeng.2012.04.138.

[82] E. W. Maglischo, *Swimming Fastest*. Champaign: Human Kinetics, 2003.

[83] R. H. Sanders and C. B. McCabe, “Butterfly Technique,” in *Science of Swimming Faster*, S. A. Rodeo, Ed. Human Kinetics, 2015, pp. 87–95.

[84] “Swumsuit.” http://www.swum.org/swumsuit/index.html (accessed Sep. 20, 2022).

[85] Information-Technology Promotion Agency, “Picture materials for education (swimming),” 2014. http://www2.edu.ipa.go.jp/gz/%0Ah1swim/h1kn20/IPA-2kuro-ru.htm (accessed Jun. 19, 2015).

[86] J. Zhang and J. Hu, “Image Segmentation Based on 2D Otsu Method with Histogram Analysis,” *2008 International Conference on Computer Science and Software Engineering*, vol. 6, no. 1, pp. 105–108, Dec. 2008, doi: 10.1109/CSSE.2008.206.

[87] N. Otsu, “A Tlreshold Selection Method from Gray-Level Histograms,” *IEEE transactions on systems, man, and cybernetics*, vol. 9, no. 1, pp. 62–66, 1979.

[88] R. C. Gonzalez and R. E. Wood, *Digital Image Processing*, 4th ed. USA: Pearson, 2017.

[89] “DLT Method.” http://kwon3d.com/theory/dlt/dlt.html (accessed Sep. 20, 2022).

[90] M. Pink, J. Perry, A. Browne, M. L. Scovazzo, and J. Kerrigan, “The normal shoulder during freestyle swimming: An electromyographic and cinematographic analysis of twelve muscles,” *American Journal of Sports Medicine*, vol. 19, no. 6, pp. 569–576, Apr. 1991, doi: 10.1177/036354659101900603.

[91] S. Ito and K. Okuno, “Visualization and motion analysis of swimming,” *Procedia Engineering*, vol. 2, no. 2, pp. 2851–2856, Jun. 2010, doi: 10.1016/J.PROENG.2010.04.077.

[92] B. Rosenhahn, U. G. Kersting, A. W. Smith, J. K. Gurney, T. Brox, and R. Klette, “A system for marker-less human motion estimation,” *Pattern Recognition, Proceedings*, vol. 3663, pp. 230–237, 2005.

[93] Z. Zivkovic, “Improved adaptive Gaussian mixture model for background subtraction,” *Proceedings - International Conference on Pattern Recognition*, vol. 2, pp. 28–31, 2004, doi: 10.1109/ICPR.2004.1333992.

[94] A. A. Goshtasby, *Image Registration: Principles, Tools and Methods*. Springer Science & Business Media, 2012.

[95] D. Wang, D. Tan, and L. Liu, “Particle swarm optimization algorithm: an overview,” *Soft Computing*, vol. 22, no. 2, pp. 387–408, Jan. 2018, doi: 10.1007/S00500-016-2474-6/FIGURES/2.

[96] D. E. Goldberg, *Genetic Algorithms in Search, Optimization and Machine Learning*, 13th ed. Addison-Wesley Professional, 1989.

[97] P. Craven and G. Wahba, “Smoothing noisy data with spline functions,” *Numerische Mathematik 1979 31:4*, vol. 31, no. 4, pp. 377–403, Dec. 1978, doi: 10.1007/BF01404567.

[98] J. J. Bartko, “The Intraclass Correlation Coefficient as a Measure of Reliability,” *http://dx.doi.org/10.2466/pr0.1966.19.1.3*, vol. 19, no. 1, pp. 3–11, Sep. 2016, doi: 10.2466/PR0.1966.19.1.3.

Acknowledgement

First, I would like to express my upmost gratitude to God. for the guidance and strength throughout my doctoral study.

I would also like to thank the AUN/SEED-Net JICA for providing me scholarship throughout the doctoral study. I would also like to thank to Professor Motomu Nakashima for his trust, encouragements, advice, supports, and patience during my doctoral study. I am gratefully indebted to his for his enormous support and advise even when I had to return to Indonesia to complete all my doctoral papers. Prof. Nakashima is always willing to take the time to discuss both research and writing papers or other things when I was still in Japan and Indonesia. Also, I would like to thank Professor Andi Isra Mahyuddin and Professor Tatacipta Dirgantara for always encourage me to finish my doctoral study in my activity as faculty staff at Faculty of Mechanical and Aerospace Engineering ITB.

I also really thankful to my friends in Tokyo: Randy, Michael, Devin, Benny, Rio, Natasha, and every name I cannot mention one by one for their continuous supports, especially in the beginning of my stay in Japan and throughout the roller-coaster ride I have during my study in Japan. To my lab mates: Terakado, Tsunoda, Razi, Nemoto-san for filling my days in the lab so that it is more colorful and not boring in the lab. Also, I would like to thank all the former and present lab member in Nakashima and Miyazaki laboratory.

Finally, I must express my very profound gratitude to my parents with unfailing support and continuous encouragement throughout my years of study and through the process of researching and writing this thesis. This accomplishment would not have been possible without them. Thank you.

Author

Ferryanto